UNIVERSIDADE ESTADUAL DE CAMPINAS
INSTITUTO DE FÍSICA "GLEB WATAGHIN" - IFGW

Espectroscopia de Emissão de Fótons do Hélio, Nitrogênio, Silício e Argônio

Annette Lina Marie Siems

Orientador: Prof. Dr. Antonio Gomes Trigueiros

Comissão Julgadora da Tese de Doutorado:

Prof. Dr. Antonio Gomes Trigueiros - IFGW/UNICAMP
Prof. Dr. Reinhard Bruch - Department of Physics/University of Nevada/Reno, USA
Prof. Dr. César José Bonjuani Pagan - FEEC/UNICAMP
Prof. Dr. Fernando Jorge da Paixão Filho - IFGW/UNICAMP
Prof. Dr. Roberto Antonio Clemente - IFGW/UNICAMP

Tese apresentada ao Instituto de Física da Universidade Estadual de Campinas como parte dos requisitos para obtenção do título de Doutor em Ciências

Campinas, São Paulo, Brasil
23 de Outubro de 2000

FICHA CATALOGRÁFICA ELABORADA PELA

BIBLIOTECA DO IFGW - UNICAMP

Si15e

Siems, Annette Lina Marie
Espectroscopia de emissão de fótons do hélio, nitrogênio, silício e argônio / Annette Lina Marie Siems. -- Campinas, SP : [s.n.], 2000.

Orientador: Antonio Gomes Trigueiros.
Tese (doutorado) - Universidade Estadual de Campinas, Instituto de Física "Gleb Wataghin".

1. Espectroscopia de emissão. 2. Colisões (Física). 3. Polarização (Luz). I. Trigueiros, Antonio Gomes. II. Universidade Estadual de Campinas. Instituto de Física "Gleb Wataghin". III. Título.

"The glory of friendship is not the outstretched hand, nor kindly smile, nor the joy of companionship; it is the spiritual inspiration that comes to one when he discovers that someone else believes in him and is willing to trust him with his friendship. "
-- Ralph Waldo Emerson--

Agradecimentos

Ao Prof. Antonio Trigueiros, pela orientação e confiança durante o curso. Ao Prof. Egon Hennies, Prof. Wildor Hennies e ao Prof. Cabrera. Aos companheiros de laboratório: Fernando Tamariz Luna, Andrés Callegari, José Tomaselli (in memoriam), Renata Orloski e Lúcia Helena Coutinho. Um agradecimento especial ao Newton Mansur. Aos amigos da pós-graduação, em especial Iglika e Alexei. Ao CNPq pela ajuda financeira do projeto. À secretaria de pós-graduação, em especial à Maria Ignez e Armando.

From the physics department of the University of Nevada Reno, USA, where the greatest part of this investigation took place I am deeply indebted to Prof. Reinhard Bruch for giving me the possibility to take part in his group and experiments, his financial support, his encouraging advice and assistance. I would like to thank Dr. Hocine Merabet for his help and advice. Thanks to Viktoria Golovkina and Guilhermo Hinojosa, without them I wouldn't have been able to get the data from the ECR. Many thanks to Prof. Natalia Afanasyeva for her warm care for me. I would also like to thank Prof. Ron Phaneuf for giving me beam-time at the ECR.

Ich moechte mich ganz herzlich bei meinen Eltern bedanken, ohne deren konstante Unterstuetzung, ob immaterieller oder materieller Art, ich nicht bis hierher gekommen wäre. Ein besonderer Gedanke an meine Grossmutter Traute Knoll, ich weiss, sie haette sich sehr fuer mich gefreut.

Resumo

Uma investigação detalhada da excitação do He ($1s^2$) ^1S para os estados de He (1snp) $^1P^o$ (n=2-5) e da excitação - ionização do He ($1s^2$) ^1S para os estados de He^+ (2p) $^2P^o$ e He^+ (3p) $^2P^o$ no sistema da colisão de H^++He é apresentada para uma escala larga de velocidades do projetil (2.2 a.u < v < 6.9 a.u.). Especificamente, os dados experimentais novos são apresentados em medidas do grau da polarização linear para a excitação e a excitação-ionização do hélio depois do impacto do próton nos comprimentos de onda no extremo ultravioleta (EUV). Estas medidas foram executadas usando um polarímetro caracterizado de espelho de multicamadas de molybdenum/silicon (MLM). Os resultados experimentais do próton são comparados com os dados teóricos da polarização usando a primeira aproximação de Born e os cálculos atômicos recentes de "Atomic Orbital Close-Coupling Calculations" (AOCC) para o processo da excitação. Uma comparação detalhada de dados experimentais para projeteis negativamente e positivamente carregados (elétrons e prótons) em velocidades iguais de impacto é dada. Estes resultados são relevantes para diagnósticos astrofísicos tal como "solar flares".

Além disso calculamos forças de osciladores ponderada "gf" e tempos de vida para o Si IV usando o método de Hartree-Fock. Nesse cálculo os parâmetros eletrostáticos foram otimizados usando o método dos mínimos quadrados, com a finalidade de melhorar o ajuste dos valores de níveis de energia experimentais. Este método produz valores de gf e tempos de vida mais próximos dos valores experimentais. Nós apresentamos todas as linhas conhecidas experimentais de dipolo elétrico do Si IV.

São apresentados também os primeiros espectros da emissão de EUV de fótons depois da captura simples e múltipla em colisões de 80 keV de Ar^{8+} + N_2**.** Nossa análise fornece a evidência de processos de captura de um e dois eletrons que resultam em transições radiativas dos estados

Ar^{7+}(nl), n=3-6 e Ar^{6+} (3lnl'), n=3-5 dos projeteis. Além disso nós identificamos numerosas linhas de alvo de N^{q+}(q=2,3) na escala do espectro de EUV (10-80 nm), devido à ionização múltipla da molécula de N_2 e da dissociação consecutiva mais a excitação dos fragmentos. A emissão de fóton subseqüente vem da excitação para os estados altos do alvo tais como $N^{2+}(1s^2 2s2lnl')\ ^{2,4}L$, n=2-10 e N^{3+} $(1s^2 2lnl')\ ^{1,3}L$,n=2-5 com energias da excitação até 52 eV e 78 eV, respectivamente. Os fragmentos dissociados e excitados de N^{2+}e de N^{3+}são devidos aos processos multiples de captura do elétron que envolvem até seis elétrons.

Abstract

A detailed investigation of excitation of He ($1s^2$) ^1S to He (1snp) $^1P^o$ (n=2-5) states and ionization-excitation of He ($1s^2$) ^1S to He^+ (2p) $^2P^o$ and He^+ (3p) $^2P^o$ states in H^+ + He collision systems is presented for a wide range of projectile velocities (2.2 a.u. < v < 6.9 a.u.). Specifically, new experimental data are presented on measurements of the degree of linear polarization for excitation and excitation-ionization of He following proton impact in the extreme ultraviolet (EUV) wavelengths. These measurements have been performed using a characterized molybdenum/silicon multilayer mirror polarimeter (MLM) whose polarization characteristics have been optimized for EUV emission of He and He^+. Furthermore, the proton experimental results are compared with theoretical polarization data using the first Born approximation and recent atomic orbital close coupling (AOCC) calculations for the excitation process. A comprehensive comparison of experimental data for negatively and positively charged projectiles at equal impact velocities is given. These results are relevant for astrophysical diagnostics such as solar flares.

Furthermore weighted oscillator strengths gf and the lifetimes for Si IV presented in this work were carried out in a multiconfiguration Hartree-Fock relativistic (HFR) approach. In this calculation, the electrostatic parameters were optimized by a least-squares procedure, in order to improve the adjustment to experimental energy levels. This method produces gf-values that are in better agreement with intensity observations and lifetime values that are closer to the experimental ones. In this work we present all the experimentally known electric dipole Si IV spectral lines.

We also present the first EUV Emission spectra following single and multiple-electron capture in 80 keV Ar^{8+} + N_2 highly charged ion-molecular collision system. Our analysis provides evidence of single and double capture processes leading to photon transitions of Ar^{7+} (nl) n=3-6 and Ar^{6+} (3lnl') n=3-5 projectile states. Furthermore we have identified numerous N^{q+} (q=2,3) ionic target lines in the

EUV-spectral range (10-80 nm), owing to multiple ionization of the N_2 molecule and consecutive dissociation plus excitation of the fragments. The subsequent photon emission arises from high lying states of the target such as $N^{2+}(1s^2 2s2lnl')\ ^{2,4}L$, n=2-10 and $N^{3+}\ (1s^2 2lnl')\ ^{1,3}L$,n=2-5 with excitation energies up to 52 eV and 78 eV, respectively. The N^{2+} and N^{3+} excited dissociated fragments are due to multiply electron capture processes involving up to six electrons.

Conteúdo

CAPITULO 1 : Introdução Geral

Por "Espectroscopia" nós geralmente entendemos o mapeamento experimental da estrutura dos níveis de energia de sistemas físicos. Para essa finalidade, os processos de transição, espontânea ou induzida, entre estados diferentes de energia são estudados e a espectroscopia consequentemente significa a análise de vários tipos de fenômen, como a radiação eletromagnética e a emissão de partículas. A investigação espectroscópica pode ser fundamental ou de uma natureza aplicada. A espectroscopia ótica é relacionada com o desenvolvimento da teoria atômica e molecular e usada também como uma ferramenta dentro da pesquisa de física básica e em outros ramos da ciência.

Durante os anos de desenvolvimento da mecânica quântica a estrutura atômica e molecular derivada dos espectros observados como também eles mesmos forneceram ferramentas de teste para os métodos teóricos novos. A troca proveitosa entre a teoria e a espectroscopia experimental continuou. Os poderosos computadores de hoje e os métodos computacionais permitem calcular os detalhes da estrutura dos níveis da energia e as probabilidades de transição com tal exatidão para o caso de sistemas simples de poucos elétrons, que medidas espectroscópicas novas são necessárias para validar as diferentes aproximações teóricas. Enquanto para os sistemas mais complexos, os cálculos são uma guia essencial à interpretação dos dados experimentais.

No caso da espectroscopia astronômica, que evoluiu constantemente desde a observação do espectro solar da linha de Fraunhofer, as observações dos foguetes e dos satélites em altura elevada abriram a região ultravioleta para a pesquisa astronômica, e a necessidade de interpretar as observações para os dados espectroscopicos, conduziu um crescimento também para a espectroscopia do laboratório. As recentes demandas para dados apareceram quando as

observações com o telescópio espacial de Hubble renderam os espectros ultravioletas com tal exatidão de resolução de comprimentos de onda que os dados atômicos velhos do laboratório provaram ser inadequados para identificações de linhas.

Demandas adicionais podem ser esperado quando os novos instrumentos com espectrometros de alta resolução para as regiões de extremo ultravioleta e infravermelho serão lançados no futuro.

Não somente os comprimentos de onda e as probabilidades das transições serão usadas, derivando a informação sobre plasmas astrofísicos das observações espectroscópicas. No caso da polarização, por exemplo, as medidas podem fornecer uma compreensão mais profunda de jatos induzidos pelos elétrons e/ou prótons em investigações de "solar flares".

Referencias Capitulo 1

[1] Svanberg S, Atomic and Molecular Spectroscopy: Basic Aspects and Practical Applications, Springer-Verlag Berlin Heidelberg 1997.

[2] Thorne A, Litzén U, Johansson S, Spectrophysics: Principles and Applications, Springer-Verlag Berlin Heidelberg 1999.

CAPITULO 2 :

Estudo do Grau da Polarização Linear depois da Excitação e da Ionização do Hélio pelo Impacto dos Prótons

2.1 Introdução

As investigações experimentais e teóricas do impacto do elétron e do próton em átomos são de importância considerável para nossa compreensão das colisões de muitos corpos. Especialmente processos eletrônicos em colisões de poucos corpos de complexos atômicos tais como o hélio são de grande significado do ponto da vista fundamental e aplicado. O átomo do hélio é o segundo elemento mais abundante no universo e é o sistema mais simples de dois-elétron fortemente ligados. Por estas razões este átomo é ideal para o estudo da dinâmica das colisões e dos efeitos da correlação [1-5] em colisões do íon-átomo.

Além disso, emissões radiativas dos íons de ionização simples tais como He^+ foram observadas em espectros solares sob as circunstâncias de "solar-flares". [6] Portanto, o estudo destes sistemas "beam-like" em não-equilibrio, complexos, anisotrópicos, pode fornecer uma compreensão mais profunda de jatos induzidos de elétrons e/ou prótons em investigações astrofísicas e dos "solar flares" [7-8]. Os astrofísicos da NASA, por exemplo, querem conhecer a importância dos prótons e elétrons nestas colisões (veja Fig. 1.)

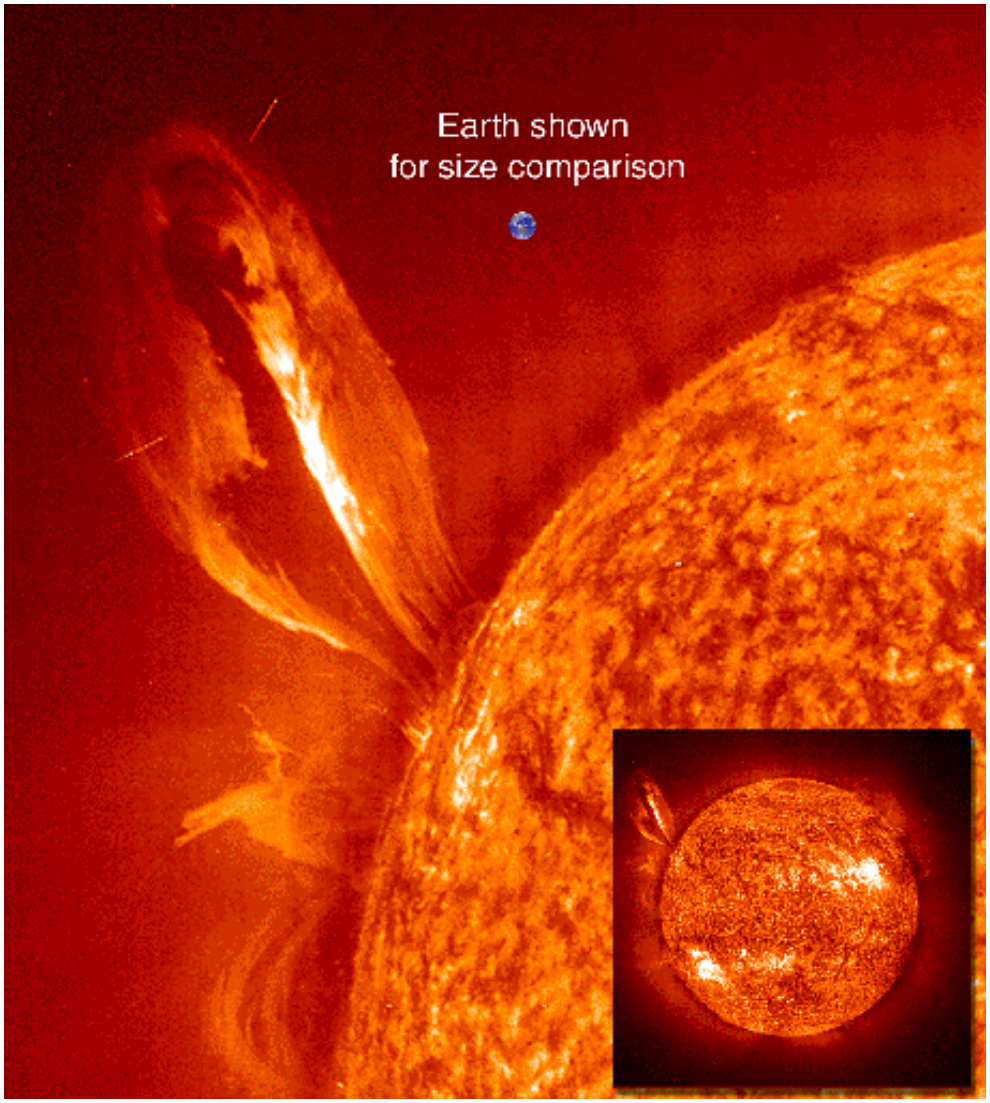

Fig.1 Grande erupção de He II de 304 Å, com uma imagem da terra adicionada para a comparação do tamanho. Este erupção de 24 de julho de 1999 é particularmente grande e fechada estendendo sobre 35 vezes o diametro da terra para fora do sol. As erupções podem afetar comunicações, sistemas de navegação, mesmo redes de energia elétrica, e também produzir as auroras visíveis nos céus da noite.

[Courtesy of SOHO consortium. SOHO is a project of international cooperation between ESA and NASA." → http://sohowww.nascom.nasa.gov/gallery/bestofsoho]

2.2 Colisões de Íons-átomos

Uma colisão de um próton com um átomo de hélio pode resultar nos seguintes estados finais:

$$
H^{+} + He \rightarrow \begin{cases}
H^{+} + \; He^{*} & \text{Excitação} \\
\qquad \mapsto He + h\nu & \\
 & \\
H + \; He^{+} & \text{Transferencia de Carga} \\
 & \\
H^{+} + \; He^{**} & \text{Dupla Excitação} \\
\qquad \mapsto He + h\nu & \\
\qquad \mapsto He^{+} + e^{-} & \\
 & \\
H^{+} + \; He^{+*} + e^{-} & \text{Ionização- Excitação} \\
\qquad \mapsto He^{+} + h\nu & \\
 & \\
H^{+} + \; He^{2+} + 2e^{-} & \text{Dupla Ionização}
\end{cases} \tag{1}
$$

O trabalho atual é uma investigação detalhada da excitação do hélio para os estados de (1snp) $^{1}P^{0}$ (n=2-5) e ionização-excitação do hélio para os estados de (2p) $^{2}P^{0}$ e (3p) $^{3}P^{0}$ em sistemas de colisões de H^{+} + He para uma escala larga de velocidades do projetil (2.2 u.a.< v < 6.9 u.a.) usando nossa técnica de análise da polarização. Especificamente, tais estados podem principalmente ser formados pelos seguintes canais da reação:

$$
\begin{aligned}
H^{+} + He\,(1s^{2})\,^{1}S \rightarrow He^{*}\,(1snp)\,^{1}P^{o} + H^{+} & \\
\llcorner\!\!\rightarrow He\,(1s^{2})\,^{1}S + h\nu, &
\end{aligned} \tag{2}
$$

envolvendo a emissão da radiação com os comprimentos de onda de λ = 517 a 584 Å para n=2 a 5, respectivamente; e:

$$
\begin{aligned}
&H^{+} + He\,(1s^{2})\,{}^{1}S \rightarrow He^{+*}\,(np)\,{}^{2}P^{o} + H^{+} + e^{-} \\
&\qquad\qquad\qquad\qquad\quad \hookrightarrow He^{+}\,(1s)\,{}^{2}S + h\nu, \qquad (3)
\end{aligned}
$$

envolvendo a emissão da radiação de Lyman-α (n=2) de λ = 304 Å e a emissão de 256 Å de HeII (3p) ${}^{2}P^{0}$. De agora em diante, nós usaremos a notação espectroscópica, isto é, o hélio neutro será etiquetado como " He I " e o hélio ionizado (H^{+}) será etiquetado como " He II ". Um diagrama esquemático dos níveis de energia para os estados de He I e de He II é mostrado na Fig.2, onde os comprimentos de onda de emissão mais fortes do He I (1snp) ${}^{1}P^{0} \rightarrow (1s^{2})\,{}^{1}S$ e He II (np) ${}^{2}P^{0} \rightarrow (1s)\,{}^{2}S$ são indicados.

Fig.2. Diagrama dos estados excitados do hélio neutro e ionizado

2.3 Polarização

Quando um projetil negativamente ou positivamente carregado colide com um átomo de hélio em energias intermediárias e altas de impacto, os mecanismos dominantes da colisão são excitação e ionização-excitação simultânea do alvo com detecção subseqüente dos fotons e/ou elétrons ejetados [9-10]. Na simetria cilíndrica, a radiação emitida das transições das linhas entre subniveis magnéticos pode ser polarizada linearmente quando observada em 90 graus com respeito à eixo central da quantização definida pelo feixe do projetil. Isto é devido à distribuição não-isotropica, não-Maxwelliana da população dos elétrons entre os subniveis (isto é, alinhamento nivelado da população). Por sua vez, este efeito do alinhamento resulta na emissão polarizada da linha que pode ser caracterizada pelo grau da polarização linear P definido pelo,

$$P = \frac{I_{\parallel} - I_{\perp}}{I_{\parallel} + I_{\perp}} \qquad (4)$$

onde o $I_{\parallel}$ é a intensidade da radiação com os vetores do campo elétrico orientados ao longo do eixo do feixe (eixo de z) e $I_{\perp}$ é a intensidade da radiação perpendicular ao eixo

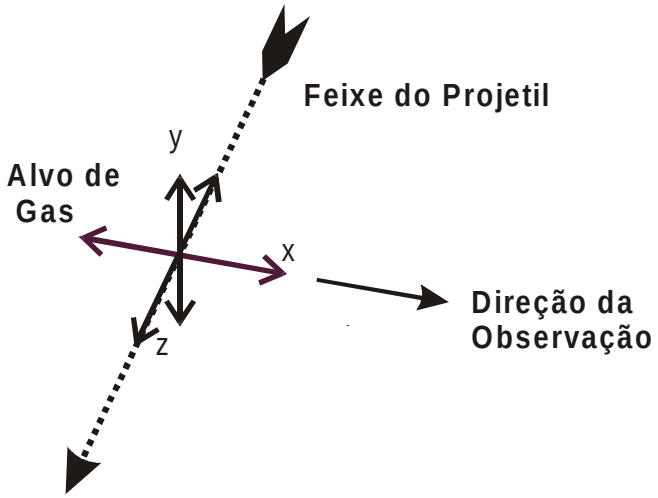

Fig. 3: Representação esquemática da distribuição dos dipolos elétricos para um ensemble de átomos excitados ou ions em direção de x,y e z.

central da quantização (eixo y) como mostrado na Fig.3 [11-12] .

O eixo x aponta ao longo do sentido da observação (a radiação dos dipolos orientados ao longo deste eixo não é observada). A medida e a análise do grau da polarização ou da distribuição angular da emissão do foton podem consequentemente revelar a anisotropia da fonte emissora.

2.4 O Experimento

As experiências foram realizadas na Universidade de Nevada, Reno, Estados Unidos.
Uma vista esquemática do experimento usado para as medidas da polarização é mostrada na Fig. 4. Os prótons foram extraídos com auxilio de uma fonte de RF e acelerados por meio de um Acelerador Van de Graaff de 2 MV. (Ao longo deste trabalho uma revisão geral do acelerador foi realizada, incluindo a limpeza de fonte de ions.) Estes íons foram focalizados e dirigidos por uma lente quadrupolo magnética em um feixe estável e intenso (analisador de massa e momentum). Após a passagem através da fenda incorporada na câmara do alvo (a qual possui um sistema de controle) onde o feixe é colimado antes de atravessar a célula do gás que contem o gás do hélio é coletado finalmente por um copo de Faraday para a normalização da carga (veja Fig. 5)

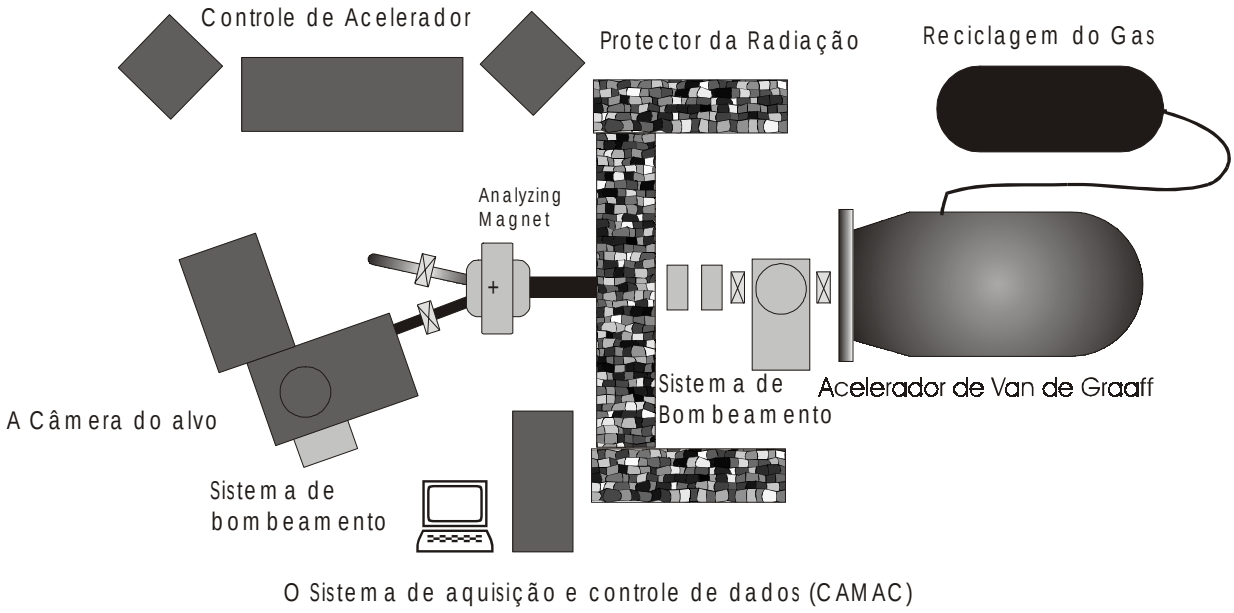

Fig. 4: O acelerador da Universidade de Nevada, Reno, Estados Unidos, a camera de alvo e o monocromador de EUV.

A instalação experimental inclui três componentes principais: (1) o polarímetro de EUV; (2) a celula do alvo e um copo de Faraday; e, (3) um monocromador de incidência rasante de 1.5 m. O polarímetro consiste de um elemento ótico: o Mo/Si MLM (Multi-layer-Mirror) (veja Fig. 5), um detetor do channeltron, o filtro espectral, e uma base rotatória. O MLM é montado em uma

cunha, que fixa o ângulo de incidência com respeito à superfície do espelho. Uma abertura removível, que prende um filtro espectral de VYNS-3 ou um filtro de Aluminum/Titanium (Al/Ti) [veja trabalho 1 do apêndice], é montada na frente do MLM. Esta abertura restringe o ângulo de incidência dentro de ±1 % correspondendo a uma largura de faixa do comprimento de onda da ordem de ±12 Å em 304 Å. O sistema é descrito em mais detalhes por Bailey *et al.*[9-13].

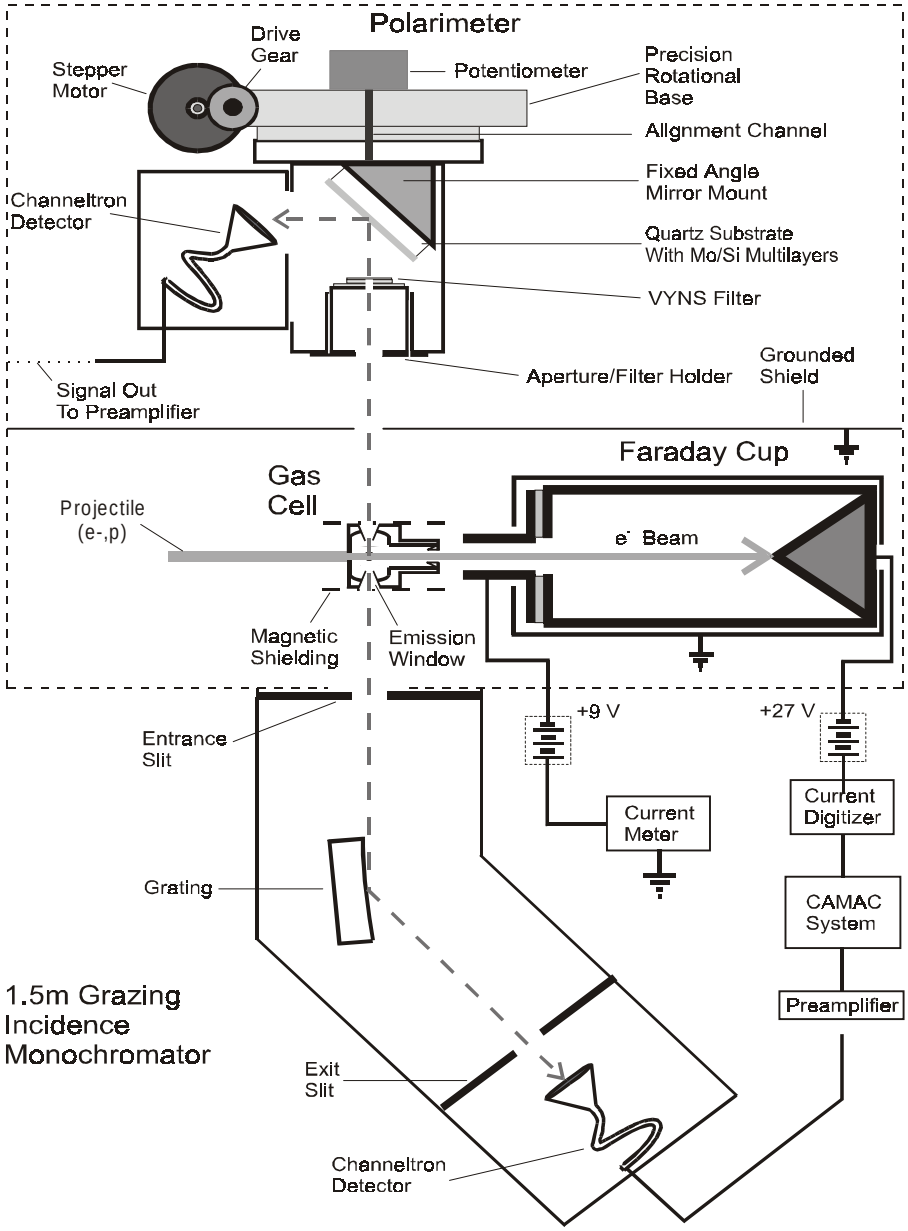

Fig.5. Vista esquemática do instrumento usado para medidas de polarização e da aquisição de dados.

2.4.1 Dependência do grau da polarização linear da pressão.

Os processos colissionais da excitação/desexcitação, da absorção, e da repopulação devido às colisões secundárias afetam o grau da polarização linear observado. Por causa disso, realizamos medidas para caracterizar a dependência da pressão com o grau da polarização da emissão do hélio excitado e ionizado-excitado usando o polarimetro.

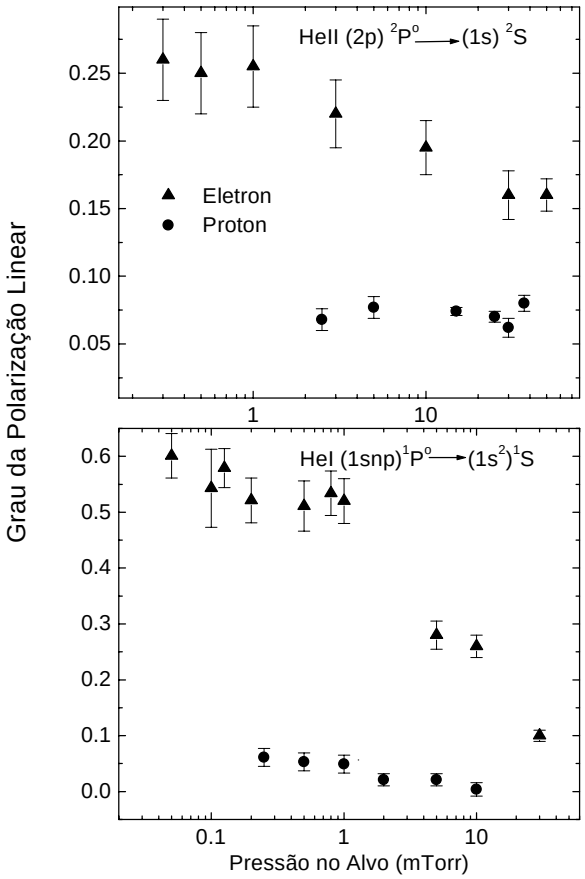

Fig.6 A dependência do grau da polarização da radiação de He I e He II com a pressão no alvo depois de impacto de 60-eV-elétrons e 220-keV-protons (correspondendo a um velocidade comparável de ≈ 2.1 e 2.9 a.u respectivamente).

Na Fig. 6, nós indicamos o grau da polarização linear em função da pressão do alvo para estados de He I e He II no caso do impacto de prótons. Incluímos dados para impacto de elétrons com He I

e He II para efeito de comparação. A fração da polarização mostra uma mudança gradual quando a pressão se torna maior do que 1 mTorr para impacto de elétrons e prótons com He I. Entretanto, vê-se claramente que a fração da polarização é constante entre 1 e 37 mTorr para prótons, enquanto mostra uma diminuição acima de 1mTorr para o projetil de elétrons no caso do He II. Consequentemente, estes dois sistemas apresentam mecanismos diferentes de colisão. Isto pode ser explicado pelo fato que os prótons são muito mais pesados do que os elétrons, assim envolvem ângulos menores de espalhamento durante as colisões, mesmo apos multiplos processos de colissões. As pressões de gás de 30 mTorr e 1 mTorr foram usadas para as medidas de impacto de próton.

2.5 Resultados e Discussão

Antes de discutir os resultados experimentais apresentamos as mais relevantes expressões da polarização de Percival and Seaton [14] e as relações correspondentes com o parâmetro de alinhamento integral correspondente, A_0 [15],

$$P(^1P^0) = \frac{\sigma(0) - \sigma(1)}{\sigma(0) + \sigma(1)} = \frac{3A_0}{A_0 - 2} \tag{5}$$

$$P(^2P^0) = \frac{3(\sigma(0) - \sigma(1))}{7\sigma(0) + 11\sigma(1)} = \frac{3A_0}{A_0 - 6} \tag{6}$$

$$A_0 = \frac{\sigma(1) - \sigma(0)}{\sigma(0) + 2\sigma(1)} \tag{7}$$

onde $\sigma(0)$ e $\sigma(1)$ são as subseções de choque magnéticas para os sub-estados magnéticos $M_L = 0$ e $M_L = \pm 1$ no acoplamento LS.

O parâmetro de alinhamento pode ser determinado pela medida da distribuição angular anisotrópica dos fótons emitidas pelo conjunto de estados excitados.

Polarização do He I (1snp) $^1P^0$

Os resultados da polarização do He I (1snp) $^1P^0$ são mostrados em Fig.7 para as energias do impacto de próton de 121 keV a 1.19 MeV. Os correspondentes dados do elétron [11,12], são descritos também nesta figura para comparação. (Os valores experimentais para os prótons são dados na tabela 1.) Ambos conjuntos de dados experimentais não foram corrigidos para efeitos cascata [12]. É evidente na Fig. 7 que o grau da polarização linear se comporta diferentemente para o impacto dos elétrons e dos prótons para velocidades equivalentes. A fração da polarização alcança mais do que 50% em uma velocidade de aproximadamente 2 a.u. no caso dos elétrons, e só 7% no caso dos prótons.

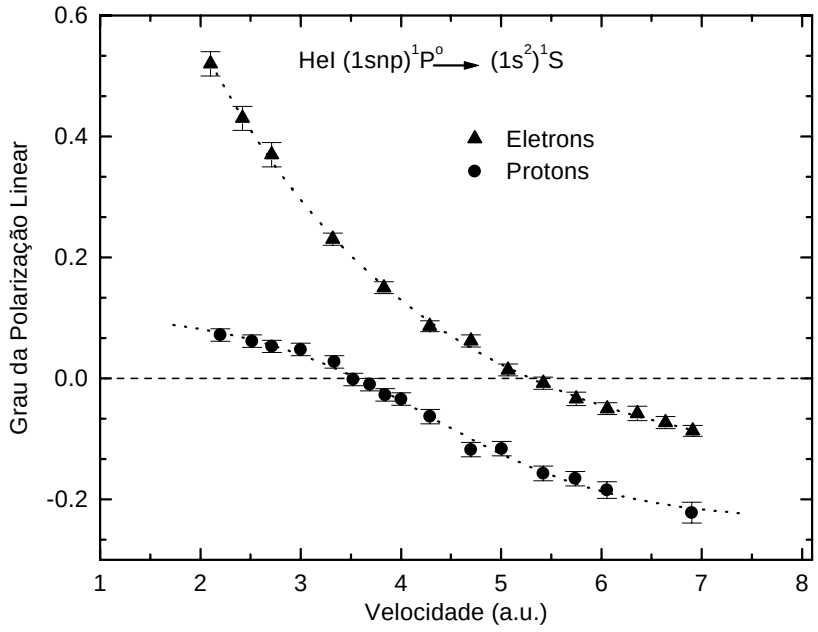

Fig.7.. Polarização da radiação de He I (1snp) $^1P^o \rightarrow (1s^2)\ ^1S$ como função da velocidade dos projeteis para o impacto de elétron e próton. As curvas pontilhadas são dadas para facilitar a visualização.

Além disso, os dois conjuntos de dados experimentais exibem um valor zero do grau de P em

velocidades distintas do impacto ao comparar o elétron e o próton em velocidades intermédias. Em velocidades mais elevadas (7 a. u.), os valores para prótons e elétrons apresentam ainda diferenças.

Tab.1: Polarização da radiação de He I (1snp) $^1P^o \rightarrow (1s^2)\ ^1S$ e incerteza para energias de próton de 121 até 1190 keV (v = 2.2 - 6.9 atomic units) na colisão de H^+ + He.

nergia do Próton [keV]	Velocidade do Próton [a.u.]	Grau da Polarização	Erro
121	2.20	0.072	0.010
158	2.51	0.061	0.010
184	2.71	0.053	0.010
225	3.00	0.048	0.010
278	3.34	0.027	0.010
310	3.52	-0.002	0.010
340	3.69	-0.010	0.010
369	3.84	-0.027	0.010
400	4.00	-0.034	0.010
460	4.29	-0.063	0.012
552	4.70	-0.118	0.012
626	5.01	-0.116	0.012
734	5.42	-0.157	0.012
823	5.74	-0.166	0.012
916	6.06	-0.185	0.014
1190	6.90	-0.222	0.017

Na Fig. 8, nós retraçamos os resultados experimentais do He I-próton junto com a primeira aproximação de Born (B1) [16] e cálculos teóricos mais avançados, baseados no método de atomic orbit close-coupling calculation (AOCC) [17].Como pode ser visto da figura, nem B1 nem o AOCC reproduzem nossas medidas. O P=0 acontece em velocidades diferentes para o AOCC e o experimento.

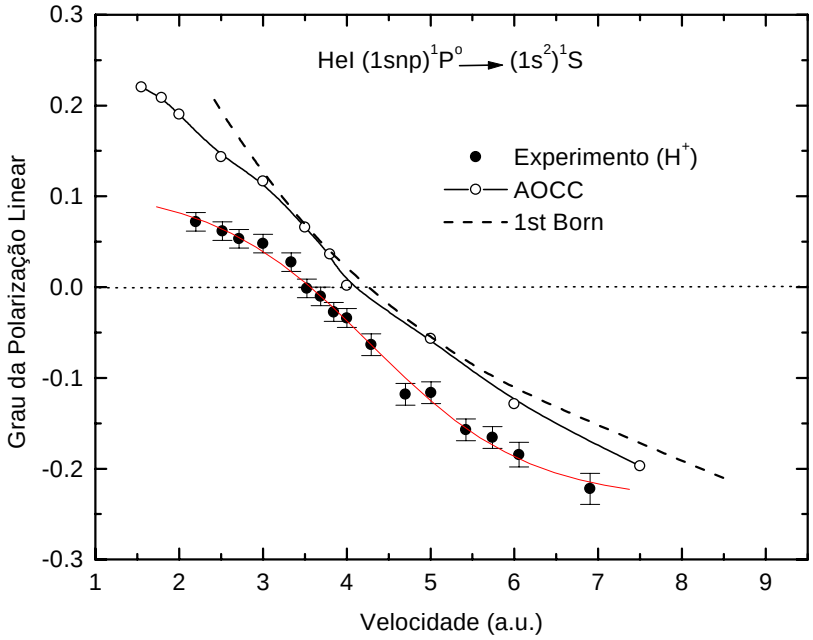

Fig.8. Polarização da radiação de He I (1snp) $^1P^o \rightarrow (1s^2)\ ^1S$ como a função da velocidade dos projeteis comparado com os calculos de "AOCC" e "first Born". A curva pontilhada é dada para facilitar a visualização.

É evidente, na Fig. 8, que a teoria de AOCC é diferente em energias baixas da primeira aproximação de Born e aproxima melhor nossos resultados experimentais. Os resultados de AOCC apresentados aqui são executados com os estados excitados limitados do alvo. Um cálculo mais exato, incluindo mais estados do alvo pode ainda melhorar a convergência aos dados experimentais. Tais cálculos mais sofisticados estão sendo executados agora.

Em velocidades elevadas de impacto, até 7 a.u. que correspondem ao impacto do próton de 1.19 MeV, resultados de AOCC também mostram uma aproximação melhor com a experiência do que a de B1. Em resumo, nós mostramos nesta seção que o grau da polarização linear depende fortemente do sinal da carga para projeteis dos elétrons e dos prótons. Estes resultados muito

interessantes podem ser usados como uma ferramenta diagnóstica nova para estudos dos "solar flares" e outras aplicações da física de plasma e da astrofísica.

Polarização do He II(np) $^2P^0$

Os resultados da polarização de He II (2p) $^2P^0$ e da polarização de He II (3p) $^2P^0$ são descritos na Fig. 9, para o impacto do próton no hélio. Os resultados da polarização de He II (3p) $^2P^0$

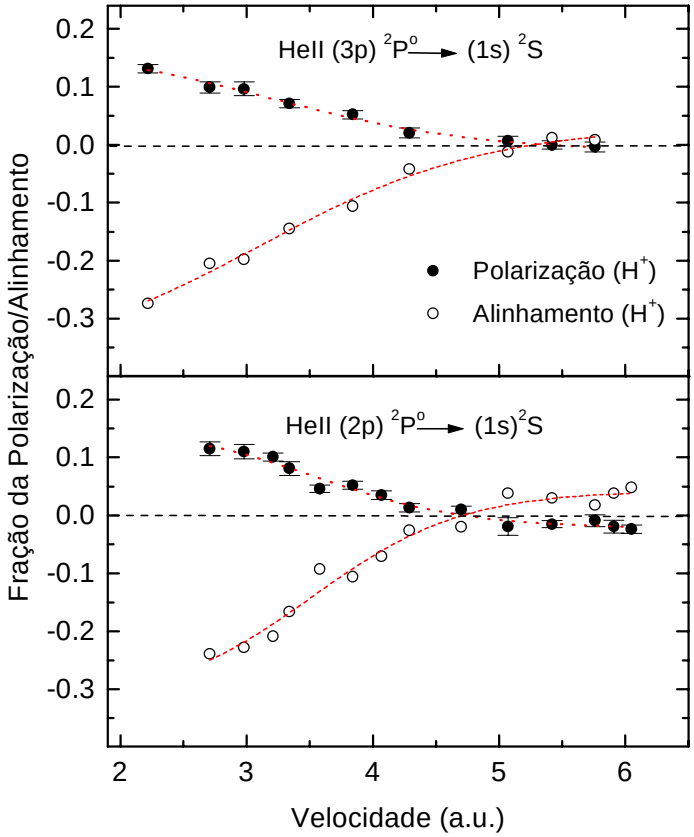

Fig. 9: Fração da Polarização P e parâmetro de alinhamento integral A_0 da radiação de He II (np) $^2P^o \rightarrow$ (1s) ^2S como função da velocidade de impacto de prótons. As curvas pontilhadas são dadas para facilitar a visualização.

nesta figura não foram corrigidos para efeitos cascata porque as seções de choque parciais dos

subniveis magnéticos para os subniveis magnéticos mais elevados de He II (nl) não são ainda exatamente conhecidas. Entretanto, devido às vidas muito mais curtas dos estados excitados de He II em comparação com os de He I, efeitos cascata associados com a repopulação magnética dos subniveis esperam-se ser menores do que para He I [5].

Os resultados da polarização de He II (2p) $^2P^0$ mostrados em Fig. 9 são ligeiramente mais elevados do que aqueles para He II (3p) $^2P^0$ (os valores experimentais são dados na tabela 2). Não obstante, os dois jogos dos dados concordam muito bem dentro de nossas incertezas experimentais. O acordo similar foi encontrado no exemplo do impacto do elétron no hélio.

Tab. 2. : Polarização da radiação de He II (np) $^2P^o \rightarrow$ (1s) ^2S, n=2,3 e incerteza para energias de próton de 184 ate 915 keV (v = 2.71 - 6.05 atomic units) na colisão de H^+ + He.

Energia do Próton [keV]	Velocidade do Próton [a.u.]	rau da Polarização He II (2p) $^2P^0$	Erro	rau da Polarização He II (3p) $^2P^0$	Erro
184	2.71	0.115	0.012	0.131	0.007
222	2.98	0.110	0.012	0.099	0.010
257	3.21	0.101	0.007	0.096	0.012
278	3.34	0.081	0.012	0.071	0.007
321	3.58	0.046	0.006	0.052	0.007
369	3.84	0.052	0.007	0.021	0.008
413	4.07	0.035	0.007	0.006	0.008
460	4.29	0.013	0.007	-0.006	0.007
552	4.70	0.010	0.006	-0.004	0.008
643	5.07	-0.019	0.015		
734	5.42	-0.015	0.006		
830	5.76	-0.009	0.010		
872	5.91	-0.019	0.011		
915	6.05	-0.024	0.007		

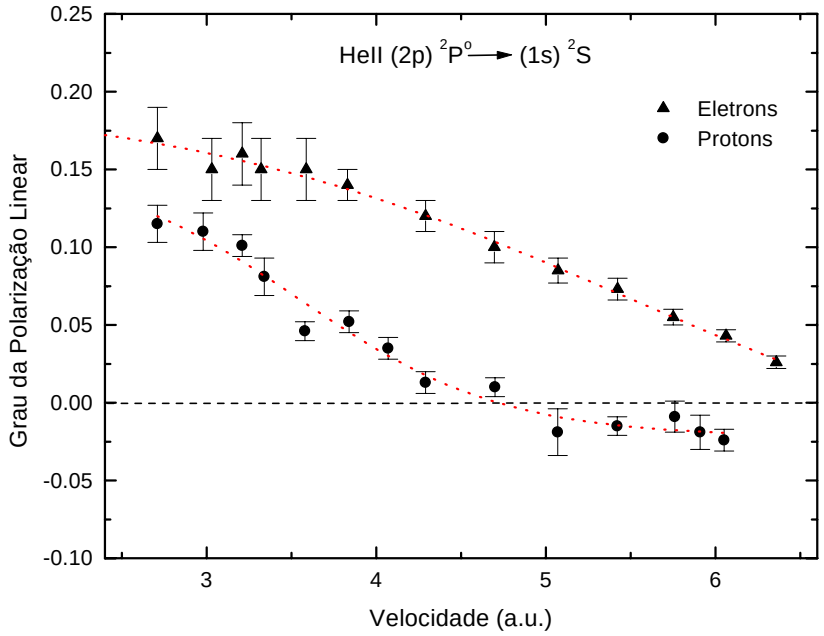

Fig. 10. Fração da polarização da emissão de He II (2p) $^2P^o \rightarrow$ (1s) ^2S como função das velocidades de impacto de elétrons e prótons. As curvas pontilhadas são dadas para facilitar a visualização.

Os dados da polarização de He II (2p) $^2P^0$ para projeteis do próton e do elétron (veja Fig. 10) indicam diferenças pronunciadas. Ambos os valores de polarização para elétrons e prótons, diminuem com o aumento da velocidade, mas os dados do próton são substancialmente diferentes dos dados do impacto do elétron para todas as velocidades da colisão. Além disso, a dependência da polarização da velocidade para He I é completamente diferente da de He II, isto é, os mecanismos dos canais da excitação e da ionização-excitação exibem distribuições angulares completamente diferentes da emissão de EUV. Não temos conhecimento de nenhum cálculo teórico exato para a polarização de Lyman-α e de β usando a aproximação sofisticada de muitos-corpos. O estudo atual pode servir como um exemplo importante para o futuro avanço dos cálculos teóricos para este muito interessante problema da colisão.

Referências Capitulo 2

[1] J.H. McGuire, *Electron Correlation Dynamics In Atomic Collisions*, Cambridge University Press, 1997.

[2] N. Stolterfoht, C.C. Havener, R. A. Phaneuf, J. K. Swenson , S. M. Shafroth, and F. W. Meyer, "Evidence for correlated double-electron capture in low-energy collisions of $O^{6+}$with He*"*, *Phys. Rev. Lett* **57**, pp. 74-77, 1986.

[3] S. Fülling, R. Bruch, E.A. Rauscher, P.A. Neill, E. Träbert, P.H. Heckmann, and J.H. McGuire, "Ionization plus excitation of helium by fast electron and proton impact", *Phys. Rev. Lett.* **68**, pp. 3152-3155, 1992.

[4] J. Chesnel, H. Merabet, B. Sulik, F. Fremont, C. Bedouet, , X. Husson, M. Grether, and N. Stolterfoht, "Radiative stabilization following double electron capture in slow Ne^{10+} + He collisions", *Phys. Rev. A* **58**, pp. 2935-2943, 1998.

[5] F.G. Donaldson, M.A. Hender, and J.W. McConkey, "Vacuum ultraviolet measurements of the electron impact excitation of helium", *J. Phys. B.* **5**, pp. 192 , 1972.

[6] S. A. Kazantsev, N.M. Firstova, A.V. Bulatov, A.G. Petrashen, J-C. Henoux, "Determination of proton's beam energy, manufactured in the solar flare, on the base of spectropolarimetry data", *Optics and Spectroscopy* **78**, pp. 729-737, 1995.

[7] S. A. Kazantsev, N.M. Firstova,, A.G. Petrashen, J-C. Henoux, " Determination of the energy of electron beam based on of the spectropolarimetry of emission of Ellerman's bombs", *Optics and Spectroscopy* **82,** pp. 714-722, 1997.

[8] S. Fineschi, J. M. Fontenla, P. MacNeice, N. N. Ljepojevic, "Electron impact polarization expected in solar EUV lines from Flaring Chromospheres/Transition regions", Proceedings of the Workshop on Max '91 /SMM Solar Flares: Observations and Theory, NO. **90-124**, pp.1-15, 1990.

[9] M. Bailey, R. Bruch, E. Rauscher, and S. Bliman, “Cross sections for the ionization-excitation of helium by fast electrons and H^+, H_2^+, H_3^+ ions: (np) $^2P^o$ levels, n=2-5”, *J. Phys. B: At. Mol. Opt. Phys*. **28**, pp. 2655-2670, 1995.

[10] W. C. Stolte and R. Bruch, " Cross sections for production of excited He^+ (np) $^2P^o$ states by 50-150 keV proton impact on helium", Phys. Rev. A **54**, pp.2116-2120, 1995.

[11] H. Merabet, A. Siems, R. Bruch, S. Fülling, M. Bailey, "Ionization-excitation of He following electron and proton impact: a polarization study using an EUV polarimeter", SPIE Conference on Ultraviolet and X-Ray Detection, Spectroscopy and Polaremetry III, Denver, Colorado, July 1999, SPIE Vol. 3764, pp.2.12, 1999.

[12] H. Merabet, M. Bailey, R. Bruch, D. V. Fursa, and I. Bray, J. W. McConkey, and P. Hammond, “A polarization study of the extreme ultraviolet emission from helium following electron impact”, *Phys. Rev. A* **60**, pp. 1187-1198,1999.

[13] M. Bailey, H. Merabet and R. Bruch, "Optical characterization of a compact multilayer mirror polarimeter in the extreme ultraviolet range", *Applied Optics* **38**, No. 19, pp.4125-4136, 1999.

[14] I.C. Percival and M.J. Seaton, "The polarization of atomic line radiation excited by electron impact", *Philos. Trans. R. Soc. London Ser. A* **251**, p. 113, 1958.

[15] K. Blum and H. Kleinpoppen, "Electron-Photon Angular Correlation in Atomic Physics", *Physics Report* **52**, p.203, 1979.

[16] L. Vriens and J.D. Carrière, "Analytical representations of generalized oscillator strengths excitation cross sections and polarization fractions", *Physica* **49**, pp.517-531, 1970.

[17] W. Fritsch and C. D. Lin, "The semiclassical close-coupling description of atomic collisions--recent developments and results", *Phys. Rept.* **201**, pp.1-97, 1991.

CAPITULO 3 :

Forças de Osciladores Ponderadas e Tempos de Vida para o Espectro do Si IV

3.1 Introdução

A estrutura de um sistema multieletrônico com N elétrons é obviamente muito mais difícil de calcular que um sistema de um elétron. Para sistemas puros de dois corpos, como o átomo hidrogênio, é possível solucionar a equação de Schrödinger analiticamente. Sistemas de muitos corpos, onde o movimento de cada elétron é acoplado com o movimento de todos os outros elétrons, precisa-se um modelo de aproximação. Um método de aproximação é o de Hartree-Fock. Este é baseado na aproximação que cada elétron se movimenta no potencial médio criado pelo núcleo e todos os outros elétrons. Esta hipótese leva para o modelo das partículas independentes, que essencialmente reduz o problema de muitos corpos para a problema que soluciona um número de equações de partículas singulares.

Estas equações são solucionadas iterativamente. Hartree fez seus primeiros cálculos à mão em 1928, mas cálculos deste tipo são certamente mais apropriados para computadores. Hoje vários códigos computacionais estão disponível gratuitamente.

Neste projeto nós trabalhamos com o Código de Cowan [1] . Calculamos forças de osciladores ponderadas e tempos de vida para o espectro do Si IV. Este trabalho faz parte de uma série de trabalhos sobre o silício do Laboratorio de Física Atômica e Molecular no Instituto de Física da Unicamp, Brasil [2-6]. O silício é um elemento importante em astrofísica e as forças de

osciladores e os tempos de vida são importantes no estudo de espectros solares e dos obtidos em laboratórios [7,8].

3.2 A Probabilidade de Transição de Einstein e o Tempo de Vida

Um átomo em um estado excitado j de Energia E_j pode espontaneamente fazer uma transição radiativa para um estado i de menor energia E_I, com a emissão de um fóton da energia

$$h\nu_{ji} = E_j - E_i \quad , \tag{1}$$

correspondendo à uma linha espectral de número de onda

$$\sigma_{ji} = 1/\lambda_{ji} = (E_j - E_I)/hc. \tag{2}$$

A taxa de transição espontânea de Einstein é definida como a probabilidade total por unidade de tempo de um átomo em um estado específico j fazer uma transição para qualquer dos g_i estados do nível da energia i:

$$A_{ji} = \sum_{M_i} a_{ji}. \tag{3}$$

Se no tempo t existem $N_j(t)$ átomos no estado j, a taxa de variação da população do N_j devido a transições espontâneas para todos estados do nível i, é dada por

$$dN_j(t)/dt = -A_{ji}N_j(t). \quad (4)$$

A intensidade de uma linha espectral é:

$$I(t) = hc\sigma_{ji}g_jA_{ji}N_j(t). \quad (5)$$

A probabilidade e Transição ponderada para emissão espontânea

$$g_jA_{ji} = g_j\sum_{M_i} a_{ji} = \sum_{M_j}\sum_{M_i} a_{ji}\,. \quad (6)$$

A taxa de variação total da população N_j é dada pela soma das taxas correspondentes a todas as transições possíveis para estados de menor energia:

$$\frac{dN_j(t)}{dt} = -N_j(t)\sum_i A_{ji}, \quad (7)$$

com a solução

$$N_j(t)=N_j(0)e^{-t/\tau_j}, \tag{8}$$

onde

$$\tau_j=\left(\sum_i A_{ji}\right)^{-1} \tag{9}$$

é o tempo de vida .

3.3 Forças de osciladores

A outra quantidade usada para descrever probabilidades de transição é a força de oscilador f. Esta quantidade tem o origem na explicação clássica da absorção e dispersão como oscilações forçadas e amortecidas dos osciladores atômicos por uma onda magnética. O valor de f foi introduzido para representar a fração de osciladores atômicos efetivos para cada freqüência de ressonância. Como a força de oscilador é um número conveniente sem dimensão, que é aproximadamente um para fortes transições de ressonância, ela é muito usada, especialmente por astrofísicos[9].

A força de oscilador no caso da emissão é definida como:

$$f_{ij} = -\frac{8\pi^2 mca_0^2\sigma}{3h(2J+1)} S = \frac{(E_i - E_j)}{3(2J+1)} S, \tag{10}$$

onde $E_i - E_j$ é a energia de transição e S é a força do dipolo elétrico, dada por

$$S = \left| \left\langle \gamma J \left\| P^{(1)} \right\| \gamma' J' \right\rangle \right|^2 . \tag{11}$$

Como A é definido como

$$A = \frac{64\pi^4 e^2 a_0^2 \sigma^3}{3h(2J'+1)} S \tag{12}$$

e a força de oscilador ponderada como

$$gf = -(2J'+1) f_{ji} = \frac{8\pi^2 mca_0^2\sigma}{3h} S, \tag{13}$$

nós temos a seguinte relação entre os dois:

$$gA = \frac{8\pi^2 e^2 \sigma^2}{mc} gf . \tag{14}$$

3.4. Código de Cowan

O código de Cowan, que nós usamos para o cálculo das forças de osciladores ponderadas e tempos de vida é composto por quatro programas:

- "RCN" usa o método de Hartree-Fock para calcular as funções de onda radiais de todos os elétrons.
- "RCN2" usa as funções de onda radiais para calcular as energias médias para as configurações, as integrais de Slater e as integrais de spin-orbita.
- "RCG" calcula os autovalores de energia (Método de Matriz de Slater-Condon). Se incluirmos as configurações pares e impares no cálculo, o programa então calcula as transições do dipolo elétrico, comprimentos de ondas, forças de osciladores, probabilidades de transições radiativas e tempos de vida radiativas dos níveis.
- "RCE" : Este programa toma as integrais radiais como parâmetros ajustáveis para dar o melhor “fit” possível com os valores experimentais de energia.

Todas as informações sobre o código de Cowan e a teoria podem ser encontrado no livro de Robert D. Cowan [1], especialmente nos capitulos 8 e 16.

3.5 Determinação semiempírica das forças de osciladores ponderadas e tempos de vida

Neste trabalho sobre o Si IV nós juntamos todos os dados experimentais disponíveis sobre o ion, como: Comprimentos de onda e intensidades das linhas e níveis energéticos conhecidos. Depois nós usamos o programa "Elcalc" (energy level calculation) [10]. Este Programa leva em consideração as transições, respectivamente os comprimentos de onda obtidos experimentalmente e os níveis de energia experimentais, para ajustar os valores de níveis de energia. Como os comprimentos de ondas são de origem de trabalhos experimentais diferentes, o programa agrega pesos diferentes para cada transição de acordo com o erro experimental. A seguir rodamos os programas RCN e RCG para obter os valores de gf e os tempos de vida (ab initio). Rodamos o programa RCE com os valores dos níveis de energia ajustados e fizemos um ajuste dos parâmetros para obter o menor desvio quadrático possível. Finalmente nós inserimos os parâmetros otimizados no programa RCG para obter valores de gf e tempos de vida com mais exatidão.

3.6. Forças de Osciladores Ponderadas e Tempos de Vida para o Espectro do Si IV.

O estado fundamental de silício três vezes ionizado, Si IV, é $1s^2 2s^2 2p^6 3s$ com o termo ^2S. Si IV pertence à seqüência isoeletrônica do Na I. O potencial de ionização é 364093.1 cm^{-1} (45.142 eV).

Seu espectro foi analisado pela primeira vez por Millikan & Bowen [11], McLennan &Shaver [12], e Fowler[13], que estudou o espectro de silício em detalhe, incluindo Si IV, na região de 1400-6700 Å.

Edlén & Söderqvist [14] melhoraram e estenderam a análise de Si IV na região de comprimento de onda de 815 - 4328 Å. Shenstone [15] observou linhas de Si IV na região de vácuo, mas ele não as publicou. Valores podem ser encontrado no Toresson [16] ou Kelly [17]. Toresson [16] estudou Si IV na região de 400 - 10 000 Å e ele forneceu todos os níveis conhecidos do íon (também publicado por Martin & Zalubas [18]). Beyer et al.[19] trabalhou com a técnica de beam-foil e ele deu transições não classificadas. Kelly[17] resumiu todos os comprimentos de onda publicados de Si IV na região de VUV.

Foram utilizadas 89 transições sendo que 29 configurações deram origem a estas transições. As configurações são: $2p^6(3s+4s+5s+6s+7s+8s)$, $2p^6(3d+4d+5d+6d+7d)$, $2p^6(5g+6g+7g+8g)$ e $2p^6$ 7i (pares), e $2p^6(3p+4p+5p+6p+7p+8p)$, $2p^6(4f+5f+6f+7f+8f)$, $2p^6(6h+7h)$.

Os valores de energia experimentais, que foram introduzido no programa RCE de Cowan foram calculados pelo programa ELCALC [10]. Os valores dos parâmetros utilizados no cálculo para as configurações são apresentados nas tabelas 1 e 2.

Tab.1 : Valores dos parâmetros de Hartree-Fock para as configurações pares do Si IV

Configurações	Parâmetros	HF cm^{-1}	Ajustados	HF/Ajustados
$2p^6 3s$	E_{av}	0	0	
$2p^6 4s$	E_{av}	195533	193979	1,008
$2p^6 5s$	E_{av}	267030	265418	1,006
$2p^6 6s$	E_{av}	301287	299677	1,005
$2p^6 7s$	E_{av}	320347	318743	1,005
$2p^6 8s$	E_{av}	332041	330440	1,005
$2p^6 3d$	E_{av}	160607	160376	1,001
	ζ_{3d}	5^a		
$2p^6 4d$	E_{av}	251424	250009	1,006
	ζ_{4d}	2^a		
$2p^6 5d$	E_{av}	293042	291498	1,005
	ζ_{5d}	1^a		
$2p^6 6d$	E_{av}	315489	313915	1,005
	ζ_{6d}	1^a		
$2p^6 7d$	E_{av}	328946	327362	1,005
	ζ_{7d}	0^a		
$2p^6 5g$	E_{av}	295411	293838	1,005
	ζ_{5g}	0^a		
$2p^6 6g$	E_{av}	316877	315305	1,005
	ζ_{6g}	0^a		

Tab.1 : Valores dos parâmetros de Hartree-Fock para as configurações pares do Si IV

Configurações	Parâmetros	HF	Ajustados	HF/Ajustados
		cm^{-1}		
$2p^6 7g$	E_{av}	329826	328250	1,005
	ζ_{7g}	0[a]		
$2p^6 8g$	E_{av}	338231	336651	1,005
	ζ_{8g}	0[a]		
$2p^6 7I$	E_{av}	329852	328261	1,005
	ζ_{7i}	0[a]		

[a] parâmetros foram mantidos fixos

Tab 2.: Valores dos parâmetros de Hartree-Fock para as configurações impares do Si IV

Configurações	Parâmetros	HF	Ajustados	HF/Ajustados
		1000 cm^{-1}		
$2p^6 3p$	E_{av}	71667	71595	1,001
	ζ_{3p}	267	307	0,870
$2p^6 4p$	E_{av}	219924	218375	1,007
	ζ_{4p}	94	108	0,870
$2p^6 5p$	E_{av}	278164	276554	1,006
	ζ_{5p}	44	50	0,880
$2p^6 6p$	E_{av}	307279	305667	1,005
	ζ_{6p}	20[a]		
$2p^6 7p$	E_{av}	323935	322329	1,005
	ζ_{7p}	15[a]		
$2p^6 8p$	E_{av}	334357	322754	1,036
	ζ_{7p}	9[a]		
$2p^6 4f$	E_{av}	255410	254128	1,005
	ζ_{4f}	1[a]		
$2p^6 5f$	E_{av}	295136	293719	1,005
	ζ_{5f}	0[a]		
$2p^6 6f$	E_{av}	316721	315230	1,005
	ζ_{6f}	0[a]		

Tab 2.: Valores dos parâmetros de Hartree-Fock para as configurações impares do Si IV

Configurações	Parâmetros	HF	Ajustados	HF/Ajustados
		1000 cm^{-1}		
$2p^6 7f$	E_{av}	329728	328200	1,005
	ζ_{7f}	0[a]		
$2p^6 8f$	E_{av}	338166	336617	1,005
	ζ_{8f}	0[a]		
$2p^6 6h$	E_{av}	316910	315317	1,005
	ζ_{6h}	0[a]		
$2p^6 7h$	E_{av}	329850	328257	1,005
	ζ_{7h}	0[a]		

[a]parâmetros foram mantidos fixos

Os valores calculados de forças de osciladores ponderadas para as transições e os tempos de vida para os níveis energéticos estudados do Si IV encontram-se no trabalho 2 do apêndice.

Referencias Capitulo 3

[1] Cowan RD. The theory of atomic structure and spectra. Berkeley: Univ California Press. 1981.

[2] Callegari F, Trigueiros AG. Weighted oscillator strength and lifetimes for the Si III spectrum. Astrophys J Suppl S 1998;119:181-188.

[3] Trigueiros AG, Jupén C. Weighted oscillator strengths for Si V spectrum. J Quant Spectrosc Radiat Transfer, 1996;56:713-723.

[4] Coutinho LH, Trigueiros AG. Weighted oscillator strength and lifetimes for the Si VI\ spectrum. Astrophys J Suppl S 1999;121:591-597.

[5] Orloski RV, Trigueiros AG, Cavalcanti GH. Weighted oscillator strength and lifetimes for the Si IX spectrum. J Quant Spectrosc Radiat. Transfer 1999;61:665-669.

[6] Cavalcanti GH, Luna FRT, Trigueiros AG. Weighted oscillator strength and lifetimes for the Si X spectrum. J Quant Spectrosc Radiat. Transfer 2000;64:5-13.

[7] Kempner JC, Richards MT. Analysis of the Si IV ultraviolet spectra of U Sagittae. Astrophys J 1999;512:345-350.

[8] Ahmed S, Pinfield DJ, Mathioudakis M, Keenan FP, Phillips KJH, Curdt W. Electron temperature diagnostics for the quiet Sun using Si IV lines. Astron and Astroph 1999;346:L69-L72.

[9] Thorne A, Litzén U, Johansson S, Spectrophysics: Principles and Applications, Springer-Verlag Berlin Heidelberg 1999.

[10] Radziemski LJ. and Kaufman V. Wavelength, Energy levels, and analysis of neutral atomic chlorine (CL I). J Opt Soc Am, 1969;59:424-443.

[11] Millikan RA and Bowen IS. Phys Rev. Extreme ultra-violet spectra. 1924;23:1-34.

[12] McLennan JC and Shaver WW Trans Roy Soc Canada.1924;18:14.

[13] Fowler A. I. Bakerian Lecture.- The spectrum of Silicon at Successive Stages of Ionization Phil Trans Roy Soc 1925;225:1-39.

[14] Edlén B and Söderqvist J. Neue Berechnung des Termsystems von Si IV. Z Phys 1933;87:217-218.

[15] Shenstone AG. Unpublished Data.1958.

[16] Toresson YG. Spectrum and term system of trebly ionized silicon. Ark Fys 1959;17:179-193.

[17] Kelly RL. J Phys Chem Ref Data, 1987;16:275-276.

[18] Martin WC. and Zalubas R. Energy levels of silicon, Si I through Si XIV. J Phys Chem Ref Data 1983;12:323-380.

[19] Beyer LM, Maddox WE, Bridwell LB, Duncan DD, Bingham LL, Asbell JC. The beam-gas spectra of silicon, sulfur and oxygen. Nucl Instr Meth 1973;110:61-67.

CAPITULO 4 :

Espectroscopia de Emissão de Fótons para o Diagnóstico da Captura Simples e Múltipla em Colisões de 80 keV de Ar^{8+} + N_2

4.1 Introdução

As investigações dos processos de um e dois elétrons em colisões rápidas íon-átomo e electron-átomo com poucos elétrons no alvo (tais como o hélio) atraíram interesse considerável na década passada [1.2.]. Também, as colisões lentas que envolvem íons altamente ionizados têm sido estudadas recentemente incluindo o sistema de Ar^{8+}+He [3-5]. Alem disso as investigações espectroscopicas de sistemas de íon-molécula tais como Ar^{8+} +H_2 e Ar^{8+} +N_2 foram executadas para elucidar processos como a transferência múltipla de carga do elétron, a dissociação molecular e a dinâmica da excitação [6-9]

Neste trabalho nós apresentamos os primeiros dados obtidos do sistema de Ar^{8+} +N_2 em colisões únicas que utilizam a espectroscopia do extremo ultravioleta (EUV). Este sistema de colisão é de interesse particular devido ao alvo molecular de muitos elétrons, que permite reações múltiplas de captura de elétrons e fragmentação e excitação subseqüentes de complexos moleculares altamente ionizados de N_2^{q+} . Estes íons moleculares são instáveis e dissociam rapidamente através dos processos da explosão de Coulomb que conduzem aos estados ionizados e altamente excitados do nitrogênio. A espectroscopia de fotoemissão de EUV é a ferramenta ideal para analisar seletivamente estes estados ionizados e excitados de N^{q+}. Estes estados fornecem informações

colisionais detalhadas sobre os novos canais de dissociação que seguem processos múltiplos de captura de elétrons com alvos moleculares de muitos elétrons.

4.2 O Experimento

As experiências foram executadas na Universidade de Nevada, Reno, (UNR), Estados Unidos usando o "14-Ghz Elétron Cyclotron Resonance (ECR) multicharged ion source facility" que é mostrada na figura 1.

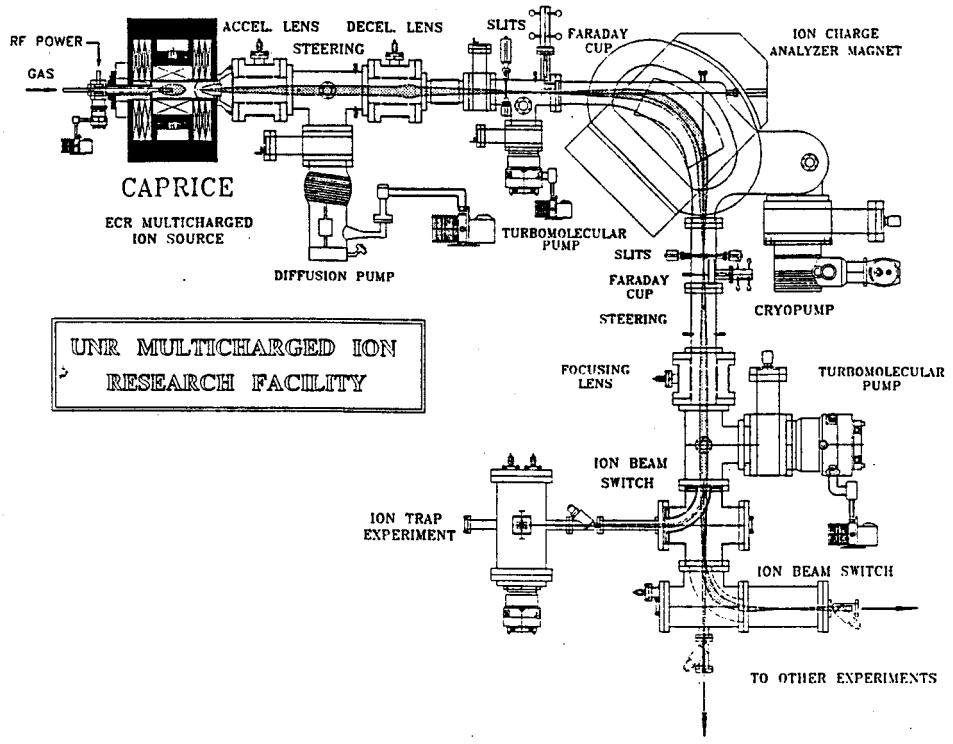

Fig. 1: A instalação experimental de fonte de ion de ECR da Universidade de Nevada, Reno, E.S.U.

O coração de sistema é uma fonte de ion CAPRICE electron-cyclotron-resonance (ECR), confinado magneticamente e gerado por ressonância ciclotronica dos elétrons por uma fonte de microondas. A " garrafa magnética " que confina os elétrons superaquecidos consiste de um par

de bobinas solenoidais que formam um espelho magnético axial, e de um hexapolo de ímã permanente que fornece o confinamento radial. Um gás ou vapor de metal de pressão baixa é admitido no garrafa magnética, e torna-se altamente ionizado por colisões sucessivas com os elétrons quentes. Os íons são extraídos da garrafa magnética através de uma abertura pequena por um campo externo. O feixe de ions é colimado e selecionado por carga/massa e dirigido para as experiências.

Como pode ser visto em Fig. 2 o experimento, é composto de um monocromator de incidência rasante (modelo 247 de Mc Pherson) de 2.2 m , uma câmara do alvo com uma célula de gás, o sistema do colimador, a lente quadrupolar para focalizar e dirigir o feixe de íon, e um copo de Faraday para a normalização do feixe de íon. A célula do alvo é operada em uma pressão de aproximadamente 0.7 mTorr e a pressão do fundo da câmara do vácuo é aproximadamente 5×10^{-7} torr. A pressão de gás na célula do alvo é controlada através de um manômetro (Barocel 655).

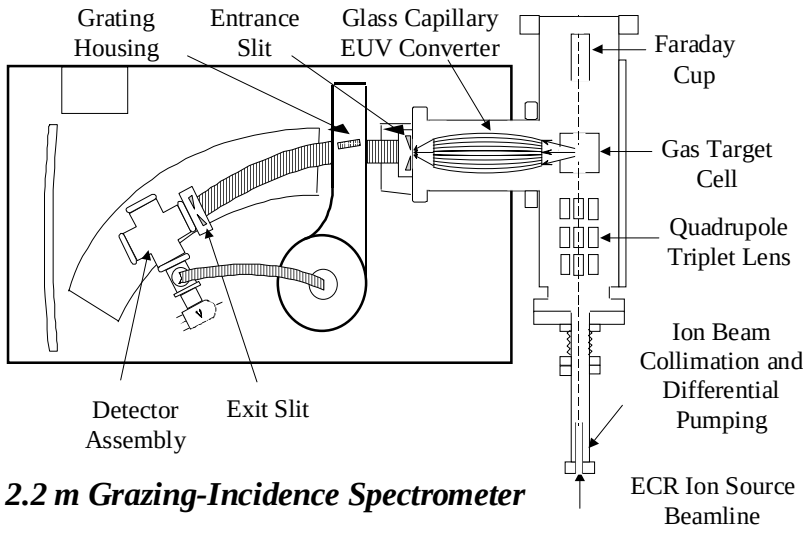

Fig. 2. O Experimento para Espectroscopia no EUV de colisões de íons altamente ionizados com moléculas.

Os fótons emitidos são observados sob um ângulo de 90^0 com respeito ao sentido do feixe do ion da incidência e as intensidades medidas da linha foram realçadas substancialmente (veja figura 3b) com o uso de um sistema capilar de vidro sofisticada de conversor (GCC: Glass Capillary Converter) [10-11, fig. 3a].

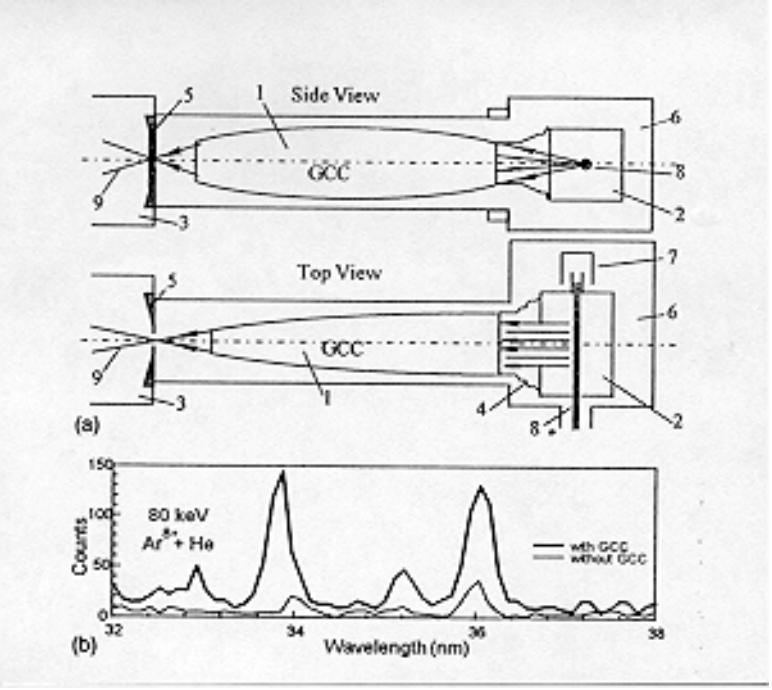

Fig. 3: (a) Espectrometro de EUV com GCC; (b) Espectro de EUV com e sem GCC [11]. 1. GCC, 2. Célula de gás, 3. Monocromador de incidência rasante, 4. Flexible housing, 5. Fenda de entrada do Monocromador, 6. Câmera do alvo, 7. Copo de Faraday, 8. Feixe de íons, 9. Radiação de EUV

Os fotons, que foram emitidos na célula de gás, são guiados, concentrados e focalizados pelo GCC na entrada da fenda do monocromador de incidência rasante de 2.2 m, que fica aproximadamente 60 cm do centro da célula de gás. O GCC consiste de 170 monocapilares de quartzo com um diametro de 390 µm.

O monocromator de incidência rasante de 2.2 m é equipada com uma rede de 600 linhas/mm. A aquisição de dados e o controle são realizados com um sistema computadorizado de PC-CAMAC, e as contagens dos fótons são normalizadas com respeito à quantidade de carga coletada no copo de Faraday. A largura da fenda do monocromator de incidência rasante foi ajustada para 400 μ m e a radiação curta do comprimento de onda é detectada por um "channeltron multiplier" (CEM). Nós calibramos relativamente nosso monocromator da incidência rasante de 2.2 m pela curva estabelecida da eficiência [12] obtida na universidade de Bochum, que pode ser visto na Fig. 4.

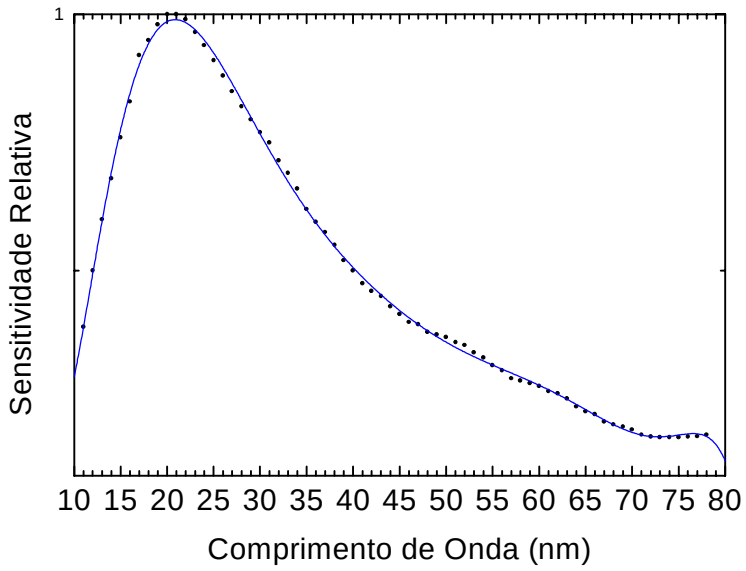

Fig. 4: Curva da eficiência para o monocromador de incidência rasante de 2.2 m.

Nós medimos os espectros de sistema de colisões de $Ar^{8+}+N_2$ no intervalo de comprimento de onda entre 10 -80 nm. Aqui nós apresentamos os resultados da identificação experimental das linhas do alvo e do projetil.

4.3 Resultados e Discussão

Em Fig. 5 nós exibimos o espectro de EUV entre 10 e 80 nm que foi executada sub condições de colisões únicas do sistema $Ar^{8+}+N_2$.

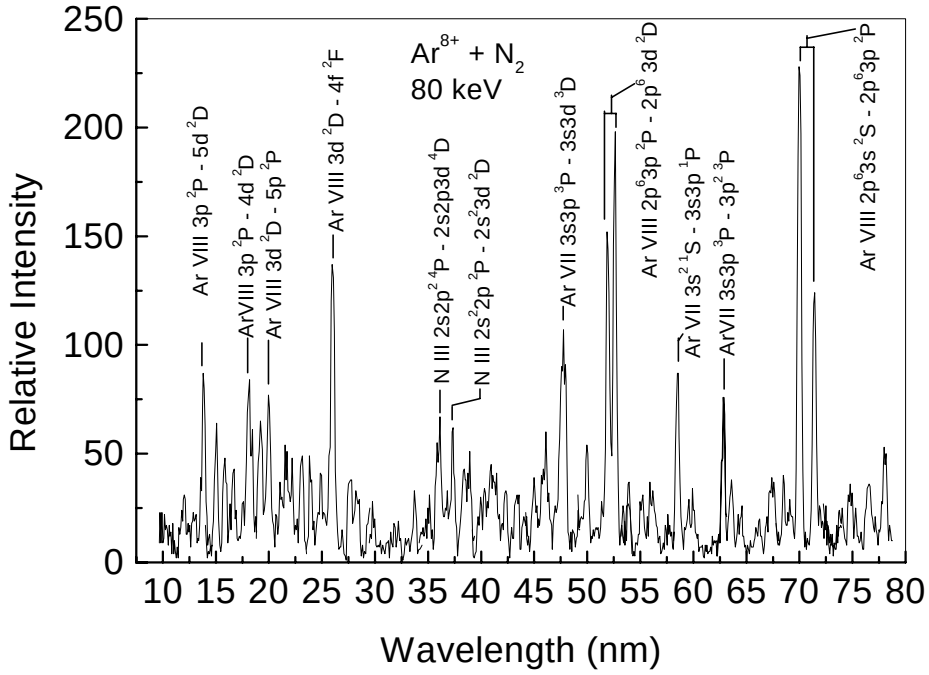

Fig.5.: Espectro de EUV para colisões de $Ar^{8+}+N_2$ no intervalo de comprimento de onda de 10 a 80 nm.

Os espectros mais detalhados se encontram no final deste capitulo. Nós fornecemos a evidência para mais de 150 linhas espectrais; muitas delas nós poderíamos identificar como linhas de projetil, especialmente íons de Ar^{7+} e Ar^{6+} devidos aos processos de captura simples e múltipla dos elétrons. Para a identificação das linhas do projetil nós utilizamos a tabulação detalhada de EUV do Kelly [14]. Para este fim nós executamos também cálculos extensivos de níveis de energia, comprimentos de onda, e probabilidades da transição para Ar $^{7+}$ (nl), n=3-6 e Ar $^{6+}$ (nln'l'), n'=3-5 , estados do projetil usando o código atômico da estrutura de Cowan [13]. O "classical over-

barrier model" foi utilizado para prever que níveis de número quântico principal de projetil serão povoados durante o processo de colisão.

[O "classical over barrier model": Quando um projetil carregado se aproxima de um alvo neutro, uma barreira impede o elétron do alvo de mover facilmente para dentro do potencial do projetil, mas essa barreira de potencial diminui gradualmente. Existe uma distancia interatomica R_0 onde a energia de ligação de elétron coincide com a altura da barreira, então o elétron é "compartilhado" entre os dois parceiros de colisão. Nas colisões lentas com um projetil altamente ionizado, o "classical over barrier model" assume que para todas as distancias menor que R_0 o elétron é capturado pelo projetil. Portanto uma estimativa para a seção de choque é: $\sigma_{tot} = \pi R^2_0$. As seções de choque determinadas assim normalmente concordem com os experimentos dentro de um fator dois.]

Os valores experimentais de comprimento de onda para as linhas de $Ar^{7+} + Ar^{6+}$ são mostrados nas tabelas 1 e 2. Nessas tabelas nos mostramos também os resultados de nossos cálculos teóricos e resultados de experimentos anteriores. É evidente na identificação dos espectros, que os seguintes processos simples e múltiplos são os proeminentes:

$$Ar^{8+} + N_2 \rightarrow Ar^{7+*} (nl, n=3\text{-}6) + N_2^{+} \qquad (1),$$

e

$$Ar^{8+} + N_2 \rightarrow Ar^{6+} (3lnl, n=3\text{-}5) + N_2^{2+} \qquad (2),$$

Estes são os canais principais que se estabilizam através das transições radiativas.

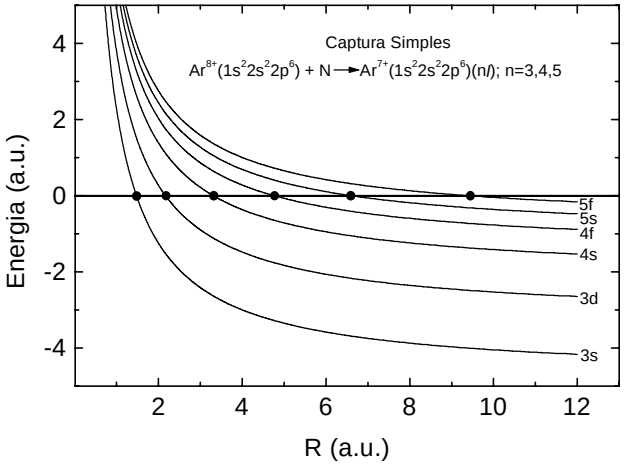

Fig. 6. Diagrama de correlação para os processos de captura de elétrons simples de Ar^{8+} + N utilizando o "classical over-barrier model".

Nós estabelecemos diagramas da correlação para os processos simples e duplos da captura de Ar^{8+}+N indicados em Fig. 6 e 7, respectivamente. É importante notar que nós usamos um modelo simplificado que substitui os potenciais de N_2 pelas curvas atômicas do nitrogênio e supusemos que as seções de choque são aproximadamente a metade da seção de choque para

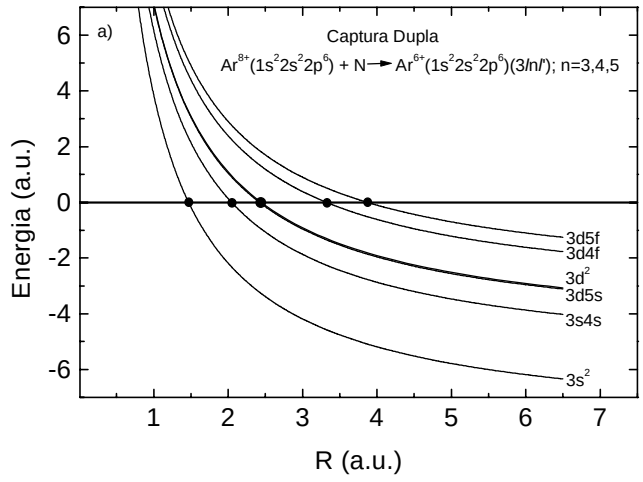

Fig. 7. Diagrama de correlação para os processos de captura de elétrons duplas de Ar^{8+} + N utilizando o "classical over-barrier model".

estados N_2. Usando esta aproximação, nós predizemos que para a captura simples dos elétrons, os estados de Ar^{7+}(nl) com n=3-5 estão povoados o mais abundante.

Além das linhas do projetil nós identificamos numerosas linhas do nitrogênio (usando a tabulação de Kelly) que originam de estados de N^{2+*} e de N^{3+*} que estabilizam-se pelas transições radiativas.

Estas linhas surgem nos espectros pela fragmentação dos complexos multiionizados de N_2^{q+}, q=1-6 e da excitação dos fragmentos de molécula consecutivos da dissociação. Na tabela 3 nós resumimos as transições principais de EUV que originam dos ions de N^{2+*} e de N^{3+*} na escala de 10-80 nm. De acordo com Remscheid et al.[7] tais ions de nitrogênio gerados em colisões lentos de $Ar^{8+}+N_2$ são produzidas mais provável pelo:

$$N_2^{q+} \rightarrow N^{r+}+N^{s+} \qquad (3)$$

onde na dissociação de N_2^{q+} a distribuição simétrica da carga de ambos os fragmentos é preferida, isto é que para N_2^{2+}, N_2^{4+} e N_2^{6+}os fragmentos muito provavelmente têm a mesma carga, visto que para os estados impares da carga tais como N_2^{3+} e N_2^{5+} eles diferem principalmente por uma unidade de carga. Em nossa experiência nós observamos a emissão do foton de EUV- dos fragmentos ionizados do nitrogênio, isto é estados altamente excitados do alvo como $N^{2+}(1s^2 2s2lnl')\ ^{2,4}L$, n=2-10 e $N^{3+}\ (1s^2 2lnl')\ ^{1,3}L$, n=2-5 N^{2+} com energias da excitação até 52 e 78 eV, respectivamente (veja a tabela 3). Por exemplo os fragmentos excitados do nitrogênio de N^{2+} e N^{3+}podem resultar de mecanismo de captura de quatro e seis elétrons.

Ao comparar as intensidades relativas das linhas para as transições óticas de N^{2+*} e N^{3+*}, nós encontramos que 60% das linhas de alvo identificadas são de estados excitados de N^{2+*} visto que 40% originam de linhas de emissão de N^{3+*}em nossa região de comprimento de onda. Da tabela 3,

é óbvio que as configurações de N^{2+} (2s2p3d, 2s ^{2} 3d, 2s2p4d, e 2s2p 2) são povoadas de forma mais abundante em processos de captura de 3,4, e 5 elétrons. Além disso, para os canais da fragmentação de N^{3+*}, as configurações N^{3+*} (2s2p, 2s4p, 2s4s, 2p4p, 2p5s, 2s4s) dominem na escala espectral medida.

Tab.1. Identificação das transições de Ar^{7+} depois da captura simples de sistema de Ar^{8+}+ N_2. Para a comparação é mostrado também nossos cálculos teóricos e resultados experimentais anteriores.

ico	Inten-sidade Relativa	Transição	λ (nm) Este trabalho	λ (nm) Teorica[a]	λ (nm) Kelly[b]	λ (nm) Bruch *et.al*[c]	λ (nm) Bliman *et al*[d]
1	48	$3s\ ^2S_{1/2} – 6p\ ^2P_{3/2}$	10.55	10.645			
2	62	$3s\ ^2S_{1/2}$-$5p\ ^2P_{3/2}$	11.99	11.981	12.009		
3	39	$3p\ ^2P_{3/2} – 6s\ ^2S_{1/2}$	12.86	12.783			
4	60	$3p\ ^2P_{1/2}$ -$5d\ ^2D_{3/2}$	13.58	13.764	13.793		
	129	$3p\ ^2P_{3/2}$ -$5d\ ^2D_{5/2}$	13.84	13.810	13.844		13.82
6	25	$3p\ ^2P_{3/2} – 5s\ ^2S_{1/2}$	14.98	14.957	14.873		
8	57	$3s\ ^2S_{1/2}$ -$4p\ ^2P_{3/2}$	15.80	15.845	15.892	15.90	15.9
13	79	$3p\ ^2P_{3/2}$ -$4d\ ^2D_{5/2}$	18.03	17.973	18.025	18.00	18.0
14	63	$3d\ ^2D_{5/2}$ -$5f\ ^2F_{7/2}$	18.41	18.396	18.432		18.4
16	78	$3d\ ^2D_{5/2}$ -$5p\ ^2P_{3/2}$	19.98	19.937	20.003		20.0
27	50	$3p\ ^2P_{3/2}$ -$4s\ ^2S_{1/2}$	23.09	23.006	23.088	23.10	23.10
34	151	$3d\ ^2D_{5/2} – 4f\ ^2F_{7/2}$	26.03	26.009	26.033	26.00	26.030
54	43	$3d\ ^2D_{5/2}$ - $4p\ ^2P_{3/2}$	33.80	33.551	33.726	33.80	33.8
69	98	$4s\ ^2S_{1/2}$ -$5p\ ^2P_{3/2}$	38.91	38.917	38.943		39.0

80	71	$4p\ ^2P_{3/2}$ - $5d\ ^2D_{5/2}$	42.33	42.369		42.2
111	447	$3p\ ^2P_{1/2}$ -$3d\ ^2D_{3/2}$	51.90	52.004	51.943	51.943
	582	$3p\ ^2P_{3/2}$ -$3d\ ^2D_{5/2}$	52.65	52.620	52.646	52.666
147	1200	$3s\ ^2S_{1/2}$ - $3p\ ^2P_{3/2}$	70.0245	69.914	70.0245	70.0245
	689	$3s\ ^2S_{1/2}$ -$3p\ ^2P_{1/2}$	71.36	71.144	71.3812	71.3812
150	147	$4d\ ^2D_{5/2}$ – $5p\ ^2P_{3/2}$	73.81	73.940	74.00	

[a]Cowan, R.D., *The Theory of Atomic Structure and Spectra*, Univ. of California Press (1981).
[b]Kelly, R.L., *Atomic and Ionic Lines Below 2000 Å, H through Ar* (1982).
[c]Bruch, R., *et al., Rev. Sci. Instrum.*, **68** 1091 (1997).
[d]Bliman, S., *et al., Phys. Rev. A.*, **60** 1 (1999).

Tab.2. Identificação das transições de Ar^{6+} depois da captura dupla de sistema de Ar^{8+}+ N_2. Para a comparação são mostrados também nossos cálculos teóricos e resultados experimentais anteriores.

Pico	ntensidade elativa	Transição	λ (nm) Este trabalho	λ (nm) Teórico[a]	λ (nm) Kelly[b]	λ (nm) Bruch *et al.*[c]	λ (nm) Bliman *et al.*[d]
7	82	$3s3p\ ^3P_2$ – $3s5d\ ^3D_3$	14.98	15.162	15.226		
10	47	$3s3p\ ^3P_2$ – $3s5s\ ^3S_1$	16.60	16.575			
12	30	$3s^2\ ^1S_0$ - $3s4p\ ^1P_1$	17.54	17.682	17.657	17.54	17.54
15	53	$3s3p\ ^3P_2$ - $3s4d\ ^3D_3$	19.18	19.128	19.264	19.20	
31	44	$3s3p\ ^3P_2$ - $3s4s\ ^3S_1$	24.87	24.956	25.0940	25.10	
41	36	$3s3d\ ^3D_3$ – $3s4f\ ^3F_4$	29.81	29.844	29.700	29.800	29.766
59	50	$3s3d\ ^1D_2$ - $3s4f\ ^1F_3$	35.07	34.871			
98	282	$3s3p\ ^3P_0$ - $3s3d\ ^3D_1$			47.3938		
		$3s3p\ ^3P_1$ - $3s3d\ ^3D_2$	47.61	47.353	47.5656		
		$3s3p\ ^3P_1$ -	47.78	47.370	47.573		

		$3s3d\ ^3D_1$				
		$3s3p\ ^3P_2$ - $3s3d\ ^3D_3$	47.95	47.671	47.9379	
		$3s3p\ ^3P_2$ - $3s3d\ ^3D_2$		47.697	47.949	
105	146	$3s3p\ ^1P_1$ - $3s3d\ ^1D_2$	49.08		50.107	
114	110	$3p4d\ ^3D_2$ – $3d4d\ ^3G_4$	53.88	53.520		
129	311	$3s^2\ ^1S_0$- $3s3p\ ^1P_1$	58.51	57.987	58.575	58.575
135	158	$3s3p\ ^3P_1$ – $3p^2\ ^3P_2$	62.92		63.031	
140	100	$3s4p\ ^3P_2$ – $3s5s\ ^3S_1$	66.98	67.434		
141	157	$3s4d\ ^3D_3$ – $3s5f\ ^3F_4$	67.42	67.714		
155	294	$3s4f\ ^3F_4$ – $3s5g\ ^3G_5$	77.99	78.109		

[a]Cowan, R.D., *The Theory of Atomic Structure and Spectra*, Univ. of California Press (1981).
[b]Kelly, R.L., *Atomic and Ionic Lines Below 2000 Å, H through Ar* (1982*).*
[c]Bruch, R., *et al., Rev. Sci. Instrum.*, **68** 1091 (1997).
[d]Bliman, S., *et al., Phys. Rev. A.*, **60** 1 (1999).

Tab.3. Principais linhas ionizadas de alvo devido a fragmentação mais excitação depois da captura múltipla de elétrons em colisões de Ar^{8+} + N_2 de 80 keV.

Pico	ntensidade Relativa	Ion	Transição	λ (nm)[a]	λ (nm)[b]	Energia (eV)[c]
30	25	N^{2+}	$2s^2 2p\ ^2P_{3/2} - 2s2p5p\ ^2D_{5/2}$	24.63	24.6249	50.374
33	56	N^{2+}	$2s2p^2\ ^4P_{5/2} - 2s2p15d\ ^4D_{7/2}$	25.70	25.7502	55.260
35	17	N^{2+}	$2s^2 2p\ ^2P_{3/2} - 2s^2 10d\ ^2D_{5/2}$	26.89	26.8473	46.206
36	37	N^{2+}	$2s2p^2\ ^4P_{5/2} - 2s2p6d\ ^4P_{5/2}$	27.44	27.4374	52.299
37	46	N^{2+}	$2s^2 2p\ ^2P_{3/2} - 2s^2 7d\ ^2D_{5/2}$	27.70	27.6326	44.894
38	40	N^{2+}	$2s^2 2p\ ^2P_{3/2} - 2s^2 6d\ ^2D_{5/2}$	28.22	28.2209	43.959
42	26	N^{2+}	$2s^2 2p\ ^2P_{3/2} - 2s^2 5s\ ^2S_{1/2}$	29.98	29.9818	41.378
48	19	N^{2+}	$2s^2 2p\ ^2P_{3/2} - 2s^2 4d\ ^2D_{5/2}$	31.50	31.4850	39.402
53	16	N^{2+}	$2s^2 2p\ ^2P_{3/2} - 2s^2 4s\ ^2S_{1/2}$	33.20	33.2333	37.332
61	92	N^{2+}	$2s2p^2\ ^4P - 2s2p3d\ ^4P$	35.79	35.8578	41.688
62	112	N^{2+}	$2s2p^2\ ^2P_{3/2} - 2s2p3d\ ^2P_{3/2}$	36.06	36.1288	52.420
65	109	N^{2+}	$2s^2 2p\ ^2P_{3/2} - 2s^2 3d\ ^2D_{5/2}$	37.28	37.4441	33.136
68	77	N^{2+}	$2s2p^2\ ^2S_{1/2} - 2s2p4d\ ^2P_{3/2}$	39.35	38.7483	48.243
74	94	N^{2+}	$2s2p^2\ ^2P_{1/2} - 2s2p4d\ ^2P_{1/2}$	40.91	41.1056	48.252
144	200	N^{2+}	$2s^2 2p\ ^2P_{3/2} - 2s2p^2\ ^2P_{3/2}$	68.43	68.5816	18.101
154	116	N^{2+}	$2s2p^2\ ^4P_{5/2} - 2p^3\ ^4S_{3/2}$	77.14	77.2385	23.162
19	38	N^{3+}	$2s2p\ ^3P_2 - 2s5s\ ^3S_1$	21.04	20.9471	67.552
22	52	N^{3+}	$2s2p\ ^1P_1 - 2p4p\ ^1S_0$	21.73	21.7218	73.287
24	49	N^{3+}	$2p^2\ ^3P_2 - 2p5s\ ^3P_2$	22.22	22.1789	77.695

28	52	N^{3+}	$2s2p\ ^3P_2$ - $2s4s\ ^3S_1$	23.80	23.7991	60.460
39	36	N^{3+}	$2s2p\ ^1P_1$ – $2p3p\ ^1P_1$	28.53	28.5561	59.626
49	25	N^{3+}	$2p^2\ ^1S_0$ - $2s5p\ ^1P_1$	31.87	31.7596	68.224
50	27	N^{3+}	$2s2p\ ^3P_2$ – $2s3s\ ^3S_1$	32.26	32.2722	46.780
64	57	N^{3+}	$2p^2\ ^1S_0$ – $2s4p\ ^1P_1$	36.78	36.8108	62.868
153	194	N^{3+}	$2s^2\ ^1S_0$ – $2s2p\ ^1P_1$	76.540	76.5148	16.205

[a]Esse trabalho. [b]Dados de Kelly [14]. [c] Energia de Excitação é obtida dos dados de Kelly [14].

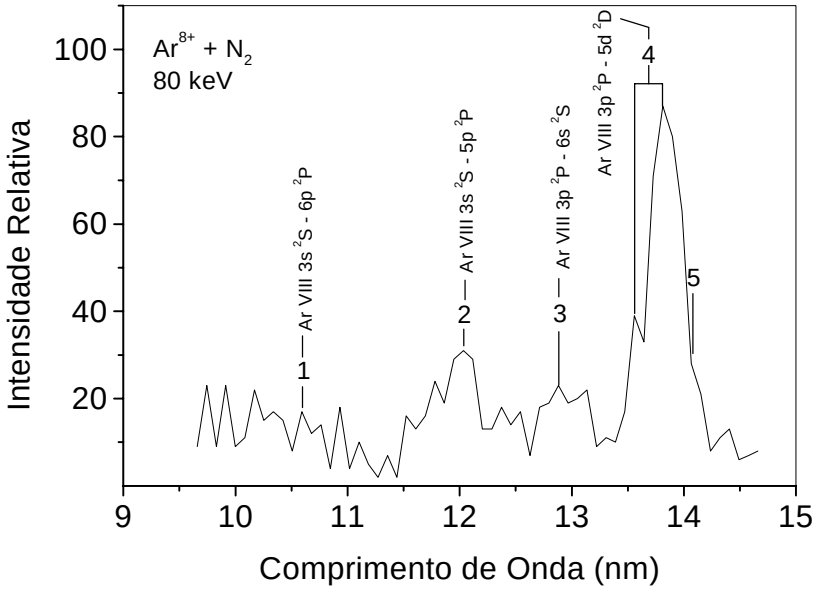

Espectro de EUV para colisões de Ar^{8+}+N_2 no intervalo de comprimento de onda de aproximadamente 9 ate 15 nm. As linhas dominantes são do alvo.

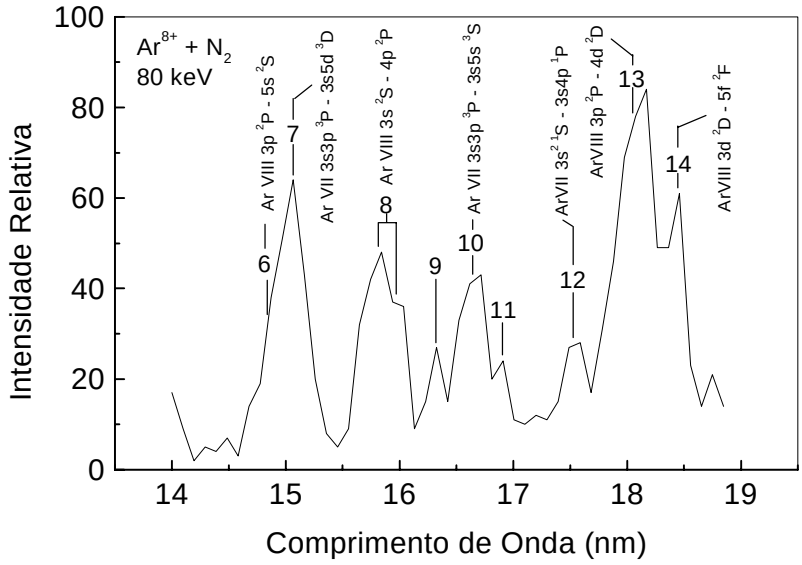

Espectro de EUV para colisões de Ar^{8+}+N_2 no intervalo de comprimento de onda de aproximadamente 14 ate 19 nm. As linhas dominantes são do alvo.

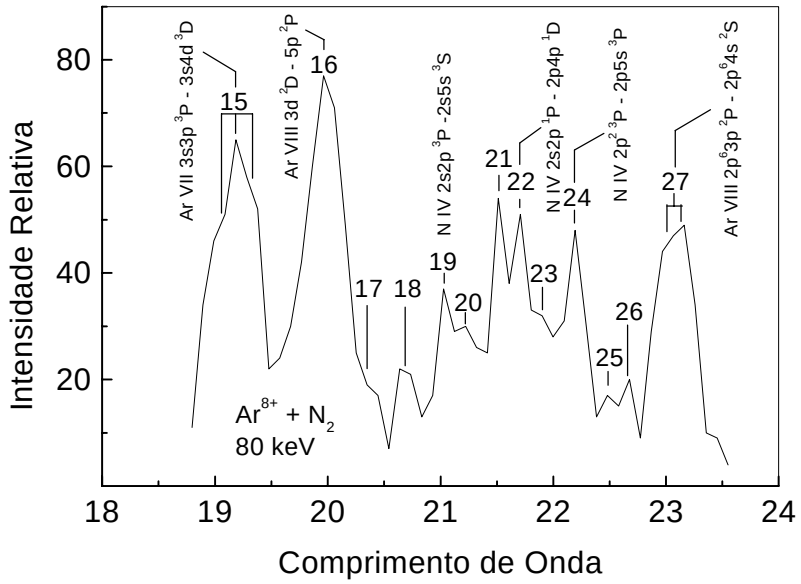

Espectro de EUV para colisões de Ar^{8+}+N_2 no intervalo de comprimento de onda de aproximadamente 19 ate 24 nm. As linhas dominantes são do alvo e do projetil.

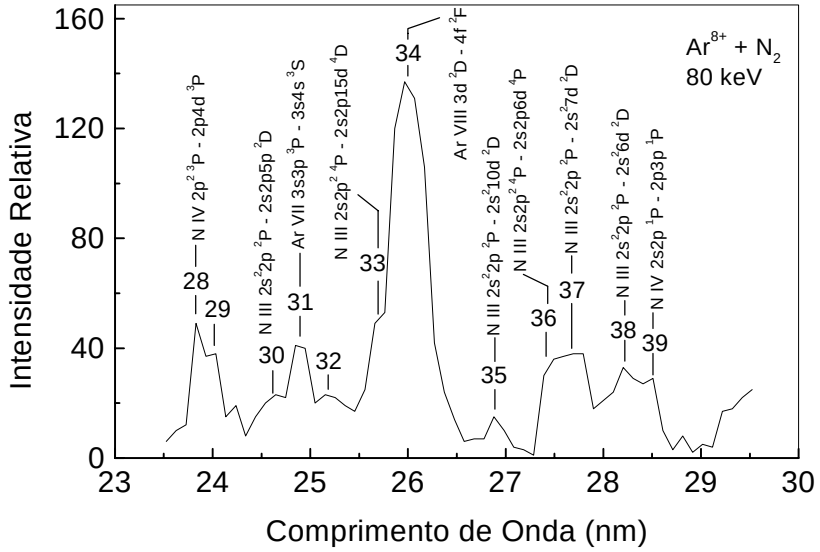

Espectro de EUV para colisões de Ar^{8+}+N_2 no intervalo de comprimento de onda de aproximadamente 24 ate 29 nm. As linhas dominantes são do alvo e do projetil.

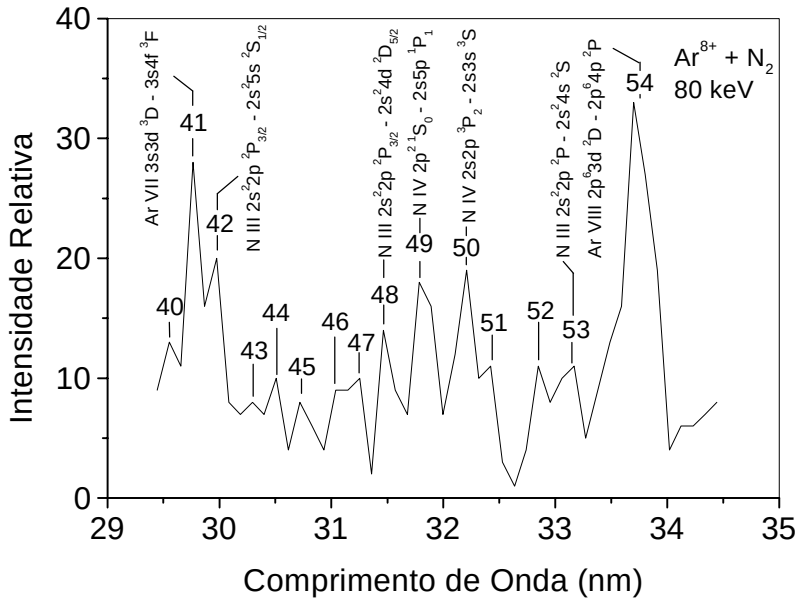

Espectro de EUV para colisões de Ar^{8+}+N_2 no intervalo de comprimento de onda de aproximadamente 29 ate 34 nm. As linhas dominantes são do alvo e do projetil.

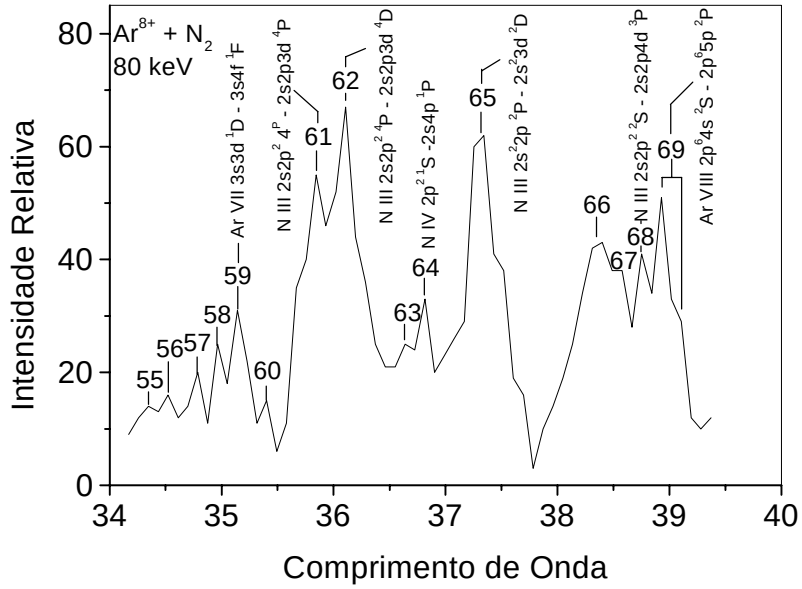

Espectro de EUV para colisões de Ar^{8+}+N_2 no intervalo de comprimento de onda de aproximadamente 34 ate 39 nm. As linhas dominantes são do alvo e do projetil.

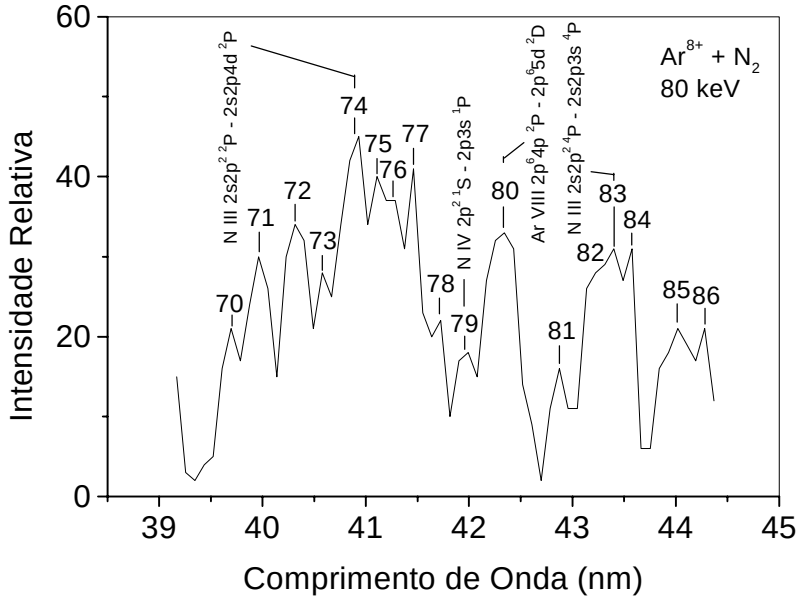

Espectro de EUV para colisões de Ar^{8+}+N_2 no intervalo de comprimento de onda de aproximadamente 39 ate 45 nm. As linhas dominantes são do alvo e do projetil.

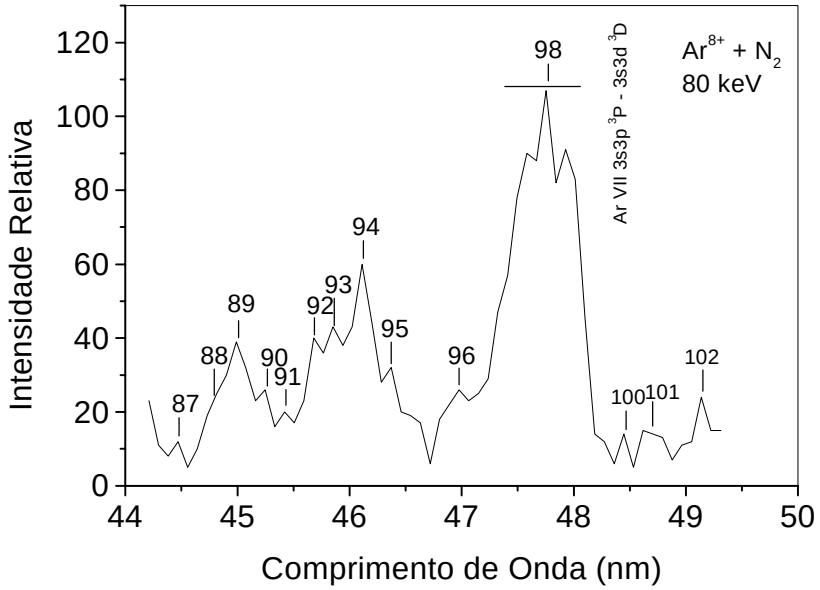

Espectro de EUV para colisões de Ar^{8+}+N_2 no intervalo de comprimento de onda de aproximadamente 45 ate 50 nm. As linhas dominantes são do alvo e do projetil.

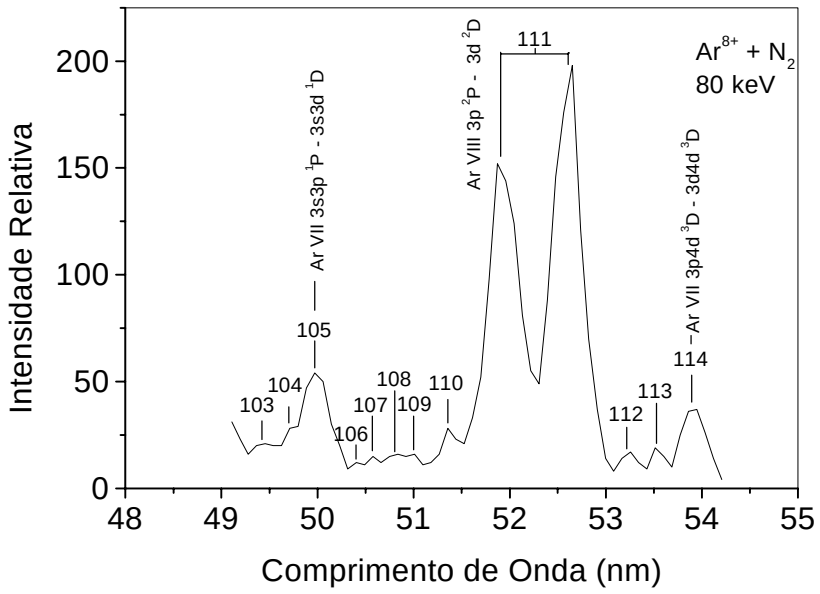

Espectro de EUV para colisões de Ar^{8+}+N_2 no intervalo de comprimento de onda de aproximadamente 49 ate 54 nm. As linhas dominantes são do alvo e do projetil.

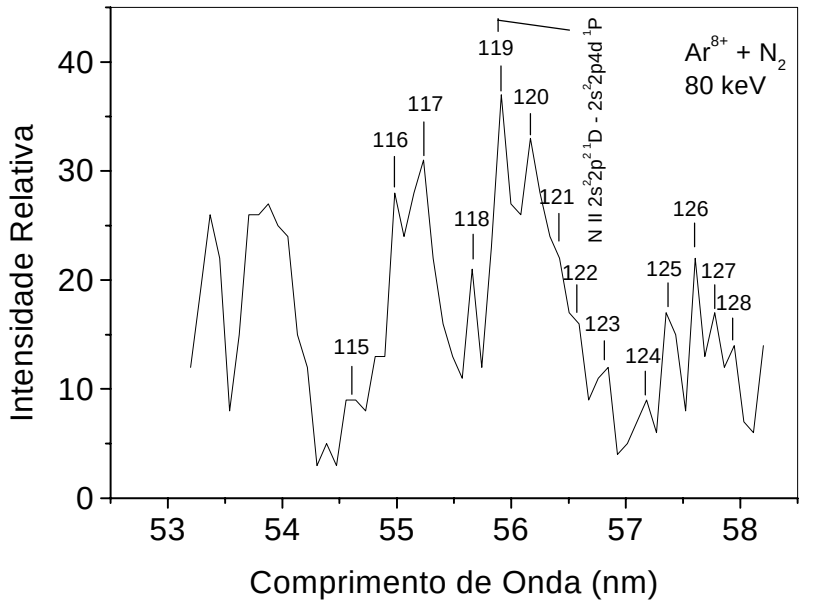

Espectro de EUV para colisões de Ar^{8+}+N_2 no intervalo de comprimento de onda de aproximadamente 53 ate 58 nm. As linhas dominantes são do alvo e do projetil.

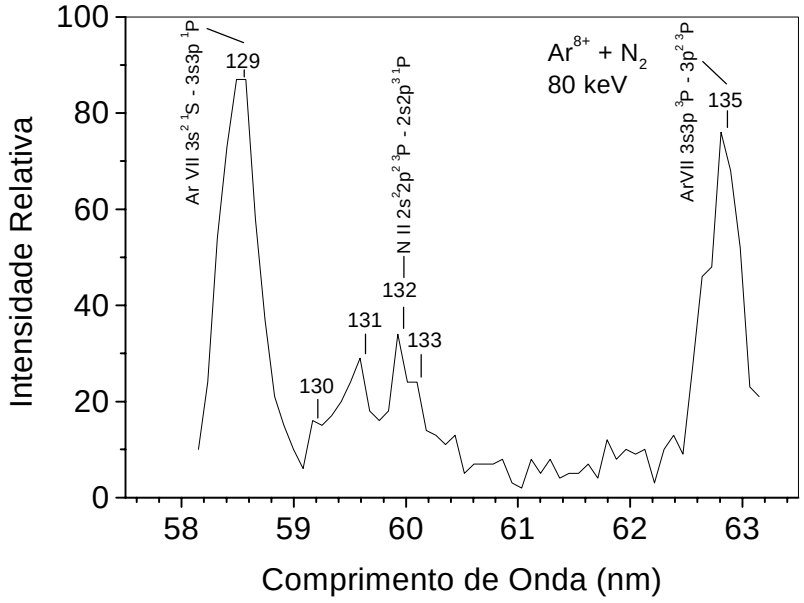

Espectro de EUV para colisões de Ar^{8+}+N_2 no intervalo de comprimento de onda de aproximadamente 58 ate 63 nm. As linhas dominantes são do alvo e do projetil.

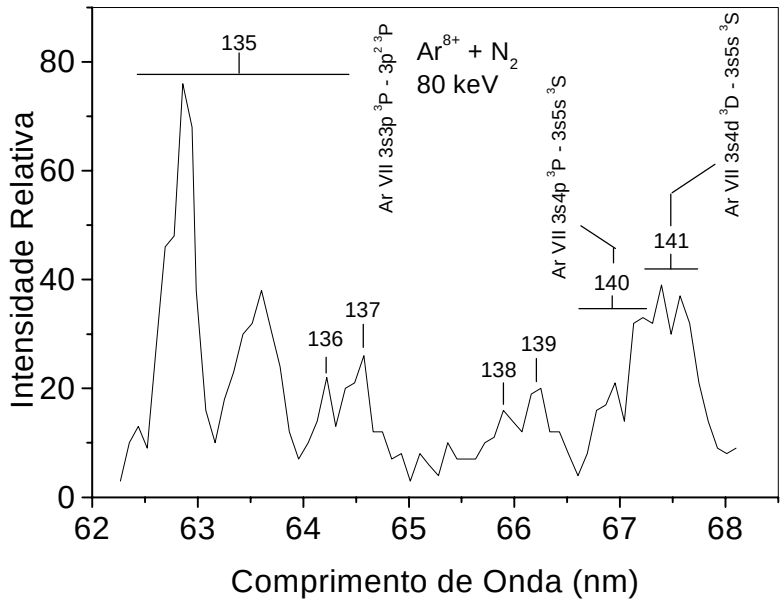

Espectro de EUV para colisões de Ar^{8+}+N_2 no intervalo de comprimento de onda de aproximadamente 62 ate 68 nm. As linhas dominantes são do projetil.

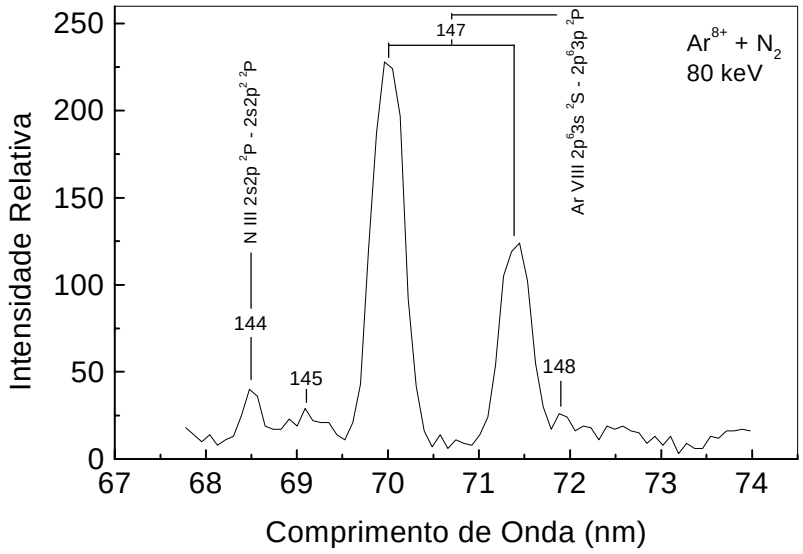

Espectro de EUV para colisões de Ar^{8+}+N_2 no intervalo de comprimento de onda de aproximadamente 68 ate 74 nm. As linhas dominantes são do alvo e do projetil.

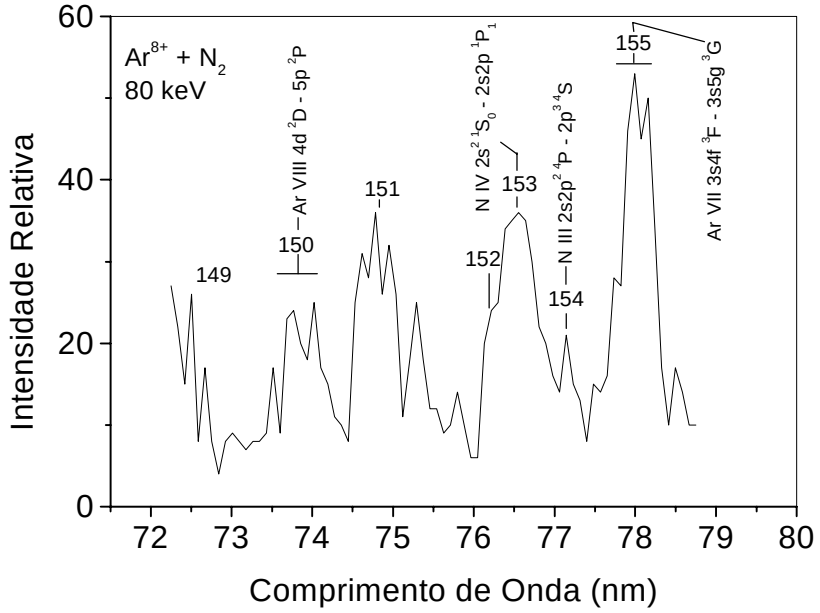

Espectro de EUV para colisões de Ar^{8+}+N_2 no intervalo de comprimento de onda de aproximadamente 72 ate 79 nm. As linhas dominantes são do alvo e do projetil.

Referências Capitulo 4

[1] McGuire, J.H., *Electron Correlation Dynamics in Atomic Collisions, Cambridge University Press* (1997).

[2] Fuelling, S., *et al. Phys. Rev. Lett.* **68** 3152 (1992).

[3] Bliman, S. *et al., Phys. Rev A,* **46** 1321 (1992).

[4] Zou, Y., *et al., Phys. Scr.* **T73** 79 (1997).

[5] Kambara, T, *et al., J. Phys. B* **31** L909 (1998).

[6] Meyer, F.W., *et al., Nucl. Instrum. Methods Phys. Res. B* **24/25** 106 (1987).

[7] Remscheid, A. et al., J.Phys. B 29 515 (1996).

[8] Shiromaru, H. et al, Phys. Scr. **T80** 110 (1999).

[9] Bliman, S., *et al., Phys. Rev. A.*, **60** 1 (1999).

[10] Bruch, R, *et al., Surf. Interface Anal.*, **27** 236 (1999).

[11] Bruch, R., *et al., Rev. Sci. Instrum.*, **68** 1091 (1997).

[12] Fülling, S. *Ph.D. Thesis*, UNR, Reno, NV USA (1991).

[13] Cowan, R.D., *The Theory of Atomic Structure and Spectra*, Univ. of California Press (1981).

[14] Kelly, R.L., *Atomic and Ionic Lines Below 2000 Å, H through Ar* (1982*).*

CAPITULO 5 :

Conclusão Geral e Perspectivas Futuras

Os resultados de He I (1snp) $^1P^0$ (n=2-5) e He II (np) $^2P^0$, apresentados para a excitação mais a excitação-ionização do hélio pelo impacto de próton neste estudo, representam as primeiras medidas detalhadas da polarização destes estados. Nós fornecemos a evidência que as emissões de EUV de He I e de He II associados com os mecanismos de poucos corpos conduzem às frações completamente diferentes da polarização para os sistemas da colisão do próton e do elétron. Estes valores fundamentalmente diferentes poderiam ser usados como diagnostico na análise dos "solar flares", onde tais projeteis positivamente e negativamente carregados são os mais abundantes.

Em comparação com cálculos teóricos, o B1 (first Born) não reproduz os dados da polarização para o impacto do próton no caso da excitação (He I). Cálculos mais elaborados (AOCC) mostram uma convergência melhor, embora o acordo total não seja ainda inteiramente satisfatório com respeito aos resultados experimentais. Daqui, cálculos mais detalhados, usando AOCC e outros métodos, são planejados.

No caso da excitação-ionização (He II) nenhuma teoria detalhada existe, porem nossos dados podem ser usados como referencia para testar aproximações teóricas mais avançadas que incorporam pouca dinâmica do corpo.

Experiências adicionais são atualmente executadas para investigar projeteis moleculares dos íons (H_2^+ + He e H_3^+ + He) para elucidar os processos mais complexos.

No caso do trabalho sobre Si IV nós completamos mais um trabalho na série do silício. Agora falta o trabalho sobre Si I planejado no futuro próximo e sobre Si XIV, nesse caso como não

existem dados experimentais são planejados experimentos em Lund, Suécia, com a intenção de publicar uma compilação completa sobre o silício, que é um elemento importante na astrofísica.

Nós estudamos processos simples e múltiplos de captura de elétron em colisões lentes de 80 keV entre Ar^{8+} e nitrogênio molecular usando a espectroscopia de EUV. No caso das linhas medidas de Ar^{6+} e Ar^{7+} são planejados trabalhos de cálculo teórico de forças de osciladores ponderadas e tempos de vida. Os processos exóticos da captura de até seis elétrons na colisão poderiam explicar os estados ionizados altamente excitados de Rydberg observados do nitrogênio do tipo $N^{2+}(1s^2 2s2lnl')\ ^{2,4}L$, n=2-10 and $N^{3+}\ (1s^2 2lnl')\ ^{1,3}L$, n=2-5 . Assim, a captura de quatro elétrons pode conduzir à produção de ions excitados de N^{2+*}. Se cinco elétrons forem capturados, este pode conduzir à criação de estados excitados de N^{2+*} e N^{3+*}. Visto que, na reação da captura de seis elétrons, muito provavelmente são criados ions excitados de N^{3+*} Estes resultados são consistentes com nossas intensidades relativas medidas das linhas do alvo. Para completar o presente trabalho são planejados experimentos de "target ion TOF (time-of-flight) spectrometry" em futuro proximo.[1]

Referências Capitulo 5

[1] Private communication: Prof. Samuel Bliman: Université de Marne la Vallé, France

Apêndice

- Trabalho 1: "Investigation of Excitation and Ionization-Excitation of He Following Electron and Proton Impact Using EUV Polarimetry."
  Accepted for publication in Proceedings of SPIE 12/2000, Vol. 4139

- Trabalho 2: "Weighted Oscillator Strength and Lifetimes for the Si IV Spectrum."
  Accepted for publication (May 2000) in Journal of Quantitative Spectroscopy and Radiative Transfer.

- Trabalho 3: "EUV Photon Emission Spectroscopy For Diagnostics Of Single And Multiple-Electron Capture Processes In 80 keV Ar^{8+} + N_2 Collisions."

- Trabalho 4: "Auger and Radiative Decay of Triply Excited States of Li, Be^{+}, and B^{2+} Projectiles Following Ion-Atom and Ion-Molecule Interactions."

- Trabalho 5: "Non-statistical Magnetic Substate Populations and Cross Sections Following the Excitation of Helium by Electron and Proton Impact."

Trabalho 3-5: Submitted to: 16th International Conference on the Application of Accelerators in Research and Industry CAARI 2000, November 1-4, 2000, University of North Texas, Department of Physics, Denton, Texas, USA. The Proceedings of the 16th International Conference on the Application of Accelerators in Research and Industry will be published in April, 2001 by the American Institute of Physics.

- Trabalho 6: "Development of x-ray and extreme ultraviolet (EUV) glass capillary optical devices for diagnostics and instrumentation for various sensing and diagnostics applications".
  Published in: Proceedings for the 7th International Symposium on Recent Advances in Microwave Technology (ISRAMT'99) , 13-17 December 1999 in Malaga, Spain.

Investigation of Excitation and Ionization-Excitation of He Following Electron and Proton Impact Using EUV Polarimetry

H. Merabet[a*], A. Siems[b], R. Bruch[a], J. Hanni[a], M. Bailey[c], H.C. Tseng[d], C.D. Lin[e], A. G. Trigueiros[b]

[a] Department of Physics, University of Nevada Reno, Reno NV 89557 USA,
[b] Instituto de Física, Universidade Estadual de Campinas (Unicamp), 13083-970 Campinas, São Paulo, Brazil,
[c] Atmospheric Science Center, Desert Research Institute (DRI), Reno NV 89506 USA,
[d] Department of Physics, Chung Yuan Christian University, Chung Li, Taiwan 32023,
[e] Department of Physics, Kansas State University, Manhattan, KS 66506-2601 USA

ABSTRACT

A detailed investigation of excitation of He ($1s^2$) ^1S to He ($1snp$) $^1P^o$ (n=2-5) states and ionization-excitation of He ($1s^2$) ^1S to He ($2p$) $^2P^o$ and He ($3p$) $^2P^o$ states in e^- + He and H^+ + He collision systems is presented for a wide range of projectile velocities $(2.2\,\text{a.u.} < v < 6.9\,\text{a.u.})$. Specifically, new experimental data are presented on measurements of the degree of linear polarization for excitation and excitation-ionization of He following proton impact in the extreme ultraviolet (EUV) wavelengths. These measurements have been performed using a characterized molybdenum/silicon multilayer mirror polarimeter (MLM) whose polarization characteristics have been optimized for EUV emission of He and He^+. Furthermore, the proton experimental results are compared with theoretical polarization data using the first Born approximation and recent atomic orbital close coupling (AOCC) calculations for the excitation process. A comprehensive comparison of experimental data for negatively and positively charged projectiles at equal impact velocities is also given in order to elucidate differences in the collision mechanisms of two electron targets. It is important to note that these results are relevant for astrophysical diagnostics such as solar flares.

Keywords: EUV radiation, Degree of Linear Polarization, Electron and Proton Impact on He, Multilayer Mirror, Polarimeter

1. INTRODUCTION

Experimental and theoretical investigations of electron and proton impact on atoms are of considerable importance for our understanding of many body collision dynamics. In particular, electronic processes in few body atomic collision complexes such as helium are of great significance both from a fundamental and an applied point of view. The helium atom is the second most abundant element in the universe and it is the simplest strongly bound two-electron system. For these reasons this atom is ideally suited for the study of collision dynamics and correlation effects[1-5] in ion-atom collisions. Furthermore, radiative emissions from singly charged ions such as He^+ have been observed in solar spectra under solar-flare conditions[6]. Hence, study of such complex non-equilibrium, anisotropic, beam-like systems may provide a deeper understanding of electron and/or proton induced jets in solar flare astrophysical investigations[7-8].

When a negatively or positively charged projectile collides with a helium atom at intermediate and high impact energies, the dominant collision mechanisms are excitation and simultaneous ionization-excitation of the target with subsequent detection of photons and/or ejected electrons[9-10]. The emitted radiation from line transitions between magnetic sublevels is linearly polarized when observed at 90 degrees with respect to the quantization axis defined by the projectile beam. This is due to the non-isotropic, non-Maxwellian distribution of electron population between the sublevels (i.e., level population alignment). In turn, this alignment effect results in polarized line emission which can be characterized by the degree of linear polarization *P* defined by,

$$P = \frac{I_{\parallel} - I_{\perp}}{I_{\parallel} + I_{\perp}} \tag{1}$$

* For further information and correspondence:
Phone: (775) 784 1335, Fax: (775) 784 1398, email: hocine@physics.unr.edu.

where $I_{\parallel}$ is the intensity of radiation with electric field vectors oriented along the beam axis (z axis) and $I_{\perp}$ is the intensity of radiation perpendicular to the quantization axis (y axis) as shown in Fig.1 [11-12]. In addition, the x axis points along the direction of observation (radiation from dipoles oriented along this axis is not observed). The measurement and analysis of the degree of polarization or the angular distribution of the photon emission can therefore reveal the anisotropy of the emitting source.

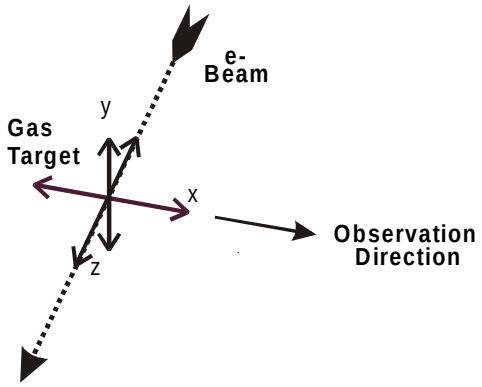

Fig. 1: Schematic representation of a distribution of electric dipoles for an ensemble of excited atoms or ions in the x, y and z directions.

The present work is a detailed investigation of excitation of He to (1snp) $^1P^o$ (n=2-5) states and ionization-excitation of He to (2p) $^2P^o$ and (3p) $^2P^o$ states in e^- + He and H^+ + He collision systems for a wide range of projectile velocities $(2.2\,\text{a.u.} < v < 6.9\,\text{a.u.})$ using our polarization analysis technique. Specifically, such states can be principally formed by the following reaction channels:

$$e^- + He\,(1s^2)\,{}^1S \rightarrow He\,(1snp)\,{}^1P^o + e^- \\ \lfloor\!\rightarrow He\,(1s^2)\,{}^1S + h\nu, \tag{2}$$

$$H^+ + He\,(1s^2)\,{}^1S \rightarrow He\,(1snp)\,{}^1P^o + H^+ \\ \lfloor\!\rightarrow He\,(1s^2)\,{}^1S + h\nu, \tag{3}$$

involving the emission of radiation with wavelengths from λ=517 to 584 Å for n=2 to 5, respectively;

and

$$e^- + He\,(1s^2)\,{}^1S \rightarrow He^+\,(np)\,{}^2P^o + e^- + e^- \\ \lfloor\!\rightarrow He^+\,(1s)\,{}^2S + h\nu, \tag{5}$$

$$H^+ + He\,(1s^2)\,{}^1S \rightarrow He^+\,(np)\,{}^2P^o + H^+ + e^- \\ \lfloor\!\rightarrow He^+\,(1s)\,{}^2S + h\nu, \tag{6}$$

involving the emission of Lyman-α radiation (n=2) at λ=304 Å and the 256 Å emission from HeII (3p) $^2P^o$. In the following, we will use spectroscopic notation, i.e., the neutral helium will be labeled "HeI" and the ionized helium (He^+) will be labeled "HeII". A schematic energy-level diagram for the states of HeI and HeII is shown in Fig.2, where the wavelengths of the strongest emission lines of the HeI (1snp) $^1P^o \rightarrow (1s^2)\,{}^1S$ and HeII (np) $^2P^o \rightarrow (1s)\,{}^2S$ series are indicated.

In this study, intensive polarization measurements for the extreme ultraviolet (EUV) emission have been performed. The photoemission has been measured for proton impact on He from 121 keV to 1.19 MeV (2.2. a.u.< v <6.9 a.u.) and compared with previous electron impact polarization results at equal velocities. The optical device used for these experiments is a multilayer mirror (MLM) polarimeter (see Fig. 4) whose reflection characteristics have been optimized for the HeI and HeII emission in the EUV wavelength range[13].

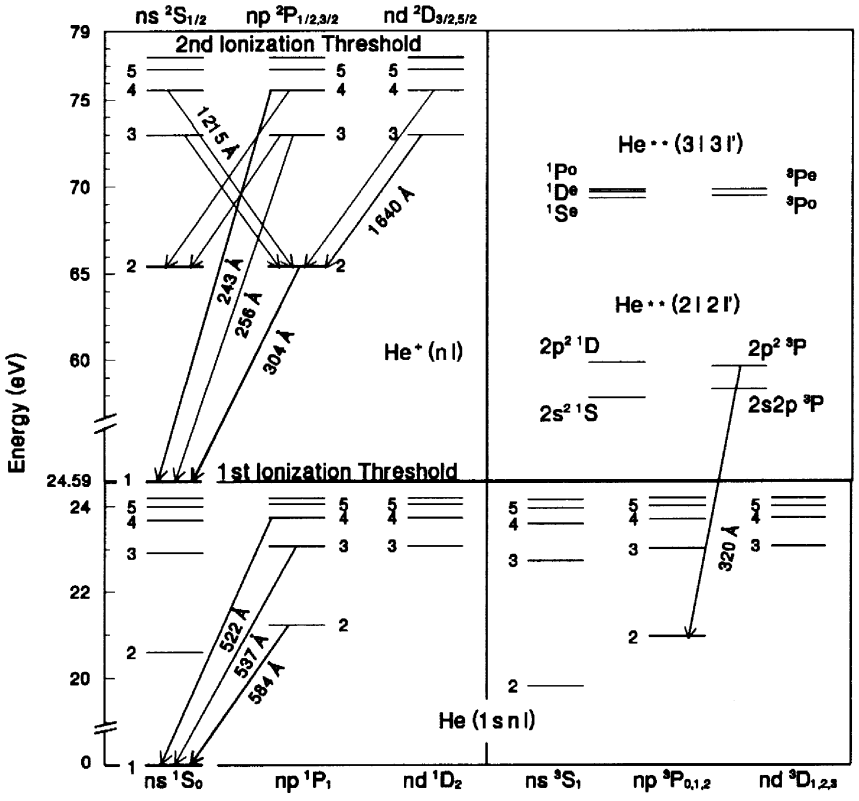

Fig.2. Energy-level diagram for the excited states of neutral and ionized helium

In the following, we first describe the experimental setup, including the MLM polarimeter (Section 2) and the 1.5 m grazing incidence monochromator used for optical filters characterization. Then, in Section 3, we discuss our experimental results and compare the degree of linear polarization for electron and proton projectiles at equal velocities for both excitation and ionization-excitation mechanisms. Moreover, a comparison with theoretical predictions, namely the first Born approximation[14] (FBA) and atomic orbital close-coupling[15-16] (AOCC) calculations, is presented in the case of the excitation process.

2. EXPERIMENTAL SETUP

2.1. The Apparatus

A schematic view of the experimental apparatus used for polarization measurements utilizing our 2 MV Van de Graaff accelerator is shown in Fig. 3. The protons were extracted from an RF-ion source and accelerated by means of the 2 MV Van de Graaff. These ions were focused and steered by a magnetic quadrupole doublet lens into a stable and intense beam, which was then mass and momentum analyzed. After passing through a slit control system they entered the target chamber where they were collimated before traversing the differentially pumped gas cell containing the helium gas and were finally collected by a Faraday cup for charge normalization (see Fig. 4). The Van de Graaff accelerator has been energy calibrated using the well energy defined nuclear reaction $F^{19}(p,\alpha\,\gamma)O^{16}$ resonance at 340.0 ± 0.3 keV[17] and 872.11 ± 0.2 keV[17]. This way, proton energies are known within a 1% uncertainty.

The experimental setup includes three main components: (1) the EUV polarimeter; (2) the internal electron gun or the external Van de Graaff accelerator beam-line, the target cell, and a Faraday cup; and, (3) an intensity calibrated 1.5 meter grazing incidence monochromator. The polarimeter consists of the Mo/Si MLM optical element (see Fig. 4), a channeltron detector, spectral filter, and a rotational base. The MLM is mounted on a wedge, which fixes the angle of incidence with respect to the mirror surface. A removable aperture, which holds a VYNS-3 spectral filter or an Aluminum/Titanium (Al/Ti) filter, manufactured by Luxel Corp.[18], is mounted in front of the MLM. This aperture restricts the angle of incidence to within $\pm 1^0$, corresponding to a wavelength bandwidth of the order of 12 Å at 304 Å. The system is described in more details by Bailey *et al.*[9,13]

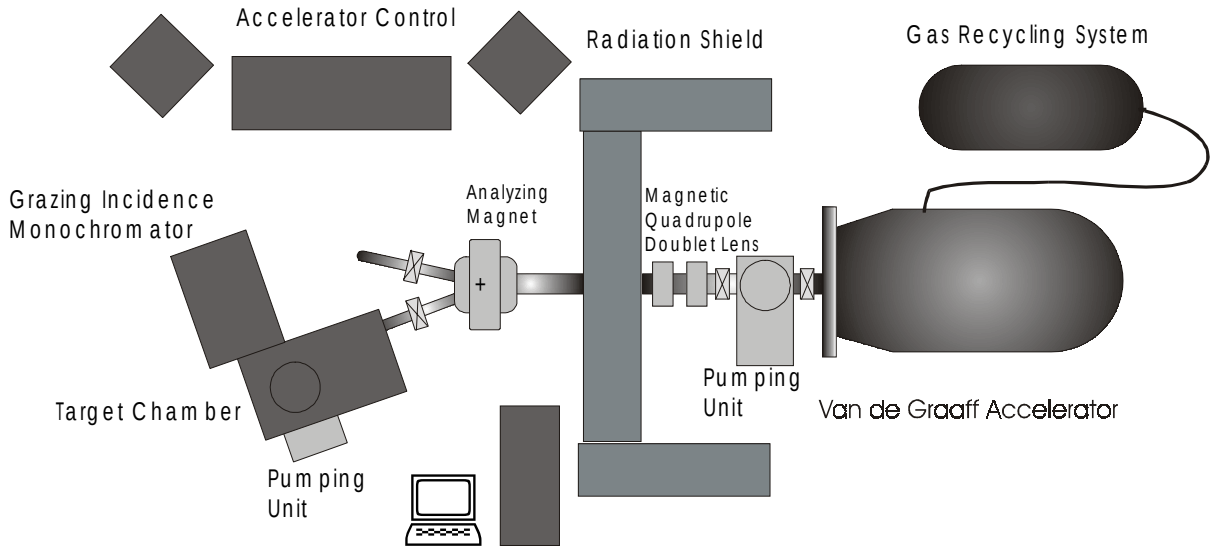

Fig. 3: The University of Nevada Reno Van de Graaff accelerator, target chamber and EUV monochromator.

The MLM and EUV filter are fixed in a box that was shielded with aluminum foils in order to prevent stray light and particles from entering the polarimeter. One side of the box containing the mirror is open to accommodate a channeltron detector mounted in a separate housing. Two different wedges were used with this setup to provide an angle of 50 for measuring Lyman-α (HeII (2p) $^2P^o$) emission and an angle of 40^0 used to measure HeII (3p) $^2P^o$ and HeI (1snp) $^1P^o$ emissions. In addition, the position of the detector housing could be varied in order to adjust for different angles of incidence and reflection.

The MLM and detector housing are mounted to a precision rotational base. This rotational base is driven by a small vacuum compatible stepping motor. The angular position of the polarimeter is monitored with a calibrated potentiometer placed on the rotational axis of the mirror mount. The compact polarimeter can be rotated with incremental steps of 0.2 degrees. For the purposes of alignment, the rotational base is attached to an adjustable mount, which can move in three mutually perpendicular directions. Alignment of the polarimeter is easily achieved by removing the potentiometer and spectral filter and viewing the emission window of the gas cell through a small channel drilled in the base of the mirror housing. This channel is coaxial with the axis of rotation and the removable aperture in front of the filter. After traversing the target region, the projectile beam was collected in a Faraday cup for normalization purposes.

2.2. Pressure Dependence of the Degree of Linear Polarization

Collisional excitation, absorption processes, and repopulation due to secondary collisions may affect the observed degree of linear polarization. Consequently, a detailed pressure dependence of the emission from both excited and ionized-excited helium was obtained with the EUV grazing incidence monochromator and the MLM polarimeter. In Fig. 5, we have indicated the polarization fraction for 60 eV e^- + He and 220 keV H^+ + He collisions as a function of the target pressure corresponding to the excitation process. In this case, the polarization fraction exhibits a gradual change when the He pressure becomes greater than 1 mTorr. However the polarization appears to reach a constant value for pressures at 1 mTorr and below. Therefore a gas pressure of 1 mTorr was adopted for the HeI (1snp) $^1P^o$ decay for polarization measurements following electron impact on He whereas a pressure of 0.25 mTorr was used before for the electron impact case[19]. The corresponding pressure dependence of the polarization fraction for the 304 Å radiation, associated with ionization-excitation of He by electron and proton impact, is depicted in Fig. 6. This figure exhibits the corresponding polarization target pressure dependence for 220 keV proton impact on He and 69 eV electron impact for the 304 Å HeII emission corresponding to the ionization-excitation mechanism. It is clearly seen that this polarization fraction is constant between 1 and 37 mTorr for protons while it shows a strong decrease above 1mTorr for electron projectiles. Therefore, these two collision systems present different collisional mechanisms. This may be expected since protons are much heavier than electrons, thus they involve smaller scattering angles during the collisions. Consequently, a gas pressure of 30 mTorr and 1 mTorr were used for this type of measurements for proton and electron impact, respectively.

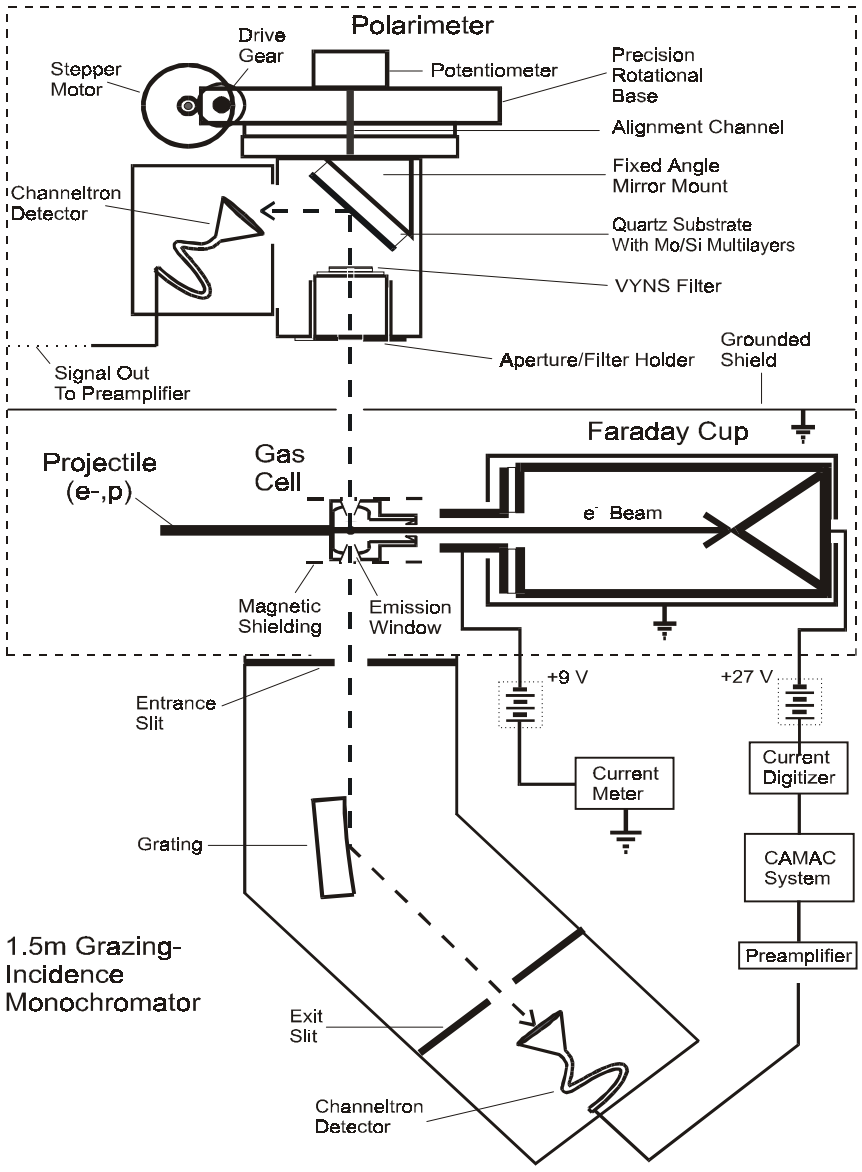

Fig.4. Schematic view of the apparatus and data acquisition used for polarization measurements.

Since sufficiently strong magnetic fields can lead to a depolarization of the observed radiation by the Hanle effect, the gas cell used in this study was mounted inside a cylindrical magnetic shielding. With this shielding at the interaction region of the gas target a magnetic field smaller than 0.05 Gauss was achieved [19].

2.3. Optical Filters

In order to accurately measure the EUV polarization of HeII radiation following electron and proton impact on He, it is necessary to suppress the dominant HeI emission. To obtain the necessary selectivity between these two spectral regions, a filter material known as VYNS-3 [13] was used. This VYNS-3 is a copolymer material containing a 90% vinyl chloride, 10% vinyl acetate mixture and is produced by Union Carbide (VYNS-3 is a specific formula of this copolymer) [20].

In particular, the effect of filter thickness and absorption was explored. The energy region for this comparison was chosen such that the polarization fraction was nearly constant. The $(2p)\ ^2P^o$ threshold measurements performed in the earlier study of

electron impact on He were initially obtained with a 25% VYNS transmission filter [20], providing a 1000:1 transmission ratio for 304 Å radiation versus the dominant 584 Å radiation from neutral helium. However, a review of our detailed electron impact differential cross section data for the excitation of the HeI (1s2p) $^1P^o$ and HeII (2p) $^2P^o$ levels of neutral and ionized helium revealed that the ratio of these cross sections at energies just slightly above the HeII (2p) $^2P^o$ threshold exceeds by far 1000:1[11-13]. Hence a 25% transmission filter would transmit roughly equal amounts of HeI (1snp) $^1P^o$ and HeII (2p) $^2P^o$ emission intensities. Therefore, this type of filter is not adequate for an accurate determination of the threshold polarization and associated alignment parameter. We further note that a 10% VYNS transmission filter provided a transmission ratio of 100,000:1 insuring that the polarization measured with this filter contained only a 1% contamination due to the HeI (1snp) $^1P^o$ decays at threshold.

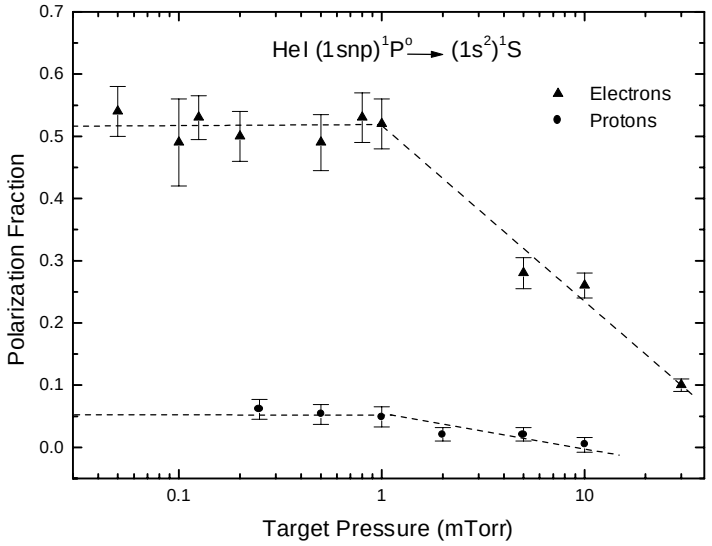

Fig. 5: Gas target pressure dependence of the HeI radiation following 60 eV electron impact on He and 220 keV proton impact on He measured with the EUV MLM polarimeter.

For EUV polarization measurements of HeI radiation following electron impact, no filter was necessary because the HeII emission contribution is negligible in comparison with HeI emission. On the other hand, the HeI polarization measurements for proton impact were not possible without a filter because of the high background due to scattered electrons, protons and recoil ions, in addition to the low HeI to HeII excitation cross sections ratio[9]. Hence a Al/Ti filter with a two to one HeI/HeII transmission ratio was used for these measurements[18].

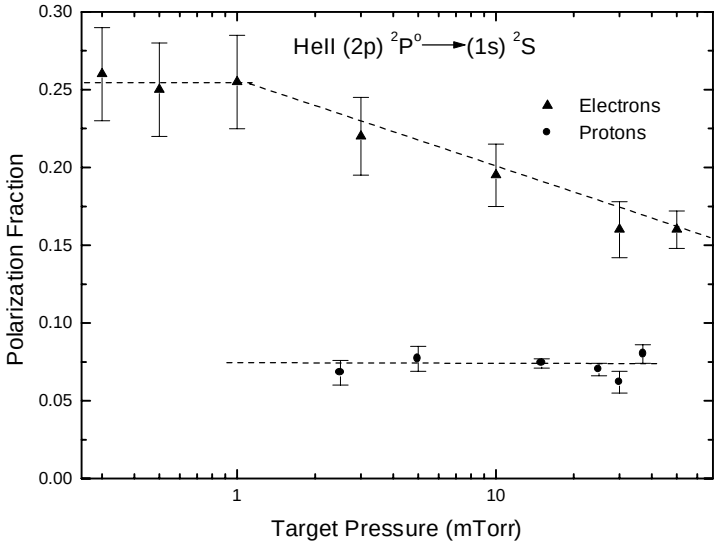

Fig. 6: Gas target pressure dependence of the 304 Å HeII radiation following 69 eV electron impact on He and 220 keV proton impact on He measured with the EUV MLM polarimeter.

3. RESULTS AND DISCUSSION

Before discussing our experimental results, we provide here the most relevant polarization expressions from Percival and Seaton[12] and their relations to the corresponding integral alignment parameter, A_0,

$$P(^1P^0) = \frac{\sigma(0) - \sigma(1)}{\sigma(0) + \sigma(1)} = \frac{3A_0}{A_0 - 2} \tag{7}$$

$$P(^2P^0) = \frac{3(\sigma(0) - \sigma(1))}{7\sigma(0) + 11\sigma(1)} = \frac{3A_0}{A_0 - 6} \tag{8}$$

where $\sigma(0)$ and $\sigma(1)$ are the magnetic subcross sections for the $M_L = 0$ and $M_L = \pm 1$ magnetic substates in LS coupling.

In the following a short description of the atomic-orbital close-coupling (AOCC) calculations is given while full details are given elsewhere [15]. Then, the proton polarization data are discussed and compared with measurements associated with impact electron on He at equal velocities (2.2 a.u. < v < 6.9 a.u.) for both excitation and ionization-excitation of helium.

3.1. Atomic –Orbital Close-Coupling (AOCC) calculations for H^+ + He collisions

For H^+ + He collisions the excitation cross sections and polarization fractions for He (1snp) $^1P^o$ states are calculated using the standard close-coupling expansion method. By treating the Schrödinger equation for the two electrons in the Coulomb fields of the two moving nuclei, one expands the time-dependent wavefunction in terms of the eigenstates of He. In the energy region under study, charge transfer processes are not important such that the basis functions included are all centered around the target atom. In other words only the helium eigenstates are used in the expansion. Following the standard procedure, the resulting expansion coefficients satisfy a system of linear first-order differential equations for each collision impact parameter. The excitation cross section to each magnetic substate is calculated by integrating the excitation probability P(b) over the impact parameter plane. Details of such calculations can be found in the review by Fritsch and Lin[15]. In this calculation, basis states consist of singly excited states up to n=3 and some pseudostates for each total angular momentum L.

3.2. HeI (1snp) $^1P^o$ Polarization

The HeI (1snp) $^1P^o$ polarization data measured earlier for electron impact energies ranging from 22 to 350 eV are shown in Fig. 7. These data have been obtained taking advantage of the surface reflectivities of our polarimeter. Included in this figure are the previous experimental results of Hammond *et al.*[21] which extend down to 0.8 eV above threshold at 22 eV. The comparison with the earlier work of Hammond *et al.* demonstrates the accuracy and reliability of our MLM EUV polarimeter in the wavelength region above 500 Å. The measured polarization is observed to drop rapidly from unity close to threshold to a value of approximately 0.48 at 25 eV. The polarization rises again to a secondary maximum value of approximately 0.57 at 40 eV and then decreases gradually with increasing electron impact energy.

As can be seen, our results are in excellent agreement with the earlier measurements of Hammond and co-workers measured with errors of less than 1%. Included in the figure are first Born approximation calculations[14] which show very good agreement with both experimental data sets even at a low impact energy of 80 eV. In Fig. 7, we have also plotted more elaborate theoretical results obtained using the first-order many-body theory (FOMBT) by Csanak *et al.*[30]. Again, these theoretical data match very well our experimental polarization fraction at energies close to threshold while they agree with the first Born at relatively higher energies.

The polarization data for excitation of He near threshold exhibits two interesting features. First, the threshold model for single excitation of helium predicts a threshold polarization value equal to one, *i.e.* $\sigma(M_L=\pm1) = 0$ at threshold corresponding to a pure s wave for the outgoing electron[23-24]. This prediction has been verified experimentally by Norén *et al.*[25]. Second, the pronounced dip in the polarization at an impact energy of 25 eV appears to coincide with the peak of the cross section for the production of metastable helium (1s2s) ^1S and (1s2s) ^3S states measured by Mason and Newell[26]. A similar feature is observed in the HeII polarization data from this work at the threshold energy for the ionization-excitation of helium (see section 3.3). From these and other observations of polarized EUV light[12], it is clear that the polarization can be noticeably affected by the presence of competing excitation channels arising from core excited or doubly excited states decaying in a first step via autoionization to an excited residual state which is subsequently depleted via E1 emission.

Now, let us consider the H^+ + He collision system. The HeI (1snp) $^1P^o$ polarization results from this study for the full range of impact velocities, corresponding to an energy range from 121 keV to 1.19 MeV proton impact, are shown in Fig.8.

The corresponding previously obtained electron polarization data[12] are also depicted in this figure for comparison. Both sets of experimental data have not been corrected for cascade effects. It is evident from Fig. 8 that the degree of linear polarization behaves differently for electron and proton impact. While the polarization fraction following electron impact reaches more than 50% at a velocity of about 2 a.u., it decreases to 7% in the proton case. Furthermore, the two sets of experimental data exhibit a zero value of the degree of *P* at distinct impact velocities when comparing electron with proton projectiles. At higher energies, we have found a more pronounced decrease of the polarization fraction in the case of protons below 7 a.u. impact velocities, whereas the polarization results corresponding to electrons appear to have clearly smaller polarization values.

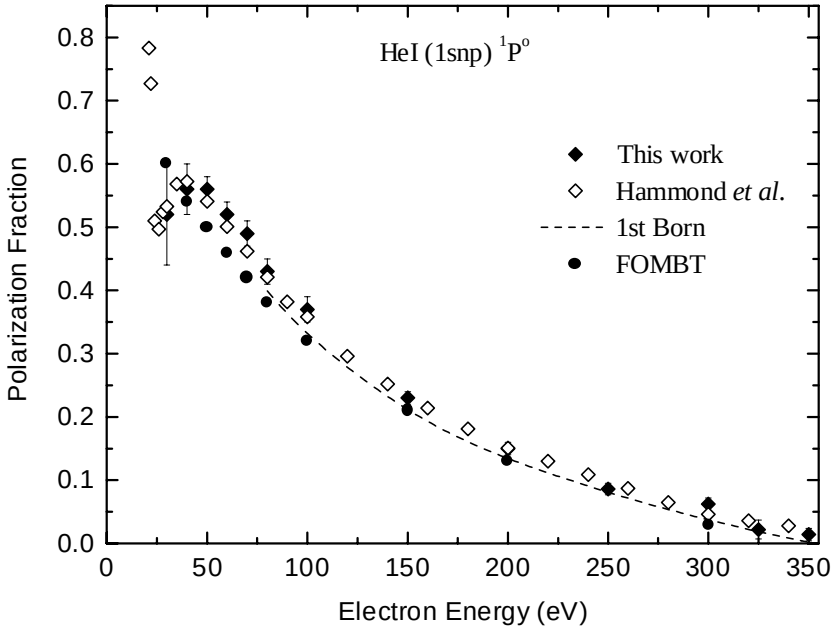

Fig. 7. Polarization fraction of HeI(1snp) $^1P^o \rightarrow (1s^2)\ ^1S$ radiation as function of the electron impact energy ranging from 22 to 350 eV.

The electron HeI polarization data have been found to agree well with the first Born approximation (see Fig. 7). Hence, we might expect a similar trend for H^+ + He collisions system. In Fig. 9, we have replotted the HeI proton experimental results along with first Born approximation and our more advanced theoretical calculations, based on the atomic-orbital close coupling (AOCC) method. As can be seen from this figure, although both theoretical results predict a like velocity dependence when compared with our experimental polarization fraction, neither the first Born nor the AOCC reproduces our measurements. It is interesting to note that our polarization data approach zero at an impact velocity of 3.5 a.u.; whereas P=0 for the AOCC prediction occurs at about 4 a.u. This velocity shift corresponds to a 90 keV difference for the proton impact energies, which exceeds by far our experimental energy uncertainty (ΔE = 8 keV at 400 keV, see Section 2.1).

It is evident from Fig. 9 that the AOCC theory deviates at low energies from the first Born approximation and better approaches our experimental results. We further note that deviations observed between our measurements and theoretical data is relevant at these lower impact energies. The AOCC results presented here are performed with limited excited target states. A more accurate calculation, including more target states may improve the convergence to the experimental data. Such more sophisticated calculations are now being performed. At high impact velocities, up to 7 a.u. corresponding to 1.19 MeV proton impact, AOCC results show a better agreement with experiment than first Born.

It is known that the first Born approximation is generally well suited to describe the excitation cross sections of helium by both electron and proton impact[5,16,27-28] in the high impact energy limit. Nonetheless, experimental deviations from the first Born theory predictions have been observed in the measured polarization for the (1s3p) $^1P^o \rightarrow$ (1s2s) ^1S transition and in several (n=4 $\rightarrow$ n=2) and (n=3 $\rightarrow$ n=2) transitions in helium which occur in the visible and near ultraviolet wavelength region[29,30]. This effect may be partially due to transfer of alignment via cascades from higher lying states[31].

In summary, we have shown in this section that the degree of linear polarization strongly depends on the charge sign for electrons and protons projectiles. These very interesting results may be used as a new diagnostic tool for solar flare studies and other plasma physics and astrophysical applications.

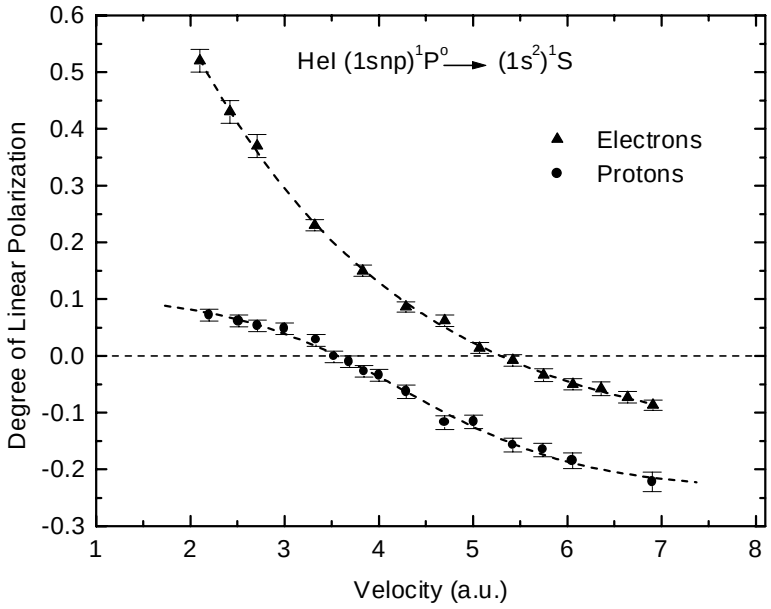

Fig.8. Polarization of HeI (1snp) $^1P^o \rightarrow (1s^2)\ ^1S$ radiation as a function of projectile velocity for electron and proton impact. The dashed lines are provided to guide the eyes.

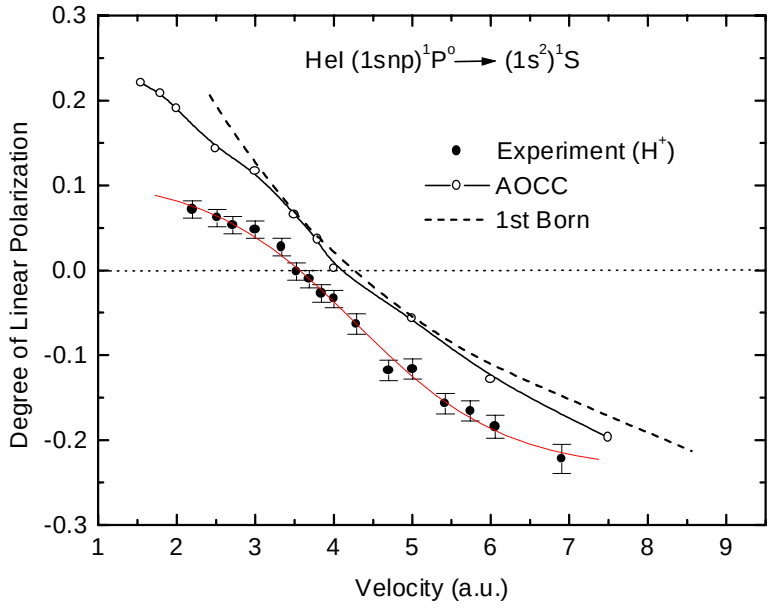

Fig.9. Polarization of HeI (1snp) $^1P^o \rightarrow (1s^2)\ ^1S$ radiation as a function of projectile velocity compared with AOCC and first Born calculations. The polarization data are fitted in order to guide the eyes.

3.3. HeII (np) $^2P^o$ Polarization

The HeII (2p) $^2P^o$ and HeII (3p) $^2P^o$ polarization results along with their integral alignment parameters A_0 are depicted in Fig. 10, for proton impact on helium. The corresponding electron impact data are also included in this figure for comparison. The HeII (2p) $^2P^o$ polarization results in this figure have not been corrected for cascade effects because the partial magnetic substate cross sections for the higher HeII (nl) magnetic sub-states are not accurately known. However, due to the much

shorter lifetimes of the excited HeII states in comparison with those of HeI, cascade effects associated with magnetic substate repopulation are expected to be smaller than for HeI [5].

The HeII (2p) $^2P^o$ polarization results shown in Fig. 10 are slightly higher than those for the He (3p) $^2P^o$ level. Nevertheless, the two sets of data agree very well within our experimental uncertainties. Similar agreement was found in the case of electron impact on helium. This confirms the hypothesis that the degree of linear polarization is approximately

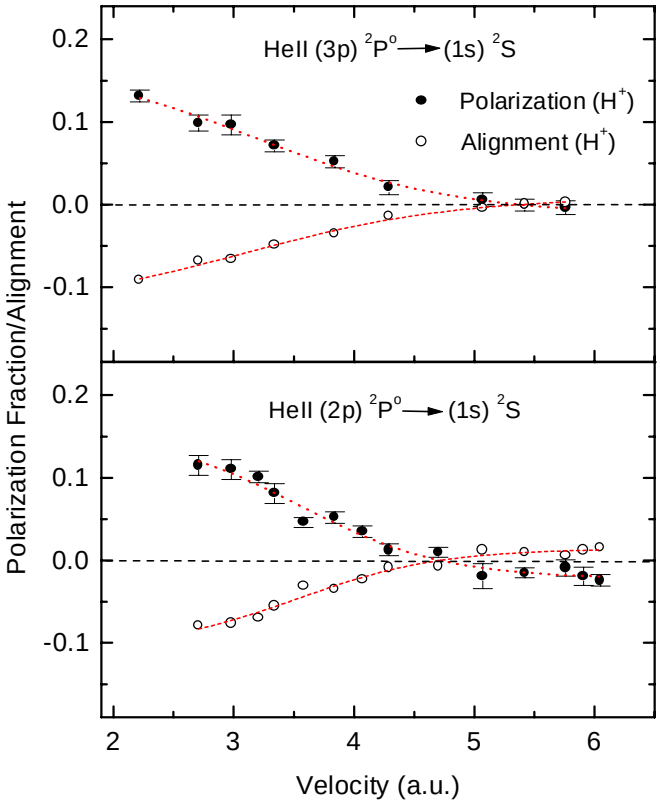

Fig. 10: Polarization fraction *P* and integral alignment parameter A_0 of HeII (np) $^2P^o \rightarrow$ (1s) ^2S radiation as a function of proton impact velocity. The dashed lines are plotted to guide the eyes.

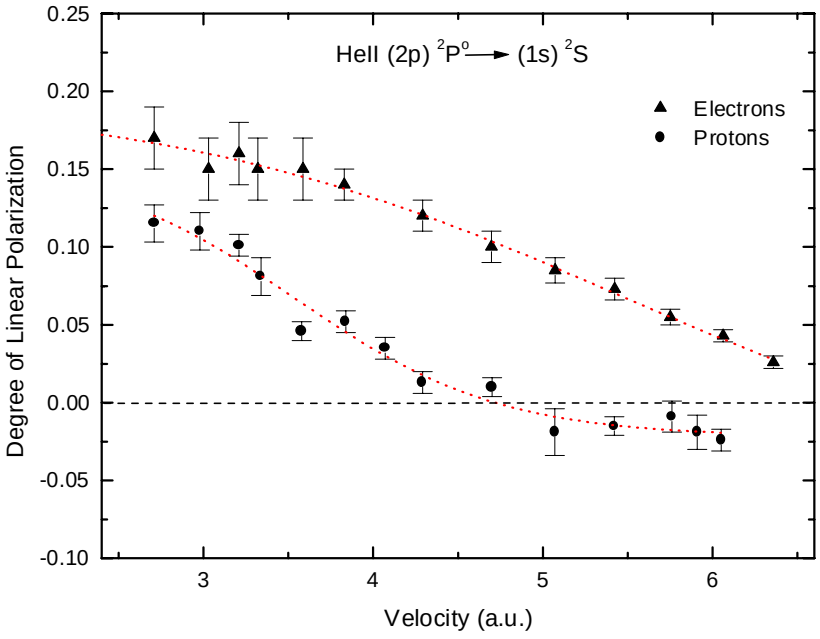

Fig. 11: Polarization fraction of HeII (2p) $^2P^o \rightarrow$ (1s) ^2S emission as a function of electron and proton impact velocities. The dashed lines are plotted to guide the eyes.

independent of the principal quantum number n. In contrast, the HeII (2p) $^2P^o$ polarization data for proton and electron projectiles (see Fig. 11) indicate pronounced differences. These prominent deviations may be understood in terms of second order Born contributions and coherent superposition of first and second order scattering amplitudes. Indeed, using a semi-empirical model based on the first and second Born approximation, Bruch *et al.*[31] were able to decompose the He^+ (np) (n=2-5) cross section data, summed over M_L=-1,0 and 1, in leading order terms which are proportional to Z_p^2, Z_p^3 and Z_p^4 where the Z_p is the projectile charge. In particular, these authors have found a strong Z_p^3 dependence, which may represent quantum interference effects. Such a strong Z_p^3 dependence may also affect the magnetic sub-level cross sections and, therefore, the observed degree of linear polarization following excitation plus ionization of helium by electron and proton projectiles. Furthermore, while both experimental polarization curves for electron and proton impact start with a positive value and decrease with increasing impact velocity until reaching negative values, the proton data are substantially different from the electron impact data for all collision velocities. In addition, the velocity dependence for HeI is completely different from the one for HeII states, *i.e.*, the mechanisms of excitation and ionization-excitation channels exhibit completely different angular distributions of the EUV emission. To our knowledge, no accurate theoretical calculations for He Lyman-α and β polarization have been performed using sophisticated many-body approach. The present study may serve as an important prototype test case for future more advanced theoretical calculations including few body dynamics such as excitation plus ionization of helium to this very interesting collision problem.

4. CONCLUSION

The degree of linear polarization of radiation from the decay of excited HeI (1snp) $^1P^o$, HeII (2p) $^2P^o$, and HeII (3p) $^2P^o$ states following proton impact on helium at EUV wavelengths has been measured, with a characterized Mo/Si multilayer mirror at a wide velocity range (2.2 <v< 6.9 a.u.). Such optical devices provide significantly enhanced reflectivities in this wavelength region in comparison with traditional optical flat mirrors.

While previously measured HeI (1snp) $^1P^o$ electron polarization fractions have been found to agree very well with first Born approximation below 7 a.u. impact velocities, this first order approach fails to reproduce the polarization data for proton impact associated with these singly excited states within the investigated velocity range. More elaborate calculations based on atomic orbital close-coupling (AOCC) show better convergence, although the overall agreement is still not fully satisfactory with respect to the experimental results. Hence, more detailed calculations, using AOCC and other methods, are envisaged. In this work, the comparison of the degree of linear polarization following excitation of helium by electron and proton projectiles exhibits completely different velocity dependence. Such prominent differences may be understood in terms of higher order Born contributions and coherent superposition of the scattering amplitudes as proposed by Bruch and co-workers[31] for the integrated excitation cross sections in the e- + He and H^+ + He collision systems. Especially, the observed Z_p^3 dependence may explain such alterations in the observed polarization fraction.

The HeII (2p) $^2P^o$ and (3p) $^2P^o$ results, presented for ionization plus excitation of helium in this study, represent the first detailed polarization measurements of these states. While no comprehensive theory exists for the simultaneous ionization-excitation mechanism following electron and proton impact, our data can be used as benchmark cases to test more advanced theoretical approaches incorporating few body dynamics. Moreover, we have provided evidence that both HeI and HeII EUV emissions associated with excitation and ionization-excitation mechanisms lead to completely different polarization fractions for the proton and electron collision systems. These fundamentally different values could be used as a new diagnostic tool in solar flare analysis, where such positively and negatively charged projectiles are most abundant. Additional experiments are currently underway to investigate molecular ion projectiles (H_2^+ + He and H_3^+ + He) to elucidate excitation and ionization-excitation processes of helium where the effects of multi-centered molecular projectile excitation and excitation-ionization will be explored.

ACKNOWLEDGMENTS

We would like to thank Dr. S. Fineschi from the Harvard-Smithsonian Center for Astrophysics for many interesting and fruitful suggestions. This project was supported in part by ACSPECT Corporation and Nevada Business and Science Foundation (NBSF), Reno Nevada.

REFERENCES

1. J.H. McGuire, *Electron Correlation Dynamics In Atomic Collisions*, Cambridge University Press, 1997.
2. N. Stolterfoht, C.C. Havener, R. A. Phaneuf, J. K. Swenson , S. M. Shafroth, and F. W. Meyer, "Evidence for correlated double-electron capture in low-energy collisions of $O^{6+}$with He*", Phys. Rev. Lett* **57**, pp. 74-77, 1986.

3. S. Fülling, R. Bruch, E.A. Rauscher, P.A. Neill, E. Träbert, P.H. Heckmann, and J.H. McGuire, “Ionization plus excitation of helium by fast electron and proton impact”, *Phys. Rev. Lett.* **68**, pp. 3152-3155, 1992.
4. J. Chesnel, H. Merabet, B. Sulik, F. Fremont, C. Bedouet, , X. Husson, M. Grether, and N. Stolterfoht, "Radiative stabilization following double electron capture in slow Ne^{10+} + He collisions", *Phys. Rev. A* **58**, pp. 2935-2943, 1998.
5. F.G. Donaldson, M.A. Hender, and J.W. McConkey, “Vacuum ultraviolet measurements of the electron impact excitation of helium”, *J. Phys. B.* **5**, pp. 192 , 1972.
6. S. A. Kazantsev, N.M. Firstova, A.V. Bulatov, A.G. Petrashen, J-C. Henoux, "Determination of proton's beam energy, manufactured in the solar flare, on the base of spectropolarimetry data", *Optics and Spectroscopy* **78**, pp. 729-737, 1995.
7. S. A. Kazantsev, N.M. Firstova,, A.G. Petrashen, J-C. Henoux, " Determination of the energy of electron beam based on of the spectropolarimetry of emission of Ellerman's bombs", *Optics and Spectroscopy* **82,** pp. 714-722, 1997.
8. S. Fineschi, J. M. Fontenla, P. MacNeice, N. N. Ljepojevic, "Electron impact polarization expected in solar EUV lines from Flaring Chromospheres/Transition regions", Proceedings of the Workshop on Max '91 /SMM Solar Flares: Observations and Theory, NO. **90-124**, pp.1-15, 1990.
9. M. Bailey, R. Bruch, E. Rauscher, and S. Bliman, “Cross sections for the ionization-excitation of helium by fast electrons and H^+, H_2^+, H_3^+ ions: (np) $^2P^o$ levels, n=2-5”, *J. Phys. B: At. Mol. Opt. Phys*. **28**, pp. 2655-2670, 1995.
10. W. C. Stolte and R. Bruch, " Cross sections for production of excited He^+ (np) $^2P^o$ states by 50-150 keV proton impact on helium", Phys. Rev. A **54**, pp.2116-2120, 1995.
11. H. Merabet, A. Siems, R. Bruch, S. Fülling, M. Bailey, "Ionization-excitation of He following electron and proton impact: a polarization study using an EUV polarimeter", SPIE Conference on Ultraviolet and X-Ray Detection, Spectroscopy and Polaremetry III, Denver, Colorado, July 1999, SPIE Vol. 3764, pp.2.12, 1999.
12. H. Merabet, M. Bailey, R. Bruch, D. V. Fursa, and I. Bray, J. W. McConkey, and P. Hammond, “A Polarization Study of the Extreme Ultraviolet Emission from Helium Following Electron Impact”, *Phys. Rev. A* **60**, pp. 1187-1198,1999.
13. M. Bailey, H. Merabet and R. Bruch, "Optical characterization of a compact multilayer mirror polarimeter in the extreme ultraviolet range", *Applied Optics* **38**, No. 19, pp.4125-4136, 1999.
14. L. Vriens and J.D. Carrière, "Analytical representations of generalized oscillator strengths excitation cross sections and polarization fractions", *Physica* **49**, pp.517-531, 1970.
15. W. Fritsch and C. D. Lin, "The semiclassical close-coupling description of atomic collisions--recent developments and results", *Phys. Rept.* **201**, pp.1-97, 1991.
16. H. Merabet, M. Bailey, R. Bruch, J. Hanni, S. Bliman, D. V. Fursa, I. Bray, K. Bartschat, H.C. Tseng, C.D. Lin "Cross Sections and Collision Dynamics of the Excitation of (1snp) $^1P^o$ Levels of Helium, n = 2-5, by Intermediate and High Velocity Electron, Proton, and Molecular Ion (H_2^+ and H_3^+) Impact", *Phys. Rev. A*, to be published, 2000.
17. J. B. Marion, "Accelerator calibration energies", *Rev. Mod. Phys*. **38**, pp.323-331, 1966.
18. Luxel Corporation, P.O. Box 1879, Friday Harbor, WA 98250.
19. M. Bailey, *Ph.D. Dissertation*, University of Nevada, Reno, 1997.
20. *Union Carbide Material Safety Data Sheet*, Union Carbide Chemicals and Plastics Company, Inc., Solvents & Coatings Materials Division, Danbury CT, 1992.
21. P. Hammond, W. Karras, A.G. McConkey, and J.W.McConkey, "Polarization of rare-gas radiation in the vacuum-ultraviolet region excited by electron impact: Helium and Neon", Phys. Rev. A. **40**, pp.1804-1810, 1989.
22. G. Csanak, D. C. Cartwright, S. Trajmar, "Magnetic-sublevel cross sections for excitation of the n ^1P levels of helium by electron impact", *Phys. Rev. A* **45**, pp.1625-1643, 1992.
23. 47. H. Klar and W. Schlecht, "Threshold multiple ionization of atoms. Energy dependence for double and triple escape", *J. Phys. B* **9,** pp.1699-1711, 1976.
24. P.L. Altick and T. Rösel, "Model-independent parameters for triply differential electron impact ionization cross sections at low energies", *J. Phys. B* **21,** pp.2635-2644, 1988.
25. C. Norén, J.W. McConkey, P. Hammond, and K. Bartschat, "Near-Threshold Study of the Polarization of He Resonance Radiation Using an Energy-Selected Electron Beam", *Phys. Rev. A*. **53**, pp.1559-1566, 1996.
26. N. J. Mason and W. R. Newell, "Total Cross Section for Metastable Excitation in the Rare Gases", *J. Phys. B* **20**, pp.1357-1377, 1987.
27. R. Hippler and K.H. Schartner, "Absolute cross sections for the excitation of n^1P^o-levels of helium by proton impact (150-100 keV)", *J. Phys. B* **7,** pp.618-625, 1974.
28. W.B. Westerveld, H.G.M. Heideman, and J. van Eck, "Electron impact excitation of 1 $^1S \rightarrow 2\ ^1P$ and 1 $^1S \rightarrow 3\ ^1P$ of helium: excitation cross sections and polarization fractions obtained from XUV radiation", *J. Phys. B*. **12,** pp.115-135, 1979.
29. S.C. McFarlane, " A Bethe theory for the polarization of impact radiation", *J. Phys*. B **7**, 1756-1762, 1974.
30. R.H. McFarland and E.A. Soltysik, " Polarization of light resulting from the excitation of helium by electrons", *Phys. Rev*. **127**, 2090-2096, 1962.

31. R. Bruch, L. Beigman, E. A. Rauscher, S. Fülling, J. H. Mcguire, E. Träbert and P. H. Heckmann, "Higher-order contributions to ionization plus excitation cross sections in high energy e- = He and H^+ + He scattering", *J. Phys. B* **26**, pp. L413-L417, 1993.

WEIGHTED OSCILLATOR STRENGTHS AND LIFETIMES FOR THE Si IV SPECTRUM

[a,*]A. Siems, [a]F. R. T. Luna, and [a,b]A. G. Trigueiros

[a]Instituto de Física "Gleb Wataghin", Universidade Estadual de Campinas, UNICAMP 13083-970 Campinas, São Paulo, Brazil; [b]Instituto de Física, Universidade do Estado do Rio de Janeiro, UERJ, 20550-013 Maracanã, Rio de Janeiro, RJ, Brazil;

*Corresponding author. Fax: 0055 19 788 5427; E-mail: siems@ifi.unicamp.br

tamariz@ifi.unicamp.br, agtri@ifi.unicamp.br, and tri@uerj.br

Received: _____; *Accepted:* _____

Abstract

The weighted oscillator strengths (gf) and the lifetimes for Si IV presented in this work were carried out in a multiconfiguration Hartree-Fock relativistic (HFR) approach. In this calculation, the electrostatic parameters were optimized by a least-squares procedure, in order to improve the adjustment to experimental energy levels. This method produces gf-values that are in better agreement with intensity observations and lifetime values that are closer to the experimental ones. In this work we present all the experimentally known electric dipole Si IV spectral lines.

Subject heading: atomic data

1. INTRODUCTION

The ground state configuration of three times ionized silicon, Si IV, is $1s^2\ 2s^2\ 2p^6\ 3s$ with the term ^2S. Si IV belongs to the Na I isoelectronic sequence. The ionization potential for Si IV is 364093.1 cm^{-1}(45.142 eV).

The first observations of Si IV spectra were made by Millikan & Bowen [1], McLennan & Shaver [2], and Fowler [3], who studied in detail the spectra of silicon, including Si IV, in the region 1400 - 6700 Å . Edlén & Söderqvist [4] improved and extended the analysis of Si IV in the wavelength region 815 - 4328 Å. Shenstone [5] observed Si IV - lines in the vacuum region, but did not publish them. Values can be found in Toresson [6] and Kelly [7]. Toresson [6] studied Si IV in the region 400 - 10 000 Å and he gave all known levels of the Si IV spectrum (also published by Martin and Zalubas [8]). Beyer et al. [9] used the beam-foil technique and gave unclassified Si IV lines. Kelly [7] summarized all wavelengths published for the Si IV spectrum in the vacuum -ultraviolet range.

The purpose of this work is to present a review of all known electric dipole transitions of Si IV, their oscillator strengths calculated from fitted values of the energy parameters and the lifetimes, calculated by the same method, for all known experimental energy levels. Oscillator strength and lifetimes are important in the study of laboratory and solar spectra, as Si IV is an astrophysically important ion [10,11].

2. CALCULATION

The oscillator strength $f(\gamma\gamma')$ is a physical quantity related to line intensity I and transition probability $W(\gamma\gamma')$, as given by Sobelman [12]:

$$W(\gamma\gamma') = \frac{2\omega^2 e^2}{mc^3} |f(\gamma\gamma')| \tag{1}$$

with,

$$I \propto gW(\gamma\gamma') \propto g\,|f(\gamma\gamma')| = gf.$$

Here m = electron mass, e = electron charge, γ = initial quantum state, $\omega = (E(\gamma) - E(\gamma'))/\hbar$, $E(\gamma)$ = initial state energy, g = $(2J+1)$ is the number of degenerate quantum states with angular momentum J (in the formula for the initial state). Quantities with primes refer to the final state.

In the equation above, the weighted oscillator strength, gf, is given by Cowan [13]:

$$gf = \frac{8\pi^2 mca_0^2\sigma}{3h} S, \tag{2}$$

where $\sigma = |E(\gamma) - E(\gamma')|/hc$, h =Planck's constant, c=light velocity, a_0 = Bohr radius, and the electric dipole line strength **S** is defined by:

$$\mathbf{S} = \left| < \gamma J \left\| \mathbf{P^1} \right\| \gamma' J' > \right|^2. \tag{3}$$

This quantity is a measure of the total strength of the spectral line, including all possible transitions between m, m' different J_z eigenstates. The tensor operator $\mathbf{P^1}$ (first order) in the reduced matrix element is the classical dipole moment for the atom in units of $-ea_0$.

To obtain gf, **S** is calculated first, or its square root:

$$\mathbf{S}^{1/2}_{\gamma\gamma'} = < \gamma J \left\| \mathbf{P^1} \right\| \gamma' J' > . \tag{4}$$

In a multiconfiguration calculation we have to expand the wavefunction $|\,\gamma J >$ in terms of single configuration wavefunctions, $|\,\beta J >$, for both upper and lower levels:

$$| \gamma J >= \sum_{\beta} y^{\gamma}_{\beta J} \mid \beta J > . \tag{5}$$

Therefore, we can have the multiconfigurational expression for $S^{1/2}_{\gamma\gamma'}$:

$$\mathbf{S}^{1/2}_{\gamma\gamma'} = \sum_{\beta} \sum_{\beta'} y^{\gamma}_{\beta J} < \beta J \left\| \mathbf{P^1} \right\| \beta' J' > y^{\gamma'}_{\beta' J'}. \tag{6}$$

The probability per unit time of an atom in a specific state γJ to make a spontaneous transition to any state with lower energy is

$$P(\gamma J) = \sum A(\gamma J, \gamma' J'), \tag{7}$$

where: $A(\gamma J, \gamma' J')$ is the Einstein spontaneous emission transition probability rate for a transition from the γJ to the $\gamma' J'$ state. The sum is over all $\gamma' J'$ states with $E(\gamma' J') < E(\gamma J)$.

The Einstein probability rate is related to gf through the following relation given by Cowan [13]:

$$gA = \frac{8\pi^2 e^2 \sigma^2}{mc} gf. \tag{8}$$

Since the natural lifetime $\tau(\gamma J)$ is the inverse of the probability $P(\gamma J)$, then:

$$\tau(\gamma J) = \left(\sum A(\gamma J, \gamma' J') \right)^{-1}. \tag{9}$$

Natural lifetime is applicable to an isolated atom. Interaction with matter or radiation will reduce the lifetime of a state.

The values for gf and lifetime given in Tables 1 and 2 respectively were calculated according to these equations.

In order to obtain better values for oscillator strengths, we calculated the reduced matrix elements $\mathbf{P^1}$ by using optimized values of energy parameters which were adjusted from a least-squares calculation. In this adjustment, the code tries to fit experimental energy values

by varying the electrostatic parameters. This procedure improves σ values used in eq. (2) and $y^{\gamma}_{\beta J}$ and $y^{\gamma'}_{\beta J'}$ values used in eq. (6). The energy parameters of this calculation are given by Siems [14].

3. DISCUSSION

The theoretical predictions for the energy levels of the configurations were obtained by diagonalizing the energy matrices with appropriate Hartree-Fock relativistic (HFR) values for the energy parameters. For this purpose the computer code developed by Cowan [13] was used. The program allowed us to calculate energy levels, wavelength, lifetimes and transition probabilities. For the even-parity configurations we have the following picture: $2p^6$ (3s+4s+5s+6s+7s+8s), $2p^6$ (3d+4d+5d+6d+7d), $2p^6$ (5g+6g+7g+8g) and $2p^6$ 7i. For the odd-parity case we study the $2p^6$(3p+4p+5p+6p+7p+8p), $2p^6$ (4f+5f+6f+7f+8f), $2p^6$ (6h+7h) configurations. The interpretation of the configuration level structures was made by a least- squares fit of the observed levels. More details of the calculations and the tables with the theoretical Hartree-Fock parameters and their fitting values can be found in Siems [14]. The energy level values were determined from the observed wavelengths by an interactive optimization procedure using the program ELCALC , Radziemski and Kaufman [15], in which the individual wavelengths are weighted according to their uncertainties. The energy levels adjusted by this method were used to optimize the electrostatic parameters by a least-squares procedure, and finally these optimized parameters were used again to calculate the *gf*- and lifetime values. This method produces *gf*-values that are in better agreement with line intensity observations and lifetime values that are closer to the experimental ones. Our semiempirical calculations for lifetimes are in good agreement with beam-foil measurements from Bashkin et al. [16] with following results: 4d ^{2}D($\tau = 2.0 \pm 0.2$ ns), 5p ^{2}P^0($\tau = 2.1 \pm 0.3$ ns), 5g ^{2}G($\tau = 1.2 \pm 0.2$ ns).

We have thus presented oscillator strengths and lifetimes for all known electric dipole

transitions in Si IV. The present work is part of an ongoing program, whose goal is to obtain weighted oscillator strength and lifetimes for elements of astrophysical importance. The works for Si III, Si V, Si VI, Si VII, Si IX and Si X have been concluded, Callegari and Trigueiros [17], Trigueiros and Jupén [18], Coutinho and Trigueiros [19], Coutinho and Trigueiros [20], Orloski, Cavalcanti, and Trigueiros [21], and Cavalcanti, Luna, and Trigueiros [22]. In this particular work on Si IV, the results are part of Siems' Ph.D. thesis that is in preparation [14].

This work was financially supported by the Fundação de Amparo à Pesquisa do Estado de São Paulo (FAPESP), Brazil, and by Conselho Nacional de Desenvolvimento Científico e Tecnológico (CNPq), Brazil. Computations were carried out at the Prof. John David Rogers Computational Center, UNICAMP.

REFERENCES

1. Millikan RA and Bowen IS. Phys Rev. Extreme ultra-violet spectra. 1924;23:1-34.

2. McLennan JC and Shaver WW Trans Roy Soc Canada.1924;18:14.

3. Fowler A. I. Bakerian Lecture.- The spectrum of Silicon at Successive Stages of Ionization Phil Trans Roy Soc 1925;225:1-39.

4. Edlén B and Söderqvist J. Neue Berechnung des Termsystems von Si IV. Z Phys 1933;87:217-218.

5. Shenstone AG. Unpublished Data.1958.

6. Toresson YG. Spectrum and term system of trebly ionized silicon. Ark Fys 1959;17:179-193.

7. Kelly RL. J Phys Chem Ref Data, 1987;16:275-276.

8. Martin WC. and Zalubas R. Energy levels of silicon, Si I through Si XIV. J Phys Chem Ref Data 1983;12:323-380.

9. Beyer LM, Maddox WE, Bridwell LB, Duncan DD, Bingham LL, Asbell JC. The beam-gas spectra of silicon, sulfur and oxygen. Nucl Instr Meth 1973;110:61-67.

10. Kempner JC, Richards MT. Analysis of the Si IV ultraviolet spectra of U Sagittae. Astrophys J 1999;512:345-350.

11. Ahmed S, Pinfield DJ, Mathioudakis M, Keenan FP, Phillips KJH, Curdt W. Electron temperature diagnostics for the quiet Sun using Si IV lines. Astron and Astroph 1999;346:L69-L72.

12. Sobelman I. Atomic spectra and radiative transitions. Berlin:Springer,1979.

13. Cowan RD. The theory of atomic structure and spectra. Berkeley: Univ California Press. 1981.

14. Siems A. Ph.D. thesis in preparation. Instituto de Física "Gleb Wataghin", Universidade Estadual de Campinas, UNICAMP, SP, Brazil. 1999.

15. Radziemski LJ. and Kaufman V. Wavelength, Energy levels, and analysis of neutral atomic chlorine (CL I). J Opt Soc Am, 1969;59:424-443.

16. Bashkin S, Astner G, Mannervik S, Ramanujam PS, Scofield M, Huldt S, Martinson I. Lifetimes for excited levels in Si I-Si IV. Phys Scr 1980;21:820-824.

17. Callegari F, Trigueiros AG. Weighted oscillator strength and lifetimes for the Si III spectrum. Astrophys J Suppl S 1998;119:181-188.

18. Trigueiros AG, Jupén C. Weighted oscillator strengths for Si V spectrum. J Quant Spectrosc Radiat Transfer, 1996;56:713-723.

19. Coutinho LH, Trigueiros AG. Weighted oscillator strength and lifetimes for the Si VI spectrum. Astrophys J Suppl S 1999;121:591-597.

20. Coutinho LH, Trigueiros AG. Weighted oscillator strength and lifetimes for the Si VII spectrum. Astrophys J Suppl S 1998;115:315-319.

21. Orloski RV, Trigueiros AG, Cavalcanti GH. Weighted oscillator strength and lifetimes for the Si IX spectrum. J Quant Spectrosc Ra 1999;61:665-669.

22. Cavalcanti GH, Luna FRT, Trigueiros AG. Weighted oscillator strength and lifetimes for the Si X spectrum. J Quant Spectrosc Ra 2000;64:5-13.

TABLE 1. WEIGHTED OSCILLATOR STRENGTHS AND SPECTRAL LINES FOR THE Si IV SPECTRUM

gf-VALUE[a]	INT.[b]	WAVELENGTHS (Å)[c]		LEVELS(cm^{-1})[d]			CONFIGURATIONS[c]			TERMS[c]	J-J[c]	REF.
		Observed	Calculated	Lower	-	Upper						
1.39×10^{-2}	1	361.560	361.560	0.000	-	276579.014	$2p^6 3s$	-	$2p^6 5p$	^2S-$^2P^0$	1/2-3/2	1
4.14×10^{-2}	4	457.818	457.815	0.000	-	218428.630	$2p^6 3s$	-	$2p^6 4p$	^2S-$^2P^0$	1/2-3/2	1,2,6
2.07×10^{-2}	3	458.155	458.155	0.000	-	218266.853	$2p^6 3s$	-	$2p^6 4p$	^2S-$^2P^0$	1/2-1/2	6
3.55×10^{-2}	2	515.118	515.118	71287.570	-	265417.932	$2p^6 3p$	-	$2p^6 5s$	$^2P^0$-^2S	1/2-1/2	6
7.08×10^{-2}	3	516.348	516.344	71748.603	-	265417.932	$2p^6 3p$	-	$2p^6 5s$	$^2P^0$-^2S	3/2-1/2	6
9.60×10^{-3}	0	559.533	559.533	71287.570	-	250008.111	$2p^6 3p$	-	$2p^6 4d$	$^2P^0$-^2D	1/2-3/2	5
1.73×10^{-2}	0	560.980	560.980	71748.603	-	250007.916	$2p^6 3p$	-	$2p^6 4d$	$^2P^0$-^2D	3/2-5/2	2,5
1.75×10^{-1}	2	595.840	595.856	160374.490	-	328200.230	$2p^6 3d$	-	$2p^6 7f$	^2D-$^2F^0$	5/2-7/2	9
3.55×10^{-1}	2	645.759	645.762	160374.490	-	315230.273	$2p^6 3d$	-	$2p^6 6f$	^2D-$^2F^0$	5/2-7/2	2,6
2.27×10^{-2}	0	688.194	688.195	160374.490	-	305682.158	$2p^6 3d$	-	$2p^6 6p$	^2D-$^2P^0$	5/2-3/2	5
9.60×10^{-1}	5	749.941	749.937	160374.490	-	293719.043	$2p^6 3d$	-	$2p^6 5f$	^2D-$^2F^0$	5/2-7/2	2,6
9.30×10^{-3}	1	779.040	779.065	193978.828	-	322337.813	$2p^6 4s$	-	$2p^6 7p$	^2S-$^2P^0$	1/2-3/2	2,9
2.28×10^{-1}	7	815.049	815.054	71287.570	-	193978.828	$2p^6 3p$	-	$2p^6 4s$	$^2P^0$-^2S	1/2-1/2	1,2,4,5,6
4.54×10^{-1}	8	818.129	818.128	71748.603	-	193978.828	$2p^6 3p$	-	$2p^6 4s$	$^2P^0$-^2S	3/2-1/2	1,2,4,5,6
7.17×10^{-2}	0	860.551	860.552	160374.490	-	276579.014	$2p^6 3d$	-	$2p^6 5p$	^2D-$^2P^0$	5/2-3/2	5
3.98×10^{-2}	0	861.118	861.118	160375.556	-	276503.630	$2p^6 3d$	-	$2p^6 5p$	^2D-$^2P^0$	3/2-1/2	5
5.20×10^{0}	8	1066.629	1066.616	160374.490	-	254128.929	$2p^6 3d$	-	$2p^6 4f$	^2D-$^2F^0$	5/2-7/2	1,2,3,4,6
1.66×10^{0}	8	1122.486	1122.486	71287.570	-	160375.556	$2p^6 3p$	-	$2p^6 3d$	$^2P^0$-^2D	1/2-3/2	1,2,4,5,6
2.98×10^{0}	10	1128.340	1128.339	71748.603	-	160374.490	$2p^6 3p$	-	$2p^6 3d$	$^2P^0$-^2D	3/2-5/2	1,2,4,5,6
3.04×10^{-2}	3	1210.652	1210.651	193978.828	-	276579.014	$2p^6 4s$	-	$2p^6 5p$	^2S-$^2P^0$	1/2-3/2	2
6.14×10^{-2}	3	1228.349	1228.349	218266.853	-	299676.926	$2p^6 4p$	-	$2p^6 6s$	$^2P^0$-^2S	1/2-1/2	1,2
5.00×10^{-4}	2	1365.549	1365.549	218266.853	-	291497.498	$2p^6 4p$	-	$2p^6 5d$	$^2P^0$-^2D	1/2-3/2	2
9.00×10^{-4}	1	1368.571	1368.570	218428.630	-	291497.585	$2p^6 4p$	-	$2p^6 5d$	$^2P^0$-^2D	3/2-5/2	2
1.077×10^{0}	15	1393.755	1393.755	0.000	-	71748.603	$2p^6 3s$	-	$2p^6 3p$	^2S-$^2P^0$	1/2-3/2	1,2,3,4,5,6
5.35×10^{-1}	12	1402.769	1402.769	0.000	-	71287.570	$2p^6 3s$	-	$2p^6 3p$	^2S-$^2P^0$	1/2-1/2	1,2,3,4,5,6
1.44×10^{0}	1	1634.607	1634.615	254128.929	-	315305.414	$2p^6 4f$	-	$2p^6 6g$	$^2F^0$-^2G	7/2-9/2	6
8.39×10^{-1}	6	1722.534	1722.530	160374.490	-	218428.630	$2p^6 3d$	-	$2p^6 4p$	^2D-$^2P^0$	5/2-3/2	1,2,3,4,5,6
4.65×10^{-1}	5	1727.377	1727.375	160375.556	-	218266.853	$2p^6 3d$	-	$2p^6 4p$	^2D-$^2P^0$	3/2-1/2	1,2,3,4,5,6
1.55×10^{-1}	1	1796.162	1796.163	250007.916	-	305682.158	$2p^6 4d$	-	$2p^6 6p$	^2D-$^2P^0$	5/2-3/2	3,4
8.61×10^{-2}	0	1797.496	1797.497	250008.111	-	305641.034	$2p^6 4d$	-	$2p^6 6p$	^2D-$^2P^0$	3/2-1/2	3,4
4.12×10^{-1}	3	2130.179	2130.172	218266.853	-	265417.932	$2p^6 4p$	-	$2p^6 5s$	$^2P^0$-^2S	1/2-1/2	3,4,6
8.21×10^{-1}	4	2127.467	2127.471	218428.630	-	265417.932	$2p^6 4p$	-	$2p^6 5s$	$^2P^0$-^2S	3/2-1/2	3,4,6
4.05×10^{0}	5 h	2287.041	2287.042	250007.916	-	293719.043	$2p^6 4d$	-	$2p^6 5f$	^2D-$^2F^0$	5/2-7/2	3,4,6
6.65×10^{-1}	2 H	2328.560	2328.569	293719.043	-	336650.686	$2p^6 5f$	-	$2p^6 8g$	$^2F^0$-^2G	7/2-9/2	6
8.69×10^{-2}	2	2366.755	2366.752	276503.630	-	318742.707	$2p^6 5p$	-	$2p^6 7s$	$^2P^0$-^2S	1/2-1/2	6
1.74×10^{-1}	3	2370.985	2370.983	276579.014	-	318742.707	$2p^6 5p$	-	$2p^6 7s$	$^2P^0$-^2S	3/2-1/2	4,6
2.43×10^{-2}	2	2482.816	2482.845	265417.932	-	305682.158	$2p^6 5s$	-	$2p^6 6p$	^2S-$^2P^0$	1/2-3/2	4,6
1.21×10^{-2}	1	2485.378	2485.384	265417.932	-	305641.034	$2p^6 5s$	-	$2p^6 6p$	^2S-$^2P^0$	1/2-1/2	6
7.94×10^{-2}	7	2517.506	2517.507	254127.103	-	293837.003	$2p^6 4f$	-	$2p^6 5g$	$^2F^0$-^2G	5/2-7/2	3,4,6
10.29×10^{0}	5	2517.560	2517.556	254128.929	-	293838.017	$2p^6 4f$	-	$2p^6 5g$	$^2F^0$-^2G	7/2-9/2	3,4
9.30×10^{-3}	1	2672.193	2672.192	276503.630	-	313914.955	$2p^6 5p$	-	$2p^6 6d$	$^2P^0$-^2D	1/2-3/2	6
8.00×10^{-3}	4	2675.120	2675.113	254127.103	-	291497.585	$2p^6 4f$	-	$2p^6 5d$	$^2F^0$-^2D	5/2-5/2	4,6
1.60×10^{-1}	4	2675.249	2675.243	254128.929	-	291497.585	$2p^6 4f$	-	$2p^6 5d$	$^2F^0$-^2D	7/2-5/2	4,6
1.66×10^{-2}	1 bl band	2677.570	2677.580	276579.014	-	313915.078	$2p^6 5p$	-	$2p^6 6d$	$^2P^0$-^2D	3/2-5/2	4,6
9.90×10^{-1}	3 h	2723.812	2723.794	291497.585	-	328200.230	$2p^6 5d$	-	$2p^6 7f$	^2D-$^2F^0$	5/2-7/2	3,4,6
1.78×10^{0}	3 h l	2895.131	2895.131	293719.043	-	328249.647	$2p^6 5f$	-	$2p^6 7g$	$^2F^0$-^2G	7/2-9/2	3,4,6
1.99×10^{0}	2 h	2904.470	2904.500	293838.017	-	328257.274	$2p^6 5g$	-	$2p^6 7h$	^2G-$^2H^0$	9/2-11/2	4,6
7.06×10^{-2}	1 h	2971.522	2971.524	293719.043	-	327361.974	$2p^6 5f$	-	$2p^6 7d$	$^2F^0$-^2D	7/2-5/2	6
2.42×10^{0}	7	3149.561	3149.562	218266.853	-	250008.111	$2p^6 4p$	-	$2p^6 4d$	$^2P^0$-^2D	1/2-3/2	3,4,6
4.34×10^{0}	9	3165.710	3165.715	218428.630	-	250007.916	$2p^6 4p$	-	$2p^6 4d$	$^2P^0$-^2D	3/2-5/2	3,4,6

TABLE 1 – Continued

gf-VALUE[a]	INT.[b]	WAVELENGTHS(Å)[c]		LEVELS(cm^{-1})[d]			CONFIGURATIONS[e]			TERMS[e]	J-J[e]	REF.
		Observed	Calculated	Lower		Upper						
2.65×10^{-2}	m Si III	3241.572	3241.574	291497.498	-	322337.813	$2p^6 5d$	-	$2p^6 7p$	$^2D.^2P^o$	3/2-3/2	6
2.39×10^{-1}	m Si III	3241.583	3241.584	291479.585	-	322337.813	$2p^6 5d$	-	$2p^6 7p$	$^2D.^2P^o$	5/2-3/2	6
1.33×10^{-1}	1 h	3244.192	3244.194	291497.498	-	322312.909	$2p^6 5d$	-	$2p^6 7p$	$^2D.^2P^o$	3/2-1/2	6
1.75×10^{0}	8	3762.435	3762.421	250007.916	-	276579.014	$2p^6 4d$	-	$2p^6 5p$	$^2D.^2P^o$	5/2-3/2	3,4,6
9.70×10^{-1}	6	3773.151	3773.152	250008.111	-	276503.630	$2p^6 4d$	-	$2p^6 5p$	$^2D.^2P^o$	3/2-1/2	3,4,6
1.12×10^{-1}	1 h bl band	4031.390	4031.368	305641.034	-	330439.513	$2p^6 6p$	-	$2p^6 8s$	$^2P^o.^2S$	1/2-1/2	6
2.24×10^{-1}	2	4038.057	4038.064	305682.158	-	330439.513	$2p^6 6p$	-	$2p^6 8s$	$^2P^o.^2S$	3/2-1/2	6
1.57×10^{0}	10	4088.854	4088.859	193978.828	-	218428.630	$2p^6 4s$	-	$2p^6 4p$	$^2S.^2P^o$	1/2-3/2	3,4,6
7.82×10^{-1}	9	4116.097	4116.093	193978.828	-	218266.353	$2p^6 4s$	-	$2p^6 4p$	$^2S.^2P^o$	1/2-1/2	3,4,6
3.54×10^{0}	7 h l	4212.407	4212.411	291497.585	-	315230.273	$2p^6 5d$	-	$2p^6 6f$	$^2D.^2F^o$	5/2-7/2	3,4,6
5.94×10^{-1}	3	4314.104	4314.095	276503.630	-	299676.926	$2p^6 5p$	-	$2p^6 6s$	$^2P^o.^2S$	1/2-1/2	4,6
1.18×10^{0}	5	4328.175	4328.174	276579.014	-	299676.926	$2p^6 5p$	-	$2p^6 6s$	$^2P^o.^2S$	3/2-1/2	4,6
9.65×10^{-1}	2 h l	4403.734	4403.728	313915.078	-	336616.706	$2p^6 6d$	-	$2p^6 8f$	$^2D.^2F^o$	5/2-7/2	6
2.05×10^{-2}	0 h	4411.652	4411.658	299676.926	-	322337.813	$2p^6 6s$	-	$2p^6 7p$	$^2S.^2P^o$	1/2-3/2	6
1.02×10^{-2}	m OII	4416.506	4416.507	299676.926	-	322312.909	$2p^6 6s$	-	$2p^6 7p$	$^2S.^2P^o$	1/2-1/2	6
2.27×10^{-2}	m OII	4602.578	4602.577	305641.034	-	327361.904	$2p^6 6p$	-	$2p^6 7d$	$^2P^o.^2D$	1/2-3/2	6
4.08×10^{-2}	0 h	4611.270	4611.294	305682.158	-	327361.974	$2p^6 6p$	-	$2p^6 7d$	$^2P^o.^2D$	3/2-5/2	6
8.95×10^{0}	9 h l	4631.241	4631.255	293719.043	-	315305.414	$2p^6 5f$	-	$2p^6 6g$	$^2F^o.^2G$	7/2-9/2	3,4,6
1.64×10^{1}	10 h s	4654.323	4654.332	293838.017	-	315317.385	$2p^6 5g$	-	$2p^6 6h$	$^2G.^2H^o$	9/2-11/2	3,4,6
1.89×10^{0}	1 H	4667.140	4667.139	315230.273	-	336650.686	$2p^6 6f$	-	$2p^6 8g$	$^2F^o.^2G$	7/2-9/2	6
8.53×10^{-2}	2 h	4673.297	4673.282	293838.017	-	315230.273	$2p^6 5g$	-	$2p^6 6f$	$^2G.^2F^o$	9/2-7/2	6
4.00×10^{-1}	3	4950.105	4950.086	293719.043	-	313915.078	$2p^6 5f$	-	$2p^6 6d$	$^2F^o.^2D$	7/2-5/2	6
3.21×10^{-1}	2 h	5304.971	5304.962	313915.078	-	332760.079	$2p^6 6d$	-	$2p^6 8p$	$^2D.^2P^o$	5/2-3/2	6
1.78×10^{-1}	1 h	5309.493	5309.497	313914.955	-	332743.906	$2p^6 6d$	-	$2p^6 8p$	$^2D.^2P^o$	3/2-1/2	6
3.08×10^{0}	5	6667.556	6667.549	276503.630	-	291497.498	$2p^6 5p$	-	$2p^6 5d$	$^2P^o.^2D$	1/2-3/2	6
5.51×10^{0}	7	6701.207	6701.194	276579.014	-	291497.585	$2p^6 5p$	-	$2p^6 5d$	$^2P^o.^2D$	3/2-5/2	6
3.30×10^{0}	3 h	6998.358	6998.343	313915.078	-	328200.230	$2p^6 6d$	-	$2p^6 7f$	$^2D.^2F^o$	5/2-7/2	6
2.66×10^{0}	6 h	7047.939	7047.974	291497.585	-	305682.158	$2p^6 5d$	-	$2p^6 6p$	$^2D.^2P^o$	5/2-3/2	6
1.48×10^{0}	4 h	7068.410	7068.421	291497.498	-	305641.034	$2p^6 5d$	-	$2p^6 6p$	$^2D.^2P^o$	3/2-1/2	6
7.74×10^{-1}	2 h	7630.497	7630.504	305641.034	-	318742.707	$2p^6 6p$	-	$2p^6 7s$	$^2P^o.^2S$	1/2-1/2	6
1.54×10^{0}	4 h	7654.555	7654.531	305682.158	-	318742.707	$2p^6 6p$	-	$2p^6 7s$	$^2P^o.^2S$	3/2-1/2	6
8.31×10^{0}	4 h l	7678.748	7678.747	315230.273	-	328249.647	$2p^6 6f$	-	$2p^6 7g$	$^2F^o.^2G$	7/2-9/2	6
1.46×10^{1}	5 h l	7718.785	7718.765	315305.414	-	328257.274	$2p^6 6g$	-	$2p^6 7h$	$^2G.^2H^o$	9/2-11/2	6
2.38×10^{1}	6 h s	7723.818	7723.816	315317.385	-	328260.786	$2p^6 6h$	-	$2p^6 7i$	$^2H^o.^2I$	11/2-13/2	6
7.34×10^{-2}	1 h	7730.469	7730.460	315317.385	-	328249.647	$2p^6 6h$	-	$2p^6 7g$	$^2H^o.^2G$	11/2-9/2	6
2.25×10^{-1}	1 h	7752.905	7752.922	315305.414	-	328200.230	$2p^6 6g$	-	$2p^6 7f$	$^2G.^2F^o$	9/2-7/2	6
6.85×10^{-1}	1 h	8240.606	8240.611	315230.273	-	327361.974	$2p^6 6f$	-	$2p^6 7d$	$^2F^o.^2D$	7/2-5/2	6
2.05×10^{0}	2 h	8957.245	8957.262	265417.932	-	276579.014	$2p^6 5s$	-	$2p^6 5p$	$^2S.^2P^o$	1/2-3/2	6
1.02×10^{0}	1 h	9018.162	9018.165	265417.932	-	276503.630	$2p^6 5s$	-	$2p^6 5p$	$^2S.^2P^o$	1/2-1/2	6

[a]Weighted oscillator strengths for atomic transition obtained by the method described in § 2.

[b]Observed line intensities and shapes (bl = blended by, h = hazy, H = very hazy, l = shaded to longer waves, m = masked by, s = shaded to shorter waves).

[c]Wavelength corresponding to the energy levels difference between the experimental adjusted energy level values. Above 2000

Å wavelengths are given in air.

[d] Numerical values of the energy levels are those obtained by an optimized procedure using the program ELCALC.

[c] Level designations for the transition, including configuration parentage, term, and total angular momentum. For pratical purposes, we show them in three separate columns.

TABLE 2. LIFETIMES FOR THE Si IV SPECTRUM

Configuration	Terms	Energy(cm^{-1})	Lifetimes (ns)[a]	Configuration	Terms	Energy(cm^{-1})	Lifetimes (ns)[a]
$2p^6 3s$	$^2S_{1/2}$	0.000	0.000	$2p^6 8g$	$^2G_{9/2}$	336650.686	3.619
$2p^6 3d$	$^2D_{5/2}$	160374.490	0.384	$2p^6 3p$	$^2P_{1/2}$	71287.570	1.102
$2p^6 3d$	$^2D_{3/2}$	160375.556	0.379	$2p^6 3p$	$^2P_{3/2}$	71748.603	1.081
$2p^6 4s$	$^2S_{1/2}$	193978.828	0.293	$2p^6 4p$	$^2P_{1/2}$	218266.853	1.923
$2p^6 4d$	$^2D_{5/2}$	250007.916	1.846	$2p^6 4p$	$^2P_{3/2}$	218428.630	1.908
$2p^6 4d$	$^2D_{3/2}$	250008.111	1.824	$2p^6 4f$	$^2F_{5/2}$	254127.103	0.262
$2p^6 5s$	$^2S_{1/2}$	265417.932	0.751	$2p^6 4f$	$^2F_{7/2}$	254128.929	0.262
$2p^6 5d$	$^2D_{3/2}$	291497.498	3.231	$2p^6 5p$	$^2P_{3/2}$	276579.014	2.449
$2p^6 5d$	$^2D_{5/2}$	291497.585	3.256	$2p^6 5p$	$^2P_{1/2}$	276503.630	2.462
$2p^6 5g$	$^2G_{7/2}$	293837.003	0.924	$2p^6 5f$	$^2F_{7/2}$	293719.043	0.483
$2p^6 5g$	$^2G_{9/2}$	293838.017	0.924	$2p^6 6p$	$^2P_{3/2}$	305682.158	3.608
$2p^6 6s$	$^2S_{1/2}$	299676.926	1.485	$2p^6 6p$	$^2P_{1/2}$	305641.034	3.620
$2p^6 6d$	$^2D_{3/2}$	313914.955	4.686	$2p^6 6f$	$^2F_{7/2}$	315230.273	0.807
$2p^6 6d$	$^2D_{5/2}$	313915.078	4.711	$2p^6 6h$	$^2H_{11/2}$	315317.385	2.376
$2p^6 6g$	$^2G_{9/2}$	315305.414	1.569	$2p^6 7p$	$^2P_{1/2}$	322312.909	5.314
$2p^6 7s$	$^2S_{1/2}$	318742.707	2.567	$2p^6 7p$	$^2P_{3/2}$	322337.813	5.301
$2p^6 7d$	$^2D_{3/2}$	327361.904	6.159	$2p^6 7f$	$^2F_{7/2}$	328200.230	1.253
$2p^6 7d$	$^2D_{5/2}$	327361.974	6.188	$2p^6 7h$	$^2H_{11/2}$	328257.274	3.750
$2p^6 7g$	$^2G_{9/2}$	328249.647	2.454	$2p^6 8p$	$^2P_{1/2}$	332743.906	0.167
$2p^6 7i$	$^2I_{13/2}$	328260.786	5.267	$2p^6 8p$	$^2P_{3/2}$	332760.079	0.167
$2p^6 8s$	$^2S_{1/2}$	330439.513	1.059	$2p^6 8f$	$^2F_{7/2}$	336616.706	1.841

[a] Lifetimes for the energy level obtained by the method describes in § 2.

EUV Photon Emission Spectroscopy For Diagnostics Of Single And Multiple-Electron Capture Processes In 80 keVAr^{8+} + N_2 Collisions.

A. Siems[$,#], H. Merabet[#*], R. Bruch[#], V. Golovkina[#], G. Hinojosa[#], R. Phaneuf[#], J. Hanni[#], S. Bliman[&], and A.G. Trigueiros[$]

[#] *Department of Physics, University of Nevada, Reno, NV 89557 USA*
[$] *Instituto de Fisica, Universidade Estadual de Campinas, 13083-970 Campinas, Sao Paulo, Brazil*
[&] *Department de Physique, Universitéde Marne la Vallé, 93166 Noisy LeGrand, France*

Abstract. We present the first EUV emission spectra following single and multiple-electron capture for the 80 keV Ar^{8+} + N_2 multi charged ion-molecular collision system. Our analysis provides evidence of single and double capture processes leading to radiative deexcitation of Ar^{7+}* (nl) n=3-6 and Ar^{6+}* (3lnl') n=3-5 projectile states. Furthermore we have identified numerous N^{q+} (q=2,3) ionic target lines in the EUV spectral range (10-80 nm), owing to multiple ionization of the N_2 molecule and consecutive dissociation plus excitation of the fragments. The subsequent photon emission arises from high lying states of the target such as N^{2+}* ($1s^2$2s2lnl') ^{2,4}L, n=2-10 and N^{3+}* ($1s^2$2lnl') ^{1,3}L,n=2-5 with excitation energies up to 52 eV and 78 eV, respectively. The N^{2+} and N^{3+} excited dissociated fragments are due to multiply electron capture processes involving up to six electrons.

INTRODUCTION

EUV photon emission spectrometry of one- and two-electron processes in fast ion-atom and electron-atom collisions with few electron targets such as helium has attracted considerable interest over the past decade [1,2]. Recently, slow collisions involving highly charged ions have been studied including the Ar^{8+}+He system [3-5]. Furthermore spectroscopic investigations of ion-molecule systems such as Ar^{8+}+H_2 and Ar^{8+}+N_2 have been performed to elucidate multiple electron charge transfer, molecular dissociation, and excitation dynamics [6-9].

In this work we present new data obtained from Ar^{8+}+N_2 single collisions utilizing EUV spectroscopy. This collision system is of particular interest due to the many electron molecular target, which allows us to study multiple electron capture reactions and subsequent fragmentation and excitation of highly charged N_2^{q+} molecular complexes. These highly charged N_2^{q+} molecular target ions are unstable and rapidly dissociate via Coulomb explosion processes leading to highly excited ionic nitrogen states. EUV photoemission spectroscopy is the ideal tool for selectively analyzing these excited ionic N^{q+} states. These states provide detailed collisional information about new dissociation channels following multiple electron capture processes with many electron molecular targets. In a recent publication Bliman *et al.* [9] has addressed the importance of Non-Frank-Condon dissociation mechanisms caused by large space and time dependent electric field effects which may lead to large intermolecular interactions.

EXPERIMENTAL SETUP

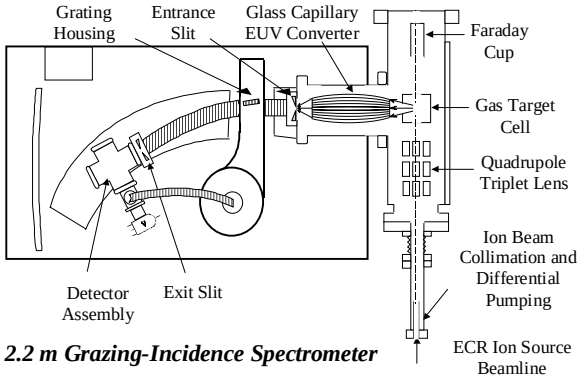

FIGURE 1. Experimental set-up for EUV spectroscopy of highly charged ion-molecule collisions.

In order to obtain a deeper understanding of the many-electron correlation effects and molecular fragmentation in Ar^{8+} + N_2 collisions, we have measured EUV spectra over a large wavelength range from 10 to 80 nm at a projectile energy of 80 keV (v = 0.29 a.u.). The experiments have been performed at the University of Nevada, Reno, 14-Ghz Electron Cyclotron Resonance (ECR) multi-charged ion source facility.

* Corresponding author: H. Merabet, email: hocine@physics.unr.edu

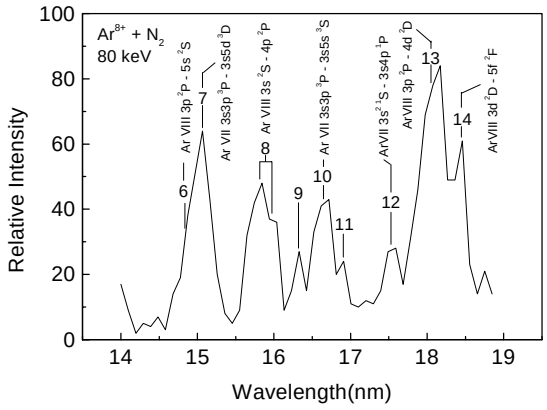

FIGURE 2. EUV Spectrum for $Ar^{8+}+N_2$ collisions in the wavelength range from about 14-19 nm. The dominant spectral features arise from single and double electron capture processes.

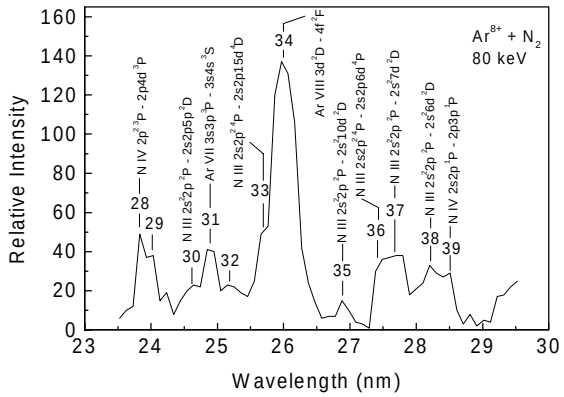

FIGURE 3. EUV Spectrum for $Ar^{8+}+N_2$ collisions in the wavelength range from about 23-29 nm. The dominant spectral features arise from ionic projectile and target lines.

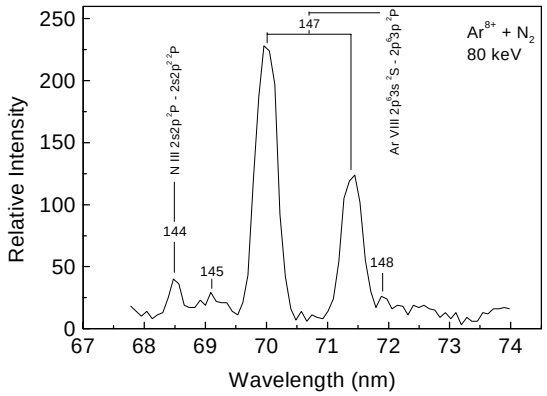

FIGURE 4. EUV Spectrum for 80 keV $Ar^{8+}+N_2$ collisions in the wavelength range from about 68-74 nm. The dominant spectral features arise from ionized projectile and target lines.

As can be seen in Fig. 1, the experimental apparatus is composed of a 2.2. m grazing incidence monochromator (Mc Pherson Model 247), a target chamber with a differentially pumped gas cell, collimator system, quadrupole lens for focusing and steering of the ion beam, and a Faraday cup for ion beam normalization. The target cell is operated at a pressure of about 0.7 mTorr and the background pressure of the vacuum chamber is approximately 5 x 10^{-7} Torr. The gas pressure in the target cell is controlled via a capitance manometer (Barocel 655). The emitted photons are observed under an angle of 90^0 with respect to the incident ion-beam direction and the measured line intensities have been substantially enhanced through the use of a sophisticated Glass Capillary Converter (GCC) system [10-11]. This GCC device collects, guides, and focuses the emitted radiation onto the entrance slit of the 2.2 m grazing incidence monochromator equipped with a 600 lines/mm grating. Data acquisition and control is accomplished using a PC-CAMAC computer system, and the photon counts are normalized with respect to the amount of charge collected in the Faraday cup. The slit width of the grazing incidence monochromator has been set to be 400 μm and the short wavelength radiation is detected by a channel electron multiplier (CEM). We have relatively calibrated our obtained spectra by dividing by the established efficiency curve for the monochromator [12]. Here we present an overview of the experimental results and identification of the most prominent target and projectile lines.

RESULTS AND DISCUSSION

In Fig. 2,3, and 4 we exhibit some of our measured characteristic EUV spectra following single Ar^{8+} + N_2 collisions. We have provided evidence for more than 150 spectral lines; many of them have been identified as projectile lines arising from Ar^{7+} and Ar^{6+} ions due to single and double electron capture processes. For the identification of the target and projectile line structures we also utilized the comprehensive EUV line tabulations of Kelly [13]. Especially, we have identified numerous ionic nitrogen lines originating from N^{2+}* and N^{3+}* states stabilizing by radiative decay. We also established correlation diagrams for Ar^{8+} + N single and double capture processes indicated in Fig. 5 and 6a and b, respectively. It is important to note that have we used a simplified collisional model replacing the N_2 potentials by the atomic nitrogen curves and assumed that the cross sections are approximately half the cross section for N_2 projectile states. Using this approach, we predicted that for single electron capture, the Ar^{7+}* (nl) states with n=3-5 are most abundantly populated. Furthermore we have performed extensive calculations of energy levels, transition wavelengths, and transition probabilities for Ar^{7+}*(nl), n=3-6 and Ar^{6+}*(nln'l'), n,n'=3-5 projectile states using the Cowan atomic structure code [14]. In addition we have utilized correlation diagrams for the

single and double capture processes based on the classical overbarrier model to receive more detailed information about the complex $Ar^{8+} + N_2$ system. It is evident from the identification of the observed line spectra, that the prominent single and double electron capture processes:

$$Ar^{8+} + N_2 \rightarrow Ar^{7+}* (nl, n=3\text{-}6) + N_2^{+} \qquad (1)$$

$$Ar^{8+} + N_2 \rightarrow Ar^{6+}* (3lnl, n=3\text{-}5) + N_2^{2+} \qquad (2)$$

are the main channels that stabilize via radiative transitions, whereas the higher lying doubly excited $Ar^{6+}*$ (nlnl') states are expected to decay predominantly via autoionization. These results will be discussed in detail elsewhere [15].

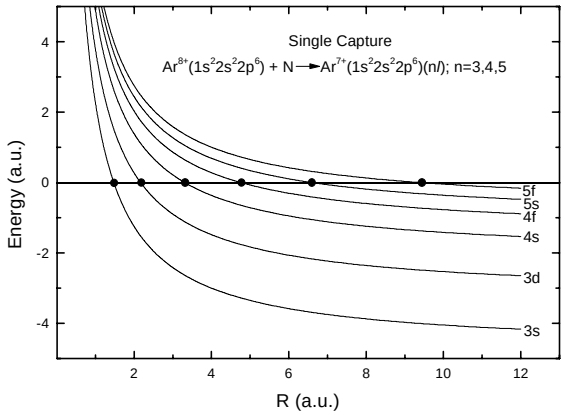

FIGURE 5. Correlation diagram for Ar^{8+} + N single electron capture processes using the classical over-barrier model.

In this work we have focused mainly on the fragmentation of multi-charged N_2^{q+}, q=1-6 molecular complexes and excitation of the consecutive dissociation fragments. In Table 1 we have summarized the main EUV transitions originating from $N^{2+}*$ and $N^{3+}*$ ions in the 10-80 nm range. According to Remscheid et al.[7] such nitrogen ions generated in slow $Ar^{8+} + N_2$ collisions are most likely produced by :

$$N_2^{q+} \rightarrow N^{r+} + N^{s+} \qquad (3),$$

where in the dissociation of N_2^{q+} the symmetric distribution of the charge to both fragments is preferred, i.e. that N^{2+}, N^{4+}, and N^{6+} fragments most likely have the same charge, whereas for odd charge states such as N^{3+} and N^{5+} they differ mainly by one charge unit. In our experiment we have observed the EUV- photon emission from such ionic nitrogen fragments, arising from the highly excited target states $N^{2+}*$ ($1s^2 2s 2lnl'$) $^{2,4}L$, n=2-10 and $N^{3+}*$ ($1s^2 2lnl'$) $^{1,3}L$, n=2-5 with excitation energies up to 52 and 78 eV, respectively (see Table 1). For example $N^{2+}*$ and $N^{3+}*$ excited nitrogen fragments may result from four and six electron capture mechanisms. The importance of non-Franck-Condon dissociation processes in such highly charged ion-molecule collisions has been suggested by Bliman et al [9]. In particular they have estimated that the electric space and time-field variation for $Ar^{8+} + H_2$ collision system is of the order of 1.5 x 10^{25} V/ms leading to dissociation processes deviating from the Frank-Condon Principle.

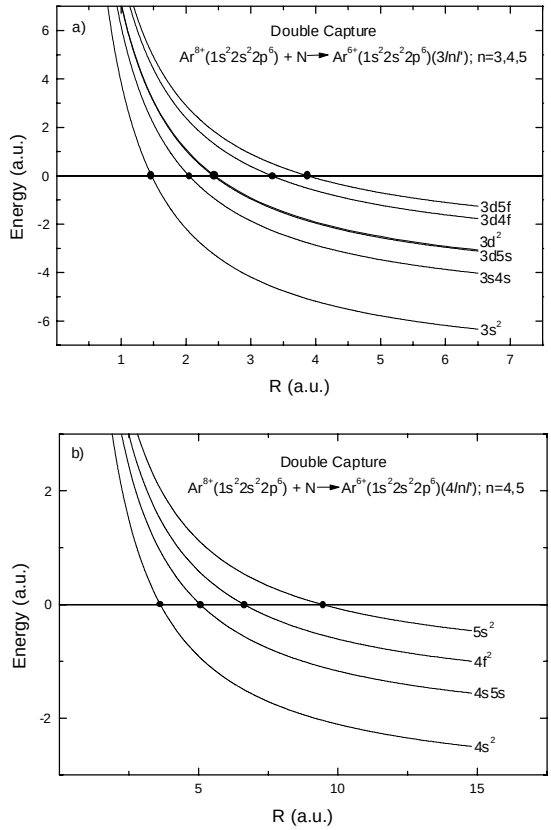

FIGURE 6a and b. Correlation diagrams for Ar^{8+} + N double electron capture processes using the classical over-barrier model.

When comparing the relative line intensities for $N^{2+}*$ and $N^{3+}*$ optical transitions, we have found that 60% of the identified target lines stem from $N^{2+}*$ excited states whereas 40% originate from $N^{3+}*$ emission lines in our wavelength region. From Table 1, it is obvious that the $N^{2+}*$ ($2s2p3d$, $2s^2 3d$, $2s2p4d$, $2s2p^2$) configurations are most abundantly populated in 3,4, and 5 electron capture processes. Furthermore, for the $N^{3+}*$ fragmentation channels, the configurations $N^{3+}*$ (2s2p, 2s4p, 2s4s, 2p4p, 2p5s, 2s4s) dominate in the measured spectral range.

CONCLUSIONS

We have studied single and multiple electron capture processes in slow 80 keV collisions between Ar^{8+} and molecular nitrogen using EUV spectrometry. Exotic electron capture processes with up to six electrons in one collision could explain the observed highly excited ionic nitrogen Rydberg states of the type N^{2+}* ($1s^2 2s 2lnl'$) $^{2,4}L$, n=2-10 and N^{3+}* ($1s^2 2lnl'$) $^{1,3}L$, n=2-5. Thus, capture of four electrons may lead to the production of N^{2+}* excited ions. If five electrons are captured, this may lead to the creation of N^{2+}* and N^{3+}* excited states. Whereas, in the six electron capture reaction, N^{3+}* excited ions are most likely created. These findings are consistent with our measured relative target line intensities. These measurements will be complimented in the near future by target ion TOF spectrometry.

ACKNOWLEDGMENTS

This Project has been partially supported by ACSPECT Corp., Reno, Nevada, and by CNPq (Conselho National de Desenvolvimento Cientifico e Technológico), Brazil.

TABLE 1: Observed main ionic target lines owing to fragmentation plus excitation following multiple electron capture processes in 80 keV Ar^{8+} + N_2 collisions.

Peak Position	Relative Intensity	Charge State	Optical Transition	Wavelength[a] λ (nm)	Wavelength[b] λ (nm)	Energy (eV)[c]
30	25	N^{2+}	$2s^2 2p\ ^2P_{3/2} - 2s2p5p\ ^2D_{5/2}$	24.63	24.6249	50.374
33	56	N^{2+}	$2s2p^2\ ^4P_{5/2} - 2s2p15d\ ^4D_{7/2}$	25.70	25.7502	55.260
35	17	N^{2+}	$2s^2 2p\ ^2P_{3/2} - 2s^2 10d\ ^2D_{5/2}$	26.89	26.8473	46.206
36	37	N^{2+}	$2s2p^2\ ^4P_{5/2} - 2s2p6d\ ^4P_{5/2}$	27.44	27.4374	52.299
37	46	N^{2+}	$2s^2 2p\ ^2P_{3/2} - 2s^2 7d\ ^2D_{5/2}$	27.70	27.6326	44.894
38	40	N^{2+}	$2s^2 2p\ ^2P_{3/2} - 2s^2 6d\ ^2D_{5/2}$	28.22	28.2209	43.959
42	26	N^{2+}	$2s^2 2p\ ^2P_{3/2} - 2s^2 5s\ ^2S_{1/2}$	29.98	29.9818	41.378
48	19	N^{2+}	$2s^2 2p\ ^2P_{3/2} - 2s^2 4d\ ^2D_{5/2}$	31.50	31.4850	39.402
53	16	N^{2+}	$2s^2 2p\ ^2P_{3/2} - 2s^2 4s\ ^2S_{1/2}$	33.20	33.2333	37.332
61	92	N^{2+}	$2s2p^2\ ^4P - 2s2p3d\ ^4P$	35.79	35.8578	41.688
62	112	N^{2+}	$2s2p^2\ ^2P_{3/2} - 2s2p3d\ ^2P_{3/2}$	36.06	36.1288	52.420
65	109	N^{2+}	$2s^2 2p\ ^2P_{3/2} - 2s^2 3d\ ^2D_{5/2}$	37.28	37.4441	33.136
68	77	N^{2+}	$2s2p^2\ ^2S_{1/2} - 2s2p4d\ ^2P_{3/2}$	39.35	38.7483	48.243
74	94	N^{2+}	$2s2p^2\ ^2P_{1/2} - 2s2p4d\ ^2P_{1/2}$	40.91	41.1056	48.252
144	200	N^{2+}	$2s^2 2p\ ^2P_{3/2} - 2s2p^2\ ^2P_{3/2}$	68.43	68.5816	18.101
154	116	N^{2+}	$2s2p^2\ ^4P_{5/2} - 2p^3\ ^4S_{3/2}$	77.14	77.2385	23.162
19	38	N^{3+}	$2s2p\ ^3P_2 - 2s5s\ ^3S_1$	21.04	20.9471	67.552
22	52	N^{3+}	$2s2p\ ^1P_1 - 2p4p\ ^1S_0$	21.73	21.7218	73.287
24	49	N^{3+}	$2p^2\ ^3P_2 - 2p5s\ ^3P_2$	22.22	22.1789	77.695
28	52	N^{3+}	$2s2p\ ^3P_2 - 2s4s\ ^3S_1$	23.80	23.7991	60.460
39	36	N^{3+}	$2s2p\ ^1P_1 - 2p3p\ ^1P_1$	28.53	28.5561	59.626
49	25	N^{3+}	$2p^2\ ^1S_0 - 2s5p\ ^1P_1$	31.87	31.7596	68.224
50	27	N^{3+}	$2s2p\ ^3P_2 - 2s3s\ ^3S_1$	32.26	32.2722	46.780
64	57	N^{3+}	$2p^2\ ^1S_0 - 2s4p\ ^1P_1$	36.78	36.8108	62.868
153	194	N^{3+}	$2s^2\ ^1S_0 - 2s2p\ ^1P_1$	76.54	76.5148	16.205

[a]This work. [b]Kelly data [13]. [c]Excitation energies are derived from data of Kelly [13].

REFERENCES

1. McGuire, J.H., *Electron Correlation Dynamics in Atomic Collisions, Cambridge University Press* (1997).
2. Fuelling, S., *et al. Phys. Rev. Lett.* **68** 3152 (1992).
3. Bliman, S., *et al., Phys. Rev A,* **46** 1321 (1992).
4. Zou, Y., *et al., Phys. Scr.* **T73** 79 (1997).
5. Kambara, T., *et al., J. Phys. B* **31** L909 (1998).
6. Meyer, F.W., *et al., Nucl. Instrum. Methods Phys. Res. B* **24/25** 106 (1987).
7. Remscheid, A., et al., J.Phys. B 29 515 (1996).
8. Shiromaru, H., *et al, Phys. Scr.* **T80** 110 (1999).
9. Bliman, S., *et al., Phys. Rev. A.*, **60** 1 (1999).
10. Bruch, R., *et al., Surf. Interface Anal.*, **27** 236 (1999).
11. Bruch, R., *et al., Rev. Sci. Instrum.*, **68** 1091 (1997).
12. Fülling, S., *Ph.D. Thesis*, UNR, Reno, NV USA (1991).
13. Kelly, R.L., *Atomic and Ionic Lines Below 2000 Å, H through Ar* (1982).
14. Cowan, R.D., *The Theory of Atomic Structure and Spectra*, Univ. of California Press (1981).
15. Siems, A., *Ph.D. Thesis*, State University of Campinas Brazil (2000).

Auger Decay of Triply Excited States of Li and Be^+ Projectiles Following Ion-Molecule Interactions.

R. Bruch[a], A. Siems[a,b], H. Merabet[a*], J. Hanni[a], S. Bliman[c]

[a]*Department of Physics, University of Nevada, Reno, NV 89557 USA*
[b]*Instituto de Fisica, Universidade Estadual de Campinas (Unicamp), 13083-970 Campinas, São Paulo, Brazil*
[c]*Department de Physique, Université de Marne la Vallée, 93166 Noisy LeGrand, France*

Abstract. In this study, we present high resolution electron spectra and new identifications of numerous triply excited states of the Li-isoelectronic sequence produced by intermediate velocity Li^+ and Be^+ projectiles interacting with CH_4 molecules under single collision conditions. In particular, we show here as typical examples high resolution lithium and beryllium projectile Auger electron spectra following double K-shell excitation in 200 keV $Li^+ + CH_4$ and 300 keV $Be^+ + CH_4$ collisions. For the beryllium case, the impact velocity is 1.15 a.u. Many new lines appearing in these spectra have been assigned to triply excited Li and Be^+ and doubly excited Li^+ and Be^{2+} states. Only recently due to the pioneering theoretical predictions by Chung and coworkers (1), such collisional line structures can now be unambiguously identified. We have not only identified the lowest lying, most prominent $2s^22p$, $2s2p^2$ and $2p^3$ triply excited states (2), but also new excitation and deexcitation channels of higher lying $2l2l'nl''$ hollow atom/ion Rydberg states following ion-molecule collisions.

INTRODUCTION

Triply excited states in Li and Be^+, also referred to as "hollow atoms," represent fundamental highly-correlated few-body dynamical systems (3-10). In earlier studies of foil excitation of Li, such states were observed by Auger-electron projectile spectroscopy, however the resolution was limited due to kinematic effects (4). Using projectile beam-gas excitation, higher resolution electron spectra from double K-shell vacancy states in Li and Be^+ were obtained (5-7). Furthermore, Simons *et al.* (8) were the first to calculate the Auger and radiative decay rates of the $2s^22p$ level in Li using many-body perturbation theory. The first comprehensive description of hollow atoms in Li and Be^+ was presented by Rødbro *et al.* (5-7). Auger decay channels of triply excited three-electron systems using beam-gas spectroscopy were reviewed by Bruch and Chung (5). Extensive calculations of even and odd parity triply excited Li-like states were provided by Chung *et al.* (1, 9-10,18), and Conneely and Lipsky (3). In addition, optical emission from the $(2p2p2p)\ ^4S^o$ states in three-electron systems has been studied both experimentally and theoretically for He^-, Li, Be^+, B^{2+}, and C^{3+} (11-12).

Recently, photoelectron and photoion spectrometry studies of the triply excited states of Li have been conducted using synchrotron radiation sources (13-17). The selectivity of such photo-excitation techniques populate only $^2P^o$ symmetry states from the ground state of Li $(1s^22s)\ ^2S$. States of different symmetry and parity have been examined by means of laser excited $(1s^22p)\ ^2P^o$ states from which synchrotron radiation has produced even-parity triply excited states (17). Photo-excitation by synchrotron radiation has proven to be a very successful method to study energies, widths, and branching ratios of such states in Li.

In this study, we provide a new examination of our double-hole K-shell vacancy Li^+, Li, Be^{2+} and Be^+ high-resolution electron spectra originating from Li^+ and Be^+ ion beams interacting with He and CH_4 under single-collision conditions. When compared to synchrotron radiation experiments, we have observed numerous additional new transitions arising from both doublet and quartet states of even and odd parity not previously discovered. Several of the triply excited Be^+ results presented here are the first reported in the literature. These results are compared with theoretical predictions of Li-like triply excited hollow atoms (9).

EXPERIMENTAL METHOD

The ejected electron spectra of highly excited resonance states of Li and Be were studied by using the projectile-electron spectroscopy method. High resolution was obtained by selecting a small observation angle with respect to the beam axis.

* Corresponding author: H. Merabet, email: hocine@physics.unr.edu

The apparatus used in this study consisted of a 600 keV heavy-ion accelerator, equipped with a universal ion source of the Nielsen type, and target chamber with a high resolution electron spectrometer, which can be continuously rotated between 0° and 150°. The excitation of the observed hollow atoms took place in a differentially pumped gas cell. Before entering the gas cell, the ion beam was carefully collimated using different apertures. The pressure in the differentially pumped gas cell was kept low enough (typically 10^{-3} torr) to ensure single-collision conditions. For normalization purposes, the ion beam was collected in a Faraday cup. The details of the experimental setup were described by Rødbro *et al.* (6-7). Since projectile electrons are ejected from fast moving particles, the laboratory energies E were transformed to energies E_o in the source-particle frame.

FORMATION OF TRIPLY EXCITED Li-LIKE STATES IN ION-ATOM AND ION-MOLECULE COLLISIONS

The projectile Auger electron spectra of Li and Be were studied for incident beam energies from 100 to 500 keV excited in single collisions with He and CH_4. Double-hole vacancy states were weakly excited in collisions with helium, whereas strong lines appeared when CH_4 was used as the target gas. Therefore, we primarily focused on molecular targets such as CH_4 to obtain high excitation probabilities for helium- and lithium-like doubly core-excited states (hollow atoms). The formation of triply excited doublet and quartet projectile states involves both direct excitation, electron capture, and or electron exchange mechanisms. For instance, Li $(2l2l'nl'')$ ^{2}L states may be formed by two-electron double K-shell excitation processes plus electron capture. On the other hand, Be^+ $(2l2l'nl'')$ ^{2,4}L states may be formed by double K-shell excitation plus additional outer shell excitation and/or electron exchange.

RESULTS AND DISCUSSION

Fig. 1, shows the high-energy portion of the Li electron spectrum obtained in 200 keV Li^+ + CH_4 collisions in the energy range from 66 to 93 eV. The observed spectral features (peaks 18-48) and the additional satellite lines (labeled *a-l*) are associated with doubly core-excited states and their decay in Li and Li^+. Several triply excited resonance channels are indicated in this figure and the line identification is summarized in Table I. In this table, we have identified resonance states and decay channels of eighteen lines originating from triply excited states. Especially, we have seen numerous decay channels of $(2l2l'nl'')$ ^{2}L resonances with n = 2, 3, and 4. It is

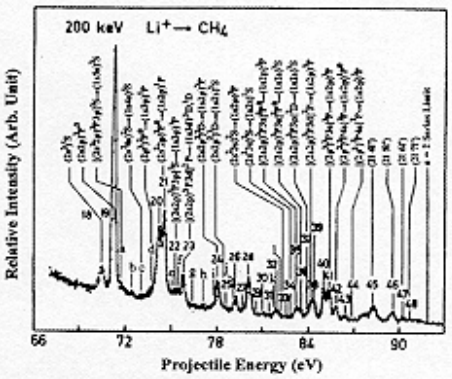

Figure 1. High-resolution projectile Auger electron spectrum for the 200 keV Li^+ + CH_4 collision system observed at an angle of 6.4°. The structures shown correspond to doubly core-excited Li^+ and triply excited Li states (hollow atoms).

interesting to note that both even and odd parity triply excited states contribute to the spectrum.

In Fig. 2, we have schematically shown the Auger decay path of Li-like triply excited states. As can be seen, some of the $(2l2l'nl'')$ states can not only decay to the lowest $(1s2l)$ ^{3,1}L continua, but also to higher lying continua such as $(1s3l)$ ^{3,1}L and $(1s4l)$ ^{3,1}L. The Auger

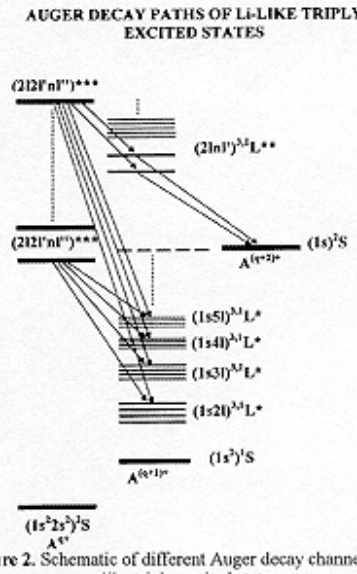

Figure 2. Schematic of different Auger decay channels of Li-like triply excited states.

rates of such triply excited series have been examined theoretically by Verbockhaven and Hansen (19); in particular, they have found that the Auger rates of triply excited Auger series behave rather differently when compared to doubly excited series. For example, the Auger decay rates for ($2l2l'nl''$) Rydberg series with $n \geq 2$ are expected to be nearly independent of n, while typical ($2lnl'$) decay rates decrease with increasing values of n. As demonstrated in Fig. 1, the Li^+ ($2lnl'$) doubly excited states for n = 4-7 agree with this predicted trend. Furthermore, all the observed transitions from triply excited resonances are in close agreement with the predictions of Chung and coworkers (1,9,10,18). In this work, we have also observed Auger transitions to Li^+ Rydberg states including (1s3p) $^1P^o$, (1s3d) $^{3,1}D$, (1s4s) ^3S, and (1s5s) ^3S. According to Fig. 2, the higher lying ($2lnl'nl''$) Rydberg states can also decay to doubly excited ($2lnl'$) $^{3,1}L$ manifolds, which in turn can decay further to the Li^{2+} (1s) ^2S ground state. Hence, some of the measured contributions of the doubly excited Li^+ ($2lnl'$) states (see Fig. 1) may arise from the decay of such triply excited states.

The high energy portion of the 300 keV $Be^+ + CH_4$ spectrum, in the projectile energy range from 120 to

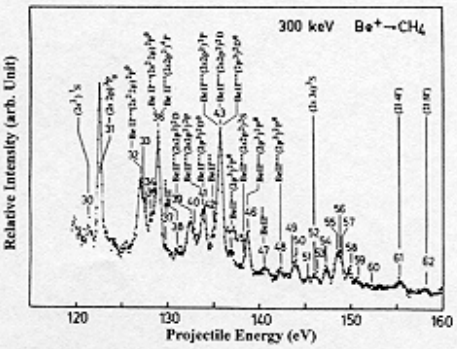

Figure 3. High-resolution projectile Auger electron spectrum for 300 keV $Be^+ + CH_4$ collisions observed at an angle of 6.4°. The structures shown correspond to doubly core-excited Be^{2+} and triply excited Be^+ states (hollow atoms).

160 eV is illustrated in Fig. 3. The observed spectral features (peaks 30-62) are attributed to Be^+ and Be^{2+} states with double K-shell vacancies. In Table II, fifteen lines, labeled 32-48, are associated with triply excited resonances. They are identified via resonance

Table I. Observed Auger transitions of triply excited $2l2l'nl''$ (n=2-4) states in Li following $Li^+ + CH_4$ collisions.

Line Number	Resonance State	Decay Channel	Theoretical Prediction (eV)
A	$[(2s2p)\ ^3P\ 3p]\ ^2S$	$(1s5s)\ ^3S$	71.800[a]
B	$(2s^24s)\ ^2S$	$(1s4s)\ ^3S$	72.957[a]
d	$(2p^3)\ ^2P^o$	$(1s3p)\ ^1P^o$	73.730[β]
21	$(2s^22p)\ ^2P^o$	$(1s2p)\ ^1P^o$	74.660[γ]
22	$[(2s2p)\ ^3P\ 3p]\ ^2S$	$(1s3p)\ ^1P^o$	75.453[a]
23	$[(2s2p)\ ^3P\ 3d]\ ^2P^o$	$(1s3d)\ ^3D$	75.970[γ]
23	$[(2s2p)\ ^3P\ 3d]\ ^2P^o$	$(1s3d)\ ^1D$	75.970[γ]
24	$(2s2p^2)\ ^2D$	$(1s2p)\ ^3P^o$	78.140[δ]
25	$(2s2p^2)\ ^2D$	$(1s2s)\ ^1S$	78.498[δ]
33	$(2s^23s)\ ^2S$	$(1s2p)\ ^3P^o$	82.667[δ]
34	$(2s^23s)\ ^2S$	$(1s2s)\ ^1S$	83.025[δ]
35	$[(2s2p)\ ^3P\ 3s]\ ^2P^o$	$(1s2p)\ ^3P^o$	83.170[γ]
36	$[(2s2p)\ ^3P\ 3s]\ ^2P^o$	$(1s2s)\ ^1S$	83.530[γ]
37	$[(2s2p)\ ^3P\ 3p]\ ^2D$	$(1s2s)\ ^1S$	83.892[a]
38	$[(2s2p)\ ^3P\ 3d]\ ^2P^o$	$(1s2p)\ ^3P^o$	84.270[γ]
41	$[(2p^2)\ ^3P\ 3s]\ ^2P$	$(1s2p)\ ^3P^o$	85.453[a]
42	$[(2p^2)\ ^3P\ 4s]\ ^2P$	$(1s2p)\ ^1P^o$	85.910[a]
44	$[(2p^2)\ ^3P\ 4s]\ ^2P$	$(1s2p)\ ^3P^o$	86.850[a]

[α]Zhang and Chung (10), [β]Kiernan *et al.* 13), [γ]Chung and Gou (9), [δ]Chung (1).

Table II. Observed Auger transitions of triply excited $2l2l'2l''$ states in Be^+ following $Be^+ + CH_4$ collisions.

Line Number	Resonance State	Decay Channel	Peak Position (eV)	Theoretical Prediction (eV)*	Branching Ratio (%)[a]
32	$(2s^22p)\ ^2P^o$	$(1s2p)\ ^1P^o$	126.9 ± 0.1	126.896	16
36	$(2s^22p)\ ^2P^o$	$(1s2s)\ ^1S$	128.9 ± 0.1	128.913	11
36	$(2s2p^2)\ ^4P$	$(1s2p)\ ^3P^o$	128.9 ± 0.1	128.992	100
39	$(2s2p^2)\ ^2D$	$(1s2p)\ ^3P^o$	132.4 ± 0.1	132.514	34
40	$(2s2p^2)\ ^2D$	$(1s2s)\ ^1S$	132.8 ± 0.1	132.783	12
41	$(2s2p^2)\ ^2P$	$(1s2p)\ ^1P^o$	134.0 ± 0.1	133.913	35
41	$(2p^3)\ ^4D^o$	$(1s2p)\ ^1P^o$	134.0 ± 0.1	134.132	21
42	$(2s2p^2)\ ^2S$	$(1s2s)\ ^1S$	135.4 ± 0.1	135.477	20
43	$(2s2p^2)\ ^2P$	$(1s2p)\ ^3P^o$	135.8 ± 0.1	135.660	65
43	$(2s2p^2)\ ^2D$	$(1s2s)\ ^3S$	135.8 ± 0.1	135.839	53
43	$(2p^3)\ ^2D^o$	$(1s2p)\ ^3P^o$	135.8 ± 0.1	135.879	79
44	$(2p^3)\ ^2P^o$	$(1s2p)\ ^1P^o$	137.0 ± 0.1	137.094	14
45	$(2s2p^2)\ ^2S$	$(1s2s)\ ^3S$	138.5 ± 0.1	138.532	80
46	$(2p^3)\ ^2P^o$	$(1s2p)\ ^3P^o$	138.8 ± 0.1	138.841	82
48	$(2p^3)\ ^2P^o$	$(1s2s)\ ^3S$	142.4 ± 0.2	142.166	1

[a]Gou and Chung (9).

states, decay channels, and branching ratios. As can be seen from this table, the experimental Auger peak positions of the observed triply excited ($2l2l'2l''$) states are in excellent agreement with predictions from Gou and Chung (9). We note that the peak 36 may be composed of transitions arising from Be^+ $(2s^22p)\ ^2P^o$ and the Be^+ $(2s2p^2)\ ^4P$ states, where the quartet state decays to the $[(1s2p)\ ^3P^o \varepsilon p]\ ^4P$ continuum.

CONCLUSION

In this work, we have presented an experimental study of triply excited states of three electron systems formed by intermediate energy impact of Li^+ and Be^+ projectiles on CH_4. We have demonstrated that the triply excited states are populated in ion-molecule collisions under single collision conditions. Using high resolution electron spectroscopy individual lines arising from Li and Be^+ so called "hollow atoms" with two K-shell vacancies were resolved and identified. Theoretically, excitation energies, probabilities for Auger decay, and branching ratios have been derived from the literature and compared with our experimental results. Excellent agreement has been found between our experimental results and predicted non-radiative transition energies.

ACKNOWLEDGMENTS

This project has been partially supported by CNPq (Conselho National de Desenvolvimento Cientificico e Technológico), Brazil.

REFERENCES

1. Chung, K.T., *Phys. Rev. A* **25** 1596 (1982).
2. Safronova, U.I. and Bruch, R, *Phys. Scrpt.* **57** 519 (1998).
3. Connecely, M.J and Lipsky, L., *Phys. Rev. A* **61** 2506 (2000).
4. Bruch, R. *et al.*, *Phys. Rev. A* **12** 1808 (1975).
5. Bruch, R. and Chung, K.T., *Comments on At. Mol. Phys. D* **14** 117 (1984).
6. Rødbro, M. *et al.*, *J. Phys B* **12** 2413 (1979).
7. Rødbro, M. *et al.*, *J. Phys. B* **10** L275 (1977).
8. Simons, R.L. *et al.*, *Phys. Rev. A* **19** 682 (1979).
9. Gou, B.C. and Chung, K.T., *J. Phys. B* **29** 6103 (1996).
10. Zhang, Y. and Chung, K.T., *Phys. Rev. A* **58** 1098 (1998).
11. Agentoft, M. *et al.*, *J. Phys. B* **17** L433 (1984).
12. Bruch, R., *et al*, private communication (2000).
13. Kiernan, L.M. *et al.*, *J. Phys. B* **28** L161 (1995).
14. Azuma, Y. *et al.*, *Phys. Rev. Lett.* **79** 2419 (1997).
15. Wehlitz, R. *et al.*, *Phys. Rev. A* **60** 1050 (1999).
16. Diehl, S. *et al.*, *Phys. Rev. Lett.* **84** 1677 (2000).
17. Madsen, L.B., *et al.*, *Phys. Rev. Lett.* **85** 42 (2000).
18. Chung, K.T. and Gou, B.C., *Phys. Rev. A* **53** 2189 (1996).
19. Verbockhaven, G. and Hansen, J.E., *Phys. Rev. Lett.* **84** 2810 (2000).

Non-statistical Magnetic Substate Populations Following Excitation of Helium by Electron and Proton Impact

J. Hanni[a], H. Merabet[a*], A. Siems[b], R. Bruch[a], M. Bailey[a], D.V. Fursa[c], I. Bray[c], K. Bartschat[d], H.C. Tseng[e], C.D. Lin[f], A.G. Trigueiros[b]

[a]*Department of Physics, University of Nevada, Reno, NV 89557 USA*
[b]*Instituto de Física, Universidade Estadual de Campinas (Unicamp), 13083-970 Campinas, São Paulo, Brazil*
[c]*The Flinders, University of South Australia, GPO Box 2100, Adelaise 5001 Australia*
[d]*Department of Physics and Astronomy, Drake University, Des Moines, IA 50311, USA*
[e]*Department of Physics, Chung Yuan Christian University, Chung Li, Taiwan 32023*
[f]*Department of Physics, Kansas State University, Manhattan, KS 66506-2601 USA*

Abstract. The first experimental magnetic substate scattering angle-integrated cross sections following excitation of He ($1s^2$) ^{1}S to He (1snp) $^1P^o$ (n=2-5) in e- + He and H^+ + He collision systems have been determined using our differential cross sections and polarization fraction data in the extreme ultraviolet (EUV) range. The derived magnetic sublevel integrated cross sections, $\overline{\sigma}_0$ and $\overline{\sigma}_1$, for M_L=0,±1 have been studied over a wide range of projectile velocities: 1.4 to 8.5 a.u. and 1.4 to 7.5 a.u. for electron and proton impact on helium, respectively. In addition, the electron and proton collision data are compared with theoretical predictions using our improved first Born approximation (IFB), convergent close coupling (CCC) calculations for electron impact, and our recent atomic orbital close coupling (AOCC) calculations for protons. We have found that the electron results match very well the CCC predictions at all energies. However, the experimental proton data slightly deviate from the AOCC approach at intermediate velocities. Such findings are relevant to plasma and astrophysical applications.

Introduction

Two electron atomic systems are of fundamental importance to the investigation of complex many-body problems in physics (1). In the past, great effort has been devoted to the study of atomic and molecular collisions using helium atom as a target (2-5). Helium, is the simplest two-electron system, therefore it is well suited for studying the electron correlation effects (1,6-8). Previous research concerning excitation, ionization, double excitation and ionization-excitation of He has produced an extensive experimental and theoretical database necessary for achieving a deeper understanding of the collision dynamics in electron, proton, and multielectron ion impact on He at intermediate and higher energies (1-11).

We have measured differential excitation cross sections (DCS) $\overline{\sigma}$ for HeI (1snp) $^1P^o$ states, n=2-5, in e- + He and H^+ + He collisions using EUV spectrometry (11). These absolute cross sections do not provide direct information about the magnetic substate populations, while linear polarization measurements yield only the magnetic sublevel scattering angle-integrated cross section ratios $\overline{\sigma}_0 / \overline{\sigma}_1$. These ratios are directly related to the degree of linear polarization (11) as:

$$P = \frac{I_{\parallel} - I_{\perp}}{I_{\parallel} + I_{\perp}} = \frac{\overline{\sigma}_0 - \overline{\sigma}_1}{\overline{\sigma}_0 + \overline{\sigma}_1} = \frac{1-r}{1+r} \qquad (1)$$

where $I_{\parallel}$ is the intensity of radiation with electric field vectors oriented along the beam axis and $I_{\perp}$ is the intensity of radiation with a transverse electric field vector (perpendicular to the plane formed by the incident projectile beam and the direction of observation); $r = \overline{\sigma}_0 / \overline{\sigma}_1$, is the cross section ratio. Moreover, the differential cross section $\overline{\sigma}$ is the sum of the three magnetic sublevel angle-integrated cross sections,

$$\overline{\sigma} = \overline{\sigma}_0 + 2\overline{\sigma}_1 \qquad (2)$$

Thus, by combining Eq. 1 and Eq. 2, the magnetic sublevel integrated cross sections can be obtained.

Another procedure has been employed, where the ratio of the magnetic sublevel (scattering) angle-differential cross section, σ_0, to the differential cross

* Corresponding author: H. Merabet, email: hocine@physics.unr.edu

section, called the parameter $\lambda = \sigma_0 / (\sigma_0 + 2\sigma_1)$, is determined experimentally using electron-photon coincidence techniques (12). The λ parameter, combined with available double differential cross section ($\sigma = \sigma_0 + 2\sigma_1$) data, yields σ_0. This approach has been utilized by Chutjian *et al.* for the excitation of HeI (1s2p) $^1P^o$ level, at 60 and 80 eV electron impact energies (13), and HeI (1s2p) $^1P^o$ level at 80 and 100 eV (14); whereas Hummer *et al.* (15) have directly obtained the relative σ_0 for the excitation of the HeI (1s3p) $^1P^o$ state at 70 eV as a function of the scattering angle. Furthermore, Harris and co-workers (16) have measured triple differential cross sections for HeI (1s3p) $^1P^o$ for electron impact energy of 40 eV. In addition, Csanak *et al.* (17) have used the λ parameter procedure to extract HeI (1snp) $^1P^o$ (n=2-3) triply differential cross sections and have computed the corresponding theoretical integral values for n=2-6 with incident energy in the 25-500 eV range, using first-order many-body theory (FOMBT) (18). To our knowledge, no experimental data are available for HeI (1snp) $^1P^o$ $n \geq 4$ levels.

In this work, we have combined measurements of two experimental techniques, namely EUV spectrometry and EUV polarimetry, to determine experimental cross section results for HeI (1snp) $^1P^o$ (n=2-5) excited states following electron and proton impact at a wide range of projectile velocities. These experimental data are compared with our IFB as well CCC results for electrons, and first Born (B1) (19) along with the AOCC predictions for protons, in an attempt to shed more light on the excitation processes of helium during the collision at intermediate and high energies. The CCC and AOCC methods have been described in detail by Fursa and Bray (20), and Fritsch *et al.* (21), respectively, whereas the IFB method is essentially similar to the first Born approximation, however with a better target description.

RESULTS AND DISCUSSION

The experimental setup used in this work consists of three main components: an EUV polarimeter; an electron gun or a 2 MV Van de Graaff accelerator, target cell and Faraday cup; and a 1.5 meter grazing incidence monochromator. A PC controlled data acquisition system has been used to operate the apparatus and to record the data. A detailed description of this experimental setup is given by Bailey *et al.* (7,22). In brief, the polarimeter utilizes a molybdenum-silicon (Mo/Si) MLM whose surface reflection has been used for radiation with a wavelengths λ > 584 Å at an incidence angle of 40° corresponding to the HeI (1snp) $^1P^0 \rightarrow (1s^2)\ ^1S$ (n=2-5) transitions. It is assumed here that the degree of linear polarization does not depend on the principal quantum numbers n. The corresponding differential cross sections $\bar{\sigma}$ measurements have been conducted using a 1.5 m high resolution grazing incidence monochromator (7-8). These results have been put on an absolute scale by normalizing our data to the Bethe-Born cross section values (23), for electron and proton impact, at high velocities. This normalization procedure has been described in more details in Ref. (7). In this work, the obtained cross section data have also been corrected for alignment effects using (9),

$$\bar{\sigma}(\theta) = \bar{\sigma} \times \left\{1 + A_0\, P_2(\cos\theta)\right\} \qquad (3)$$

where $\bar{\sigma}(\theta)$ is the measured cross section, θ=90^o is the observation angle of the emitted photons, $\bar{\sigma}$ is the cross section for an isotropic distribution, $P_2(\cos\theta)$ is the second Legendre polynomial, and A_0 is the alignment parameter related to the degree of linear polarization by:

$$P(^1P^o) = \frac{3A_0}{A_0 - 2} \qquad (4)$$

In the following, we have analyzed the obtained cross sections for electron, and proton projectiles as a function of impact velocities for HeI (1s2p) $^1P^o$ states. The complete set of data for higher Rydberg states, with the quantum number n=3-5, are available and will be published in the near future. A preliminary comparison of both experimental and theoretical results is also given.

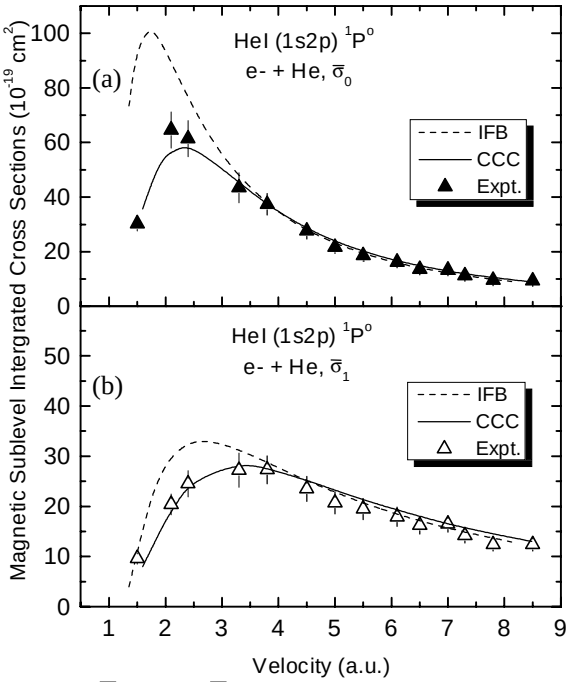

Figure 1. $\bar{\sigma}_0$ (a) and $\bar{\sigma}_1$ (b) for e$^-$ + He collisions, compared with CCC and IFB calculations.

A. Electron Impact on Helium

Using equations (1) and (2), we have derived $\bar{\sigma}_M$ following HeI (1snp) $^1P^o \rightarrow (1s^2)\ ^1S$, (n=2-5), transitions in e- + He collisions at impact energies ranging from 30 to 980 eV (1.4 < v< 8.5 a.u.). As an example, we have shown in Fig. 1, $\bar{\sigma}_0$ and $\bar{\sigma}_1$ for HeI (1s2p) $^1P^o$ states along with our IFB and CCC predictions. We have used our polarization and DCS data for $v \geq 3$ a.u. The shown lower velocities magnetic substate cross sections $\bar{\sigma}_M$ for electrons have been extracted by combing the DCS of Westerveld *et al* (4) with our polarization results. As can be seen, both theories and experimental results are in excellent agreement in the high-energy range. At relatively lower energies, the IFB predictions diverge from the experimental data, while our CCC values coincide with the measured results. This confirms that the CCC is an excellent approach for describing the e-He scattering problem.

Furthermore, the $\bar{\sigma}_0$ cross sections are all equal to the theoretical predictions within experimental uncertainties. However, the $\bar{\sigma}_1$ cross sections slightly deviate from theory. Fig. 2 exhibit our $\bar{\sigma}_0$ compared with $\bar{\sigma}_1$ for electron impact. The velocity dependence of these cross sections reveals a strong anisotropy of the photon emission originating from the HeI (1s2p) $^1P^o$ states at v <4 a.u.. From Fig. 2 it is also evident that the population of the sublevels with $M_L = 0$ is

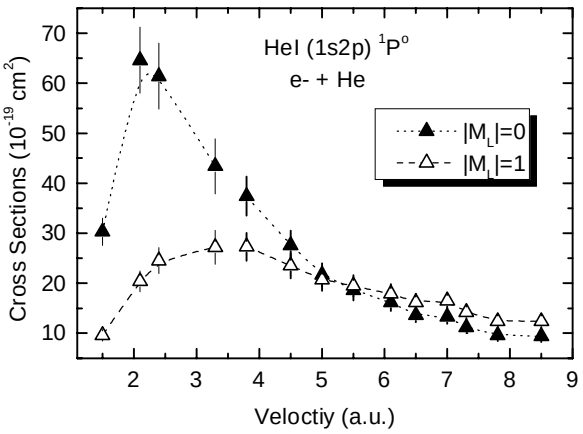

Figure 2. Comparison of MSICS σ_0 with σ_1 for electron impact on He. Fitted curves are provided to guide the eye.

greater than those with $M_L = \pm 1$ at impact velocities below 5 a.u. The cross sections $\bar{\sigma}_0$ and $\bar{\sigma}_1$ are equal at approximately v=5 a.u. For high electron velocities, the situation is reversed, *i.e.* $\bar{\sigma}_1$ is little larger than $\bar{\sigma}_0$, leading to a nearly isotropic photon emission.

B. Proton Impact on Helium

The cross sections $\bar{\sigma}_0$ and $\bar{\sigma}_1$ for HeI (1snp) $^1P^o$ states following proton impact have been extracted using the procedure outlined above at energies ranging from 50 to 1400 keV (1.4 < v< 7.5 a.u.). We have plotted in Fig. 3 the obtained experimental results in comparison with AOCC and B1 theoretical calculations corresponding to HeI (1s2p) $^1P^o \rightarrow (1s^2)\ ^1S$ transitions. In general, our experimental findings deviate from the B1 approximation at intermediate projectile velocities. The AOCC theory is somewhat closer to experiment than the first Born results, but it also partially fails to reproduce the measured values at lower velocities. Specifically, $\bar{\sigma}_1$ values match well the B1 and AOCC results in the studied velocity range. However, the 2 a.u. impact velocity point disagrees completely with both theories. We further note that in the case of M_L = 0, this lower impact velocity point is in excellent accord with the AOCC prediction and also in good agreement with the B1 approximation. In the high-energy limit, our experimental cross sections converge with both theories.

The AOCC calculations, presented in this paper, have been performed utilizing limited target states and they are, therefore, not expected to completely reproduce the experimental. data in the intermediate energy range. A more accurate calculation, including extended target states may improve the convergence to the experimental data. Such more sophisticated calculations are now being performed.

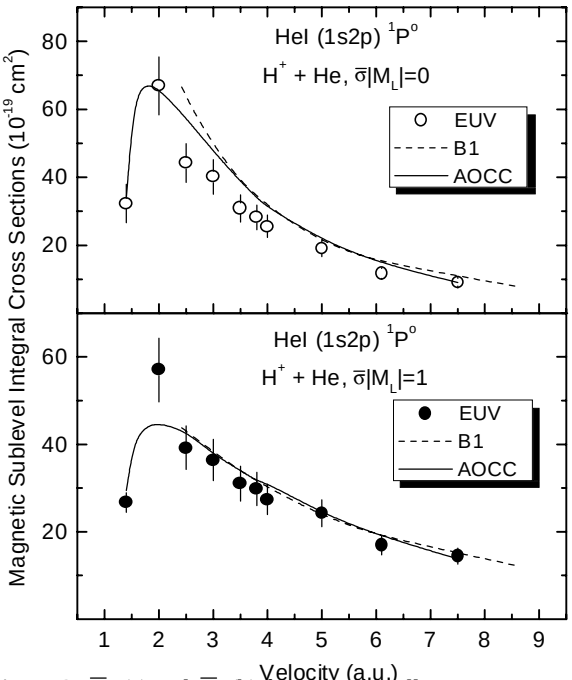

Figure 3. $\bar{\sigma}_0$ (a) and $\bar{\sigma}_1$ (b) for H^+ + He collisions, compared with CCC and IFB calculations.

Now let us compare the $\bar{\sigma}_M$ proton cross sections. Fig.4 shows these cross sections for $M_L = 0$ and $M_L = \pm 1$. In the vicinity of v = 3.5 a.u., $\bar{\sigma}_0$ is equal to $\bar{\sigma}_1$. At lower proton velocities, $\bar{\sigma}_0$ is slightly larger than $\bar{\sigma}_1$, however the error bars are large. Above v = 4 a.u., $\bar{\sigma}_1$ overtakes $\bar{\sigma}_0$ and it clear that, for impact velocities higher than 5 a.u., an anisotropic population of the magnetic sublevel cross sections occurs.

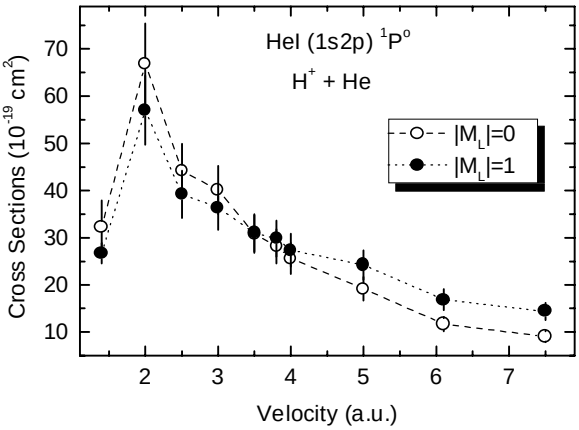

Figure 4. Comparison of $\bar{\sigma}_0$ with $\bar{\sigma}_1$ for proton impact on helium. Fitted curves have been provided to guide the eye.

It interesting to study the charge state dependence for electron and proton projectiles in order to gain a better understanding of the excitation process. This is the main focus of the following section.

C. Comparison of Electron and Proton Cross Section Results

We have depicted in Fig. 5, $\bar{\sigma}_0$ and $\bar{\sigma}_1$ for electron and proton impact. Fig. 5(a) compares $\bar{\sigma}_0$ cross sections. From 2.5 to 6 a.u., the electron and proton cross sections deviate, *i.e.*, the electron results are greater than the protons. For higher impact velocities, they converge, whereas at the lower velocities, they appear to be approximately equal. Fig. 5(b) indicates that the electron and proton cross sections are clearly unequal below 3.5 a.u., but they coincide at higher velocities. This excellent agreement in the high-energy limit is expected since both experiment and theoretical results agree very well for electrons and protons and confirm, therefore, that the excitation cross sections are independent of the charge-state and mass of the projectile.

In summary, excellent agreement between theory and experiment has been found for electron impact, although this is not quite the case for the H^+ + He collision system which requires a more accurate theoretical description to elucidate the detailed dynamics of the excitation process.

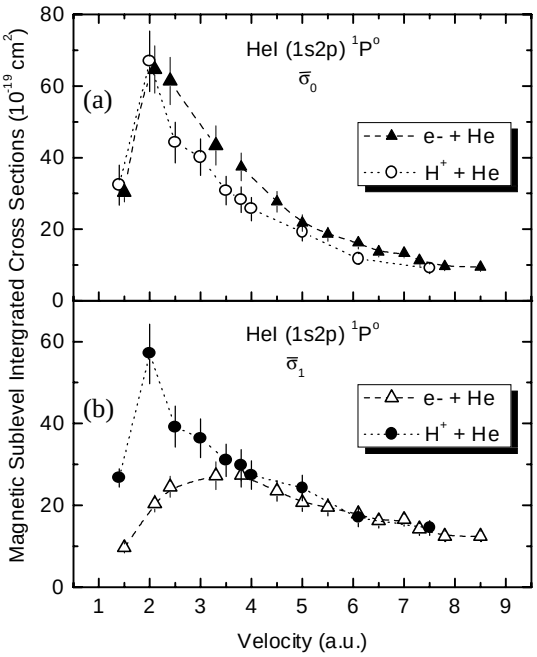

Figure 4.: Comparison of for electron (a) and proton (b) impact on He. Fitted curves have been provided to guide the eye.

ACKNOWLEDGMENTS

This Project has been supported in part ACSPECT Corp. and the Nevada Business and Science Foundation, (NBSF) Reno, Nevada.

REFERENCES

1. McGuire, J. H., *Electron Correlation Dynamics In Atomic Collisions*, (Cambridge University Press, 1997).
2. van den Bos, J. *et al.*, Physica **40**, 357 (l968).
3. Hippler, R. et al., K.H., *J. Phys. B* **7**, 618 (1974).
4. Westerveld, W.B. *et al.*, *J. Phys. B.* **12**, 115 (1979).
5. Forand, J.L. *et al.*, *J. Phys. B:* **18**, 1409 (1985).
6. Bruch, R. *et al.*, *Encyc. Applied Phys.* **10**, 437 (1994).
7. Bailey, M. *et al.*, *J. Phys. B* **28**, 2655 (1995).
8. Merabet, H. *et al.*, *Phys. Rev. A* **60**, 1187 (1999).
9. Hammond, P. *et al.*, *Phys. Rev. A.* **40**, 1804 (1989).
10. Götz, A. *et al.*, *J. Phys. B.* **29**, 4699 (1996).
11. Merabet, H. *et al*., this issue.
12. Blum, K. *et al*., *Adv. At. Mol. Phys.* **19**, 187 (1983).
13. Chutjian, A. et al., *J. Phys. B* **8**, 2360 (1975).
14. Chutjian, A., *J. Phys. B* **9**, 1749 (1976).
15. Hummer, C.R. *et al*., *Phys. Rev. A* **33**, 2995 (1986).
16. Harris, C. L., *Ph.D. Thesis*, University of Nevada, Reno (2000), unpublished.
17. Csanak, G. *et al*., *Phys. Rev. A* **45**, 1625 (1992).
18. Csanak, G. *et al*., *Phys. Rev. A* **3**, 1322 (1971).
19. L. Vriens and J.D. Carrière, *Phys. Scp.* **49**, 517 (1970).
20. Fursa, D.V. *et al.*, *J. Phys. B* **30**, 757 (1997).
21. Fritsch, W. and Lin, C.D., *Phys. Rept.* **201**, 1 (1991).
22. Bailey, M. *et al*., *Appl. Opt.* **38**, 4125 (1999).
23. Kim, Y. K. *et al*., Phys. Rev. **l84**, 38 (l969).

Development of x-ray and extreme ultraviolet (EUV) glass capillary optical devices for diagnostics and instrumentation for various sensing and diagnostics applications

R. BRUCH*, A. SIEMS**, H. MERABET*, and B. S. RAWAT***

*Department of Physics
University of Nevada Reno
Reno, NV 89557 USA
Tel: +1 775 784-4920 Fax: +1 775 784-1753 e-mail: bruch@physics.unr.edu

**Instituto de Física 'Gleb Wataghin'
Universidade Estadual de Campinas (Unicamp)
13083-970 Campinas, São Paulo, Brazil
Tel: +55 19 788 5456 e-mail: siems@ifi.unicamp.br

***Department of Electrical Engineering
University of Nevada Reno
Reno, NV 89557 USA
Tel: +1 775 784-6927 Fax: +1 775 784-6627 e-mail: rawat@ee.unr.edu

Abstract

New optical methods of surface sensitive instrumentation for diagnostics of extreme ultraviolet (EUV), soft X-ray (SXR) and X-ray radiation have been developed. In particular, our optical technology is of great importance for studies of micron size structures, plasma and biomedical diagnostics studies and is based on glass capillary converters (GCCs). These optical GCC devices provide guiding, focusing and polarization analysis of short wavelength radiation within a large bandwidth.

1.INTRODUCTION

As the semiconductor industry is pushing miniaturization of electronic devices, new compact short wavelength radiation sources and analytic detection systems are becoming indispensable in manufacturing facilities of micro and nanostructure devices [1]. At this stage, pattern dimensions in nanoelectronics will shrink towards 10 nm [2]. In the near future such single electron structures will place demanding requirements on nanolithography. Potentials and challenges for EUV [3] and X-ray applications for lithography today are concerned with the 0.13 μm outlook.

Recently capillary optics has matured as a new tool for more efficient investigations of surface and bulk analysis and numerous other applications [4-8] including nondestructive, noninvasive diagnostics methods and non or minimally invasive treatment of cancerous tissue [9], where the X-rays could be guided, and focussed via a polycapillary collimating optic system. Another application is concerned with neutron optics for example for transmutation of nuclear waste [10, 11].

Furthermore in investigations of laboratory experiments with EUV, SXR and X-rays sources we are frequently challenged by spectroscopic and polarization measurements in the (i) extreme ultraviolet (EUV) 10 nm< λ <100 nm, (ii) soft X-ray (SXR) 0.4 nm < λ < 10 nm, and (iii) X-ray wavelength regions λ < 0.4 nm. In these types of investigations the greatest challenge generally is: (a) The analysis of radiative sources, (b) the development of very compact, lightweight and versatile optical instrumentation in the short wavelength range, and (c) high resolution spectroscopic and polarization measurements in the EUV, SXR and X-ray range.

Therefore the objective has been: to generate, analyze and detect extreme ultraviolet (EUV), soft X-ray (SXR) and X-ray signals with high spatial resolution and (ii) to image a source area or volume onto a detection system with a specific cross sectional area. Recently we have tested for the first time new types of glass capillary converters (GCCs) for the (EUV) region to increase the spectral sensitivity of our short wavelength spectroscopy instrumentation. Such devices can concentrate, guide and focus short wavelength radiation from a source onto a detection system, and at the same time optimize the shape of the cross section of the photon beam for a specific configuration of the aperture of the analyzing system. Traditionally utilized optical systems consist of grazing incidence toroidal mirrors or multilayer mirrors (MLMs) to collect and focus optical signals in the short wavelength region. They are more difficult to apply for imaging

applications, whereas GCCs are very versatile even for complex imaging optics. These wide band optical systems are cost effective, relatively simple and have the potential to enhance the flux density of radiation by a factor of four to several hundred.

The major goal of this study has been the creation of modern optical devices and instrumentation for diagnostics of surfaces, biomedical microscopy, fluorescence techniques in the EUV, SXR, and X-ray regions, photon-induced fluorescence spectroscopy, imaging, and X-ray and SXR lithography. Specifically, we have been involved in the development of compact, ultra sensitive, high throughput spectrometers for analysis of SXR radiation based on sliced multilayer gratings (SMG), compact spectrometers and polarimeters based on MLMs, small size grazing incidence spectrometers for SXR imaging systems and Schwarzschild microscopes for surface imaging applications [12]. All these devices can take advantage of glass capillary optics.

2. GLASS CAPILLARY OPTICS

An integral part of our advanced instrumentation program at the University of Nevada Reno and ACSPECT Corporation, Reno are glass capillary converters (GCCs), specifically designed for EUV, SXR or X-Ray spectroscopy and fluorescence techniques. The basic optical properties of these GCC optical elements are illustrated in Fig. 1.

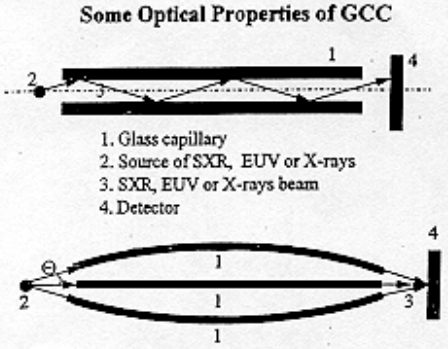

Fig. 1: (a) Propagation of short wavelength radiation along a hollow channel of a glass capillary. 1. Monocapillary, 2. Source of EUV, SXR or X-Ray radiation, 3. EUV, SXR, or X-Ray beam, 4. Detector or irradiated object. (b) Schematic diagram of a focussing glass capillary concentrator (GCC) 1. Capillaries, 2. Source, 3. Focus, 4. Detector or Surface.

In Fig. 2 we depict schematically the principle for internal total reflection for x-ray radiation. Also shown is a diagram for the reflection coefficient R as a function of the angle of incidence Θ. It is evident that at $\Theta = \Theta_{cr}$ the reflectance R decreases rapidly. In addition we have listed in this figure the critical angles for two typical X-ray sources, namely Cu K_α (E = 8 keV) and Mo K_α (E = 17.4 keV), respectively. The detailed characteristics of the X-ray capillary optic applications are discussed by Langhoff and coworkers [13-16].

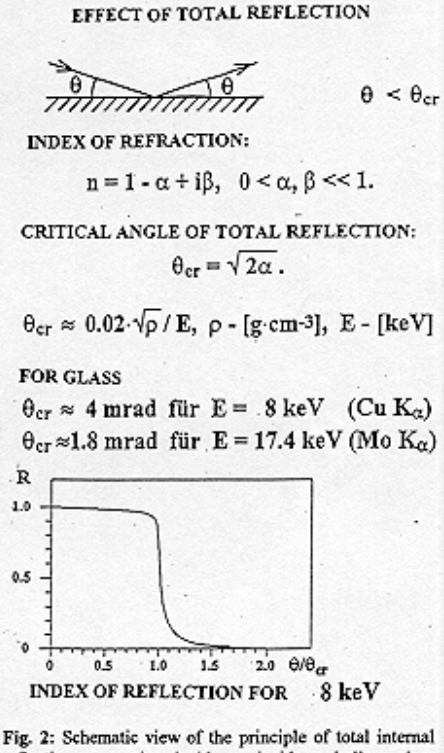

Fig. 2: Schematic view of the principle of total internal reflection at grazing incidence inside a hollow glass capillary. n is the index of reflection, Θ_{cr} the critical angle of total reflection, E the photon energy in keV, ρ the density of the optical glass material, and R the internal reflection coefficient. Also shown is the reflection coefficient versus Θ/Θ_{cr} for Cu K_α radiation.

In Fig. 3 a comparison of different types of more complex GCC devices for enhancement of radiation and image formation is provided. As can be seen such devices can for example concentrate, guide, and focus short wavelength radiation from a source onto a monochromator or detector system, and at the same time optimize the shape of the cross section of the photon flux for each specific configuration of the entrance window of the analyzing detection system.

In contrast to frequently used optical devices such as grazing incidence toroidal mirrors to

enhance and focus weak optical signals in the EUV, SXR and X-ray region, GCCs can be more easily adapted to complex imaging problems.

These wide-band optical systems are cost effective, relatively simple, and have the potential to enhance the flux density radiation by a factor of about 4-100, depending on the complexity and the wavelength range. Such GCCs generally consist of a bundle of capillaries and the guiding properties are based on the effect of total external reflection of radiation from the smooth surfaces of these capillaries at grazing incidence. Especially, for X-rays the critical angle of incidence is smaller than 0.1 degrees, whereas for SXR radiation this angle varies between 2 and 3 degrees, and for EUV application this angle is slightly larger.

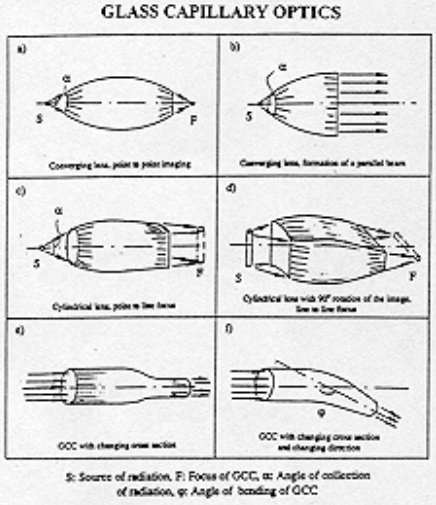

Fig. 3: Comparison of different types of GCCs and image formation: (a) Converging lens, point to point imaging; (b) Converging lens, formation of a parallel beam; (c)Cylindrical lens, point to line focus; (d) Cylindrical lens with 90° rotation of the image, line to line focus; (e) simple GCC with changing cross section; (f) GCC with changing cross section and changing direction of photon beam. S: source of radiation, F: Focus of GCC, α : Angle of collection of radiation, ϕ : Angle of bending of GCC.

To test the efficiency of such new optical devices we have studied EUV spectra arising from Ar^{8+} + He collisions [6] as indicated in Fig. 4. It is evident from this figure that the radiation from the target area is enhanced by our GCC optics by a factor of about ten. In this experiment the EUV photons emitted by multicharged Argon ions exit a target cell at 90° with respect to the ion beam and they are collected, guided and focused by our new GCC device onto the entrance slit of a 2.2 m grazing incidence monochromator. The monochromator entrance slit is 60 cm away from the target area. In this experiment the GCC system images a horizontal (cylindrical) ion beam segment ("line" - shaped source) and focuses the radiation onto the vertical entrance slit of the monochromator.

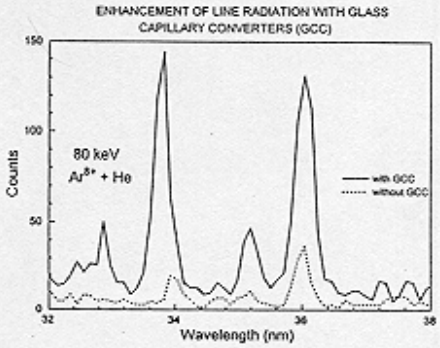

Fig. 4: (EUV) spectrum in the wavelength range from 32 to 38 nm following Ar^{8+} + He collisions at 80 keV: — the measurement has been performed with complex GCC optics, --- without GCC optics.

For alignment purposes the GCC is mounted on a (X,Y,Z) holder in a vacuum chamber and can be moved along three mutually perpendicular directions. The intrinsic focal distances of the GCC at the entrance and exit plane are 50 and 60 mm, respectively. Another important application of the capillary optics is associated with concentration of X-rays. A combination of a polycapillary conic collimator with an X-ray detector is depicted in Fig. 5.

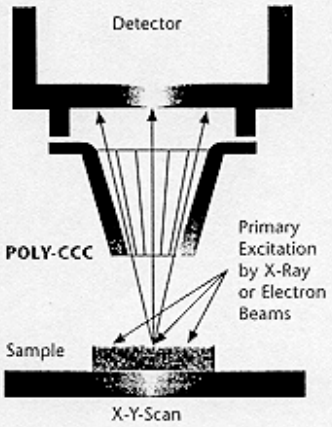

Fig.5: Polycapillary conic collimator for spatially resolved X-ray detection

The Si (Li) X-ray detector allows spatially resolved detection of X-ray fluorescence signals from a small surface area of a sample. The polycapillary consists of many channels, which are oriented towards one point producing a minimum spatial resolution of 20 µm. As can be seen from Fig. 5 the divergent fluorescence radiation is collected and transmitted to the X-ray detector by this kind of GCC optics [16].

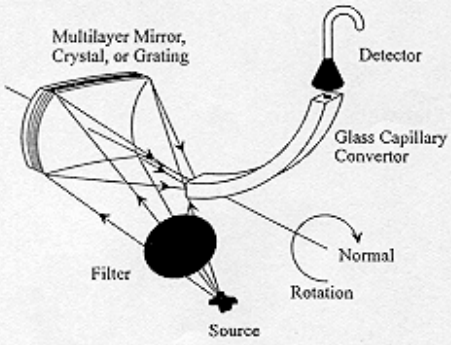

Fig. 6 Short wavelength polarimeter consisting of an MLM, crystal or grating (narrow bandwith), a curved GCC (wide bandwith) and a detector

Finally we show in Fig. 6 the principle of a short wavelength polarimeter with two polarization sensitive optical components in tandem, i.e. an MLM, crystal or grating and a curved capillary optical device that can be rotated to analyze the polarization of an EUV, SXR or X-ray source. Here the first optical device represents a highly dispersive system, whereas the GCC provides more broad band transmission.

3. CONCLUSION

In this study we have briefly discussed and demonstrated that hollow capillaries similar to optical fibers can be utilized as optical waveguides for short wavelength radiation in the EUV, SXR and X-ray range. We are exploring now different types of hollow capillaries and optical materials for the manufacturing of complex optical systems. We are in particular interested to apply this new technology to imaging applications and non or minimally invasive in vivo methods for biomedical diagnostics [9]. Such single capillaries and/or capillary optic systems are provided for example by ACSPECT Corporation, Reno, Nevada, USA and/or the Institut für Gerätebau (ifg), Berlin, Germany.

4. ACKNOWLEDGEMENTS

This project is supported in part by the Department of Energy (DOE), the United States Industry Coalition (USIC), and ACSPECT Corporation, Reno, Nevada, USA.

References

[1] R. Turton, " The Quantum Dot.", *Oxford University Press*, 1999.

[2] J. P. Silverman, *J. Vac. Sci. Technol.*, vol. B 15, p. 2117, 1997.

[3] Silver and S. Kahn, "UV and x-ray spectroscopy of laboratory and astrophysical plasmas", *Cambridge University Press*, 1993.

[4] V. Kantsyrev and R. Bruch, "New optical methods for short wavelength hot plasma diagnostics", *Rev. Sci. Instru.*,. vol.. 68, pp. 770-773, 1997.

[5] V. Kantsyrev and R. Bruch, "New methods of high sensitivity, high resolution instrumentation for spectroscopic, angular and polarization measurements in the EUV, SXR and x-ray ranges", *Phys. Scrip.*, vol. T73, pp. 393-396, 1997.

[6] R. Bruch, V. Kantsyrev, R. Phaneuf, V. Golovkina, A. Shlyaptseva and D. Schneider, "Application of new spectroscopic technique for the study of interaction of multicharged ions with gaseous targets in the extreme ultraviolet", *Phys. Scrip.*. vol. T73, pp. 397-399, 1997.

[7] V. Kantsyrev, R. Bruch, M. Bailey, and A. Shlyaptseva, "Enhancement of the flux density of line radiation in the extreme ultraviolet wavelength region for spectroscopic and plasma diagnostic applications using glass capillary converters", *Appl. Phys. Lett.*, vol. 66, pp. 3567-3569, 1995.

[8] Spectroscopy vol.14, no.2, p.1, 1999

[9] R. Bruch, N. Afanasyeva, S. Sukuta, A. Brooks, V. Makhine, and S. Kolyakov, "Various new applications of fiberoptical infrared Fourier transform spectroscopy for dermatology", *Proc. of Medical Applications of Lasers in Dermatology, Cardiology, Ophtamology, and Dentistry II, EUROPT Series, SPIE.*, vol. 3564, pp. 42-50, 1998.

[10] E. D. Arthur, "The Los Alamos accelerator transmutation of nuclear waste (ATW) concept", *ATW-92-60, Presented to STATS, Subcommittee on Transmutation*, Los Alamos, April 15-16, 1992.

[11] R. Bruch, "The crisis and future of Nevada's entrepreneurial culture", *Nevada's Washington Watch*, vol. 5, Issue 38, February 1999.

[12] R. Bruch, H. Merabet, M. Bailey, S. Showers, and D. Schneider, " Development of x-ray and extreme ultraviolet (EUV) optical devices for diagnostics and instrumentation for various surface applications", *Surf. Interface Anal.*, vol. 27, in press 1999.

[13] R. Wedell, Röntgenlichtleiter in der Analysetechnik, *Phys. Bl.* vol. 52, p. 1134, 1996.

[14] V. A. Arkadiev, B. Beckhoff, A. A. Bzhaumikov, H. E. Gorny, B. Karmgieber, *SPIE* vol.. 2859, p.123 , 1996.

[15] V. A. Arkadiev, A. A. Bzhaumikov, H. E. Gorny, J. Schmalz, *SPIE* , vol. 2859, p. 202 , 1996.

[16] Polycapillary conic collimator for local x-ray detection, *Institut für Gerätebau GmbH (ifg), Berlin, Poly – CCC Data Sheet*, 1998.